APPLICATION OF AN ELECTROSTATIC ION TRAP TOWARDS NUCLEAR AND LASER SPECTROSCOPY AT IGISOL–4

A thesis submitted to the University of Manchester
for the degree of Doctor of Philosophy
in the Faculty of Engineering and Physical Sciences

2016

Alex Robert Dicker
School of Physics and Astronomy

Contents

Word count 32891

List of Tables

List of Figures

Abstract

This thesis entitled "Application of an electrostatic ion trap towards nuclear and laser spectroscopy at IGISOL–4" was submitted to the University of Manchester on 21^{st} September 2015 by Mr Alex Robert Dicker for the degree Doctor of Philosophy (PhD).

The new ion guide isotope separator, IGISOL–4, at JYFL, Jyväskylä has been commissioned, and new spectroscopy and structural measurements are reported here. The first optical measurements of radioactive ^{101,107}Mo isotopes, with definite spin assignments, are presented. The measurements provide insight into the development of the structure and deformation around N=60 for molybdenum. A clear, exaggerated odd–even staggering in the mean–square charge radii up to N=60, followed by an immediate change in character, shows the chain to possess a far less smooth shape development than previously thought. The measurements of ^{107}Mo confirm this isotope to mark the peak of the deformation in molybdenum and these results, achieved in the limits of fission fragment production, display the improved capabilities of the IGISOL–4 facility (these two isotopes were too challenging to be studied previously at IGISOL–3).

The commissioning stages of the electrostatic ConeTrap are detailed, from the initial off–line investigations (in comparison to detailed simulations), to the first successfully stored and extracted radioactive ions. The detection of a hyperfine resonance has been achieved from (stable) hafnium ions stored and extracted from the trap prior to resonant excitation, with no observable ion energy perturbations induced by the trapping.

The observation of a resonant optical pumping effect on yttrium ion survival is presented. Pumping of an ionic ensemble within the Cooler–Buncher is shown to lead to a change in ion survival, directly observed through a change in the measured ion rates. The ConeTrap was observed to enhance this effect upon further storage of pre–pumped ions.

A new, bespoke data acquisition system for collinear laser spectroscopy is presented. The microcontroller based system provides time stamping of photon arrival, a multiple photon tracker for two photon gating and full software control over photon time gates. A novel approach for searching for weak hyperfine peaks is implemented in the system. This 'photon multiplication method' provides greater statistics on resonance peaks, providing a greatly increased accuracy in peak centroid determination.

Declaration

No portion of the work referred to in the thesis has been submitted in support of an application for another degree or qualification of this or any other university or other institute of learning.

Copyright Statement

i. The author of this thesis (including any appendices and/or schedules to this thesis) owns certain copyright or related rights in it (the "Copyright") and he has given The University of Manchester certain rights to use such Copyright, including for administrative purposes.

ii. Copies of this thesis, either in full or in extracts and whether in hard or electronic copy, may be made **only** in accordance with the Copyright, Designs and Patents Act 1988 (as amended) and regulations issued under it or, where appropriate, in accordance with licensing agreements which the University has from time to time. This page must form part of any such copies made.

iii. The ownership of certain Copyright, patents, designs, trade marks and other intellectual property (the "Intellectual Property") and any reproductions of copyright works in the thesis, for example graphs and tables ("Reproductions"), which may be described in this thesis, may not be owned by the author and may be owned by third parties. Such Intellectual Property and Reproductions cannot and must not be made available for use without the prior written permission of the owner(s) of the relevant Intellectual Property and/or Reproductions.

iv. Further information on the conditions under which disclosure, publication and commercialisation of this thesis, the Copyright and any Intellectual Property and/or Reproductions described in it may take place is available in the University IP Policy (see http://documents.manchester.ac.uk/DocuInfo.aspx?DocID=487), in any relevant Thesis restriction declarations deposited in the University Library, The University Library's regulations (see http://www.manchester.ac.uk/library/aboutus/regulations) and in The University's Policy on Presentation of Theses.

Acknowledgments

Firstly I would like to express my deepest gratitude to my supervisor Paul Campbell for providing guidance and support throughout my PhD, which has been a fantastic learning experience. Paul has patiently steered me through the last four years, and I've benefited from his extensive experimental experience and 'quietly confident' approach. I'd also like to thank Bradley Cheal for his assistance and support through the first few years.

I've had the chance to meet many wonderful people along the way. A big thank you to the IGISOL group in Jyväskylä, especially Iain Moore, who made me welcome and aided me during my long term attachment. The cold winters and pleasant summers were greatly improved by the presence of two fellow students, Jack Henderson and Chris 'fire starter' McPeake, who were always enthusiastic about beers, barbeques and a few glasses (or bottles) of whisky.

Finally I'd like to thank all the members of the Manchester nuclear physics group for creating a relaxed working atmosphere. Special thanks to Duncan Johnson and Sam Kelly, who have been great friends and colleagues through many conferences, long night shifts and pub lunches.

Chapter 1

Introduction

The iconic gold foil scattering experiment of Rutherford in 1911 provided the first evidence for an atomic nucleus [1]. The nucleus has been studied for over 100 years with great progress achieved in our understanding of the nuclear and atomic structure. Much effort has since been invested into theoretical models and experimental study of nuclear properties and their effects on the atomic structure. The hyperfine structure of atomic spectral lines was first observed in the late 19^{th} century, but it was not until 1924 that Pauli linked the phenomenon to the interaction of the nucleus with the surrounding electron cloud [2]. In his paper Pauli outlined the coupling of the nuclear spin with the electron angular momentum describing the splitting as a magnetic interaction, and made an estimate of a possible electric quadrupole interaction. In 1927 Back and Goudsmit made their detailed study of bismuth lines, extracting the nuclear spin of ^{209}Bi [3]. This confirmed Pauli's description and the concept of the nuclear magnetic moment, with the interaction between the electrons and nucleus being magnetic. In 1931 H. C. Urey and G. M. Murphy measured the optical emission spectra for samples of hydrogen gas, discovering the mass A=2 isotope, which was named deuterium [4]. In 1932 this discovery was published and just 7 weeks later the picture of the nucleus changed with the discovery of the neutron by James Chadwick [5], (who received the Nobel prize in 1935 for his contributions to physics). Shortly after in 1935 Schmidt and Schüler [6] described the quadrupole term of the hyperfine interaction after discovering large deviations from the magnetic splitting in mercury spectral lines. The origin of the isotope shift was also explained in the 1930s, with a detailed study of the effects due to changes in neutron number.

The nuclear chart today consist of more than 3000 known nuclei, with many facilities around the world dedicated to the study of a wide range of their properties. These facilities run experimental campaigns, probing different aspects of nuclear structure and nuclear astrophysical problems. A wide variety of techniques have been developed over the years, enabling researchers to probe properties with greater accuracy and sensitivity to study isotopes further and further from stability, where lifetimes and production methods become limiting experimental factors. One such facility is the IGISOL (Ion Guide Isotope Separator On–Line) experiment at the University of Jyväskylä accelerator laboratory, which began construction in the early 1980s [7], where the ion guide technique was implemented as an ion source for the existing isotope separator (using a K–20 proton cyclotron for the primary beam). This relied on a unique technique for isotope production where thin targets and buffer gases were employed, as opposed to a more standard thick target approach. This technique allows the production of radioactive ion beams with much shorter half–lives than other facilities and over a wide range of the periodic table due to comparatively shorter extraction times and the chemical insensitivity of the production and extraction mechanisms. Over the years the IGISOL facility has progressed with several major upgrades, the first of which was IGISOL–2 where the experiment was moved to the accelerator target hall at the new science campus in Jyväskylä in 1991, gaining access to the K130 heavy ion cyclotron. A collinear laser spectroscopy line was moved from Daresbury in the UK to the IGISOL facility in the 1994, and the first collinear laser spectroscopy experimental results were published in 1997 [8]. In 2003 the upgrade to IGISOL–3 took place, with the main improvements including improved radiation shielding, the addition of a sextupole ion guide extraction and the construction of the Cooler–Buncher. The most recent upgrade of the experiment is IGISOL–4, which involved a relocation to a new, purpose–built laboratory and a major re–design of the ion beam–line delivery system as well as the addition of a dedicated light–ion cyclotron, the MCC30/15 cyclotron (see section 3.1 for further details).

1.1 This work

This thesis details the underlying atomic and nuclear theory behind the interactions of a structured nucleus with its surrounding atomic electrons (chapter 2). It provides an overview of the IGISOL–4 facility (see section 3.1) as well as details of the collinear laser spectroscopy technique (section 3.3) and the re–establishment of the collinear laser spectroscopy experimental setup (section 5.1). Information on a new microcontroller based data acquisition system for laser spectroscopy is presented (chapter 3.4). This system provides photon 'time stamping' (with respect to the Cooler–Buncher release signal), a photon 'burst' counter and details on a new technique to search for hyperfine peaks.

This thesis emphasizes work on the latest addition to the facility, a novel electrostatic ion trap, the ConeTrap [9, 10, 11]. The construction and operation of this trap is described in this work (chapter 4), with simulations compared to observed behaviour at the IGISOL facility. The ConeTrap has been commissioned off–line with stable IGISOL beams (section 4.6) as well as successfully employed during on–line spectroscopy experiments in 2014/2015. Investigations into critical ConeTrap behaviour, employing radioactive ions are presented in section 5.2. Future developments towards in–trap laser spectroscopy employing ion detection are also explored.

New laser spectroscopy measurements for ^{101,107}Mo are presented (section 5.1) as well as the first collinear laser resonance detection on ions successfully extracted from the ConeTrap (section 5.4). The observations of a resonant optical pumping effect on yttrium ions in the Cooler–Buncher are also presented (section 5.2). The conclusions and future prospects of this work are presented in chapter 6.

Chapter 2

Theoretical Background

2.1 Nuclear structure

2.1.1 Nuclear properties

Experimentally stable atomic nuclei, of atomic mass, A, are found to possess a radius of approximately $r_0 A^{\frac{1}{3}}$, where $r_0 = 1.25$ fm. The nuclear density is thus (experimentally) constant for all nuclei. However at the limit of the nuclear extent a diffuse surface is observed, rather than a sharp edge. The radial distance over which the nucleon density drops from 90% to 10% of its central density is known as the skin thickness, t. The nucleons are bound by the nuclear force, which unlike the electromagnetic force, only acts over short distances, being attractive between 0.7–2 fm and becoming repulsive below 0.7 fm (as determined by nucleon–nucleon scattering experiments). This force confines the nucleons within the nucleus and acts on protons and neutrons equally, but varies depending on the spin alignment between the nucleons (and their orbital angular momenta). The repulsive and attractive nature of the force led to the concept of a nuclear equilibrium where a nucleon within a nucleus maintains an average distance with its neighbours, leading to a *saturation* of the force, independent of A. This is shown by the relatively constant nuclear matter density and the low variation in nuclear binding energies per nucleon for $A > 20$. The force also contains a tensor component, which does not conserve orbital angular momentum. The nuclear force was initially modeled by the exchange of large virtual bosons (mesons), first proposed by Hideki Yukawa in 1934, and this exchange model was supported by the experimental

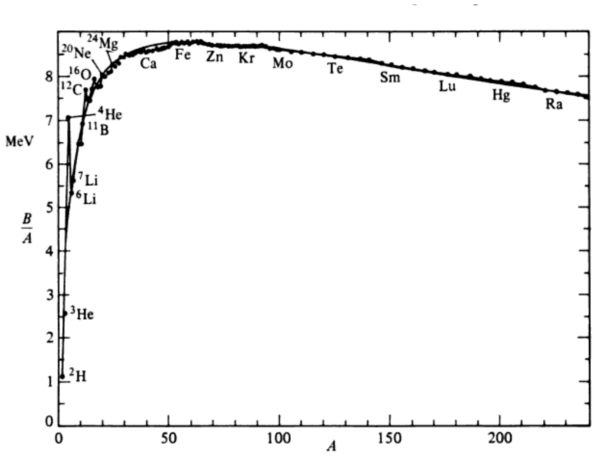

Figure 2.1: A plot of the binding energy per nucleon for increasing nuclear mass number A, reproduced from [12].

observation of the force saturation and a strong backward peak in neutron–proton scattering experiments. The subsequent discovery of quarks and gluons led to a greater understanding of the internal structure of both nucleons and mesons.

Macroscopic properties: nuclear mass and binding energy

The nuclear binding energy per nucleon for the region $A > 20$ is smooth with increasing nucleon number, with only small structural deviations as shown in figure 2.1. The observation of sharp radial changes around the so called 'magic numbers' contributed to the development of the nuclear shell model, where protons and neutrons are separated into distinct orbital energy levels. The simplest independent particle model describes the properties of nuclei through single particle behaviour of unpaired nucleons in the valence shells. This model is found to accurately predict structure in light nuclei and near shell gaps. In the model each nucleon has an orbital angular momentum, $\mathbf{l}$, and an intrinsic spin, $\mathbf{s}$, which couple to give the nucleons total angular momentum, $\mathbf{j}$. The total nuclear angular momentum is denoted as $\mathbf{I}$, the nuclear spin and is given by $\mathbf{I} = \sum_i \mathbf{j_i}$, where $\mathbf{j_i}$ represent the angular momenta of each individual nucleon.

The binding energy is the difference of the summation of individual nucleon masses from that of the nuclear mass. Masses were one of the first nuclear properties to be measured to a modest precision (in mass spectroscopy), and were a key aspect in progressing the knowledge of nuclear structure. The mass energy of a nuclide, $m_N c^2$,

is given by

$$m_N c^2 = m_A c^2 - Z m_e c^2 + \sum_{i=1}^{Z} B_i, \tag{2.1}$$

where $m_A c^2$ is the atomic mass energy, $Z m_e c^2$ is the total mass energy of Z electrons and B_i is the binding energy of the ith electron. The atomic binding energies are usually of the order 10–100 eV and for heavy nuclei only constitute a 1 part in 10^6 contribution. The binding energy, B_N of a nucleus ${}^{A}_{Z}X_N$ is given by

$$B_N = [Z m_p + N m_n - (m_{^A X} - Z m_e)]c^2. \tag{2.2}$$

The binding energy curve, figure 2.1, reaches a peak around $A = 60$, where the nuclei are most tightly bound. This curve shows that energy can be liberated through fusion for light nuclei, and by fission for heavier nuclei.

The semi–empirical mass formula was one of the first attempts to explain the small variations in the nuclear binding energy, estimating the nuclear masses based on the number of protons and neutrons [13]. This formula is based on a liquid–drop model, which treats the nucleus as a drop of incompressible nuclear fluid (protons and neutrons) bound by the nuclear force. The formula is given as

$$B_N = a_v A - a_s A^{2/3} - a_c Z(Z-1)A^{-1/3} - a_{sym}\frac{(A-2Z)^2}{A} + \delta, \tag{2.3}$$

where $a_v A$ is the volume term. The term is proportional to A (and not A^2) due to the short range nature of the nuclear force causing nucleons to only interact strongly with their closest neighbours. The a_s is the surface term coefficient, this represents a contribution due to the surface nucleons having less neighbouring nucleons, hence a lower binding energy. The Coulomb term, a_c, adds a contribution for electrostatic repulsion between 2 or more protons, assuming a sphere of uniform charge density. The asymmetry coefficient, A_{sym}, term represents a contribution due to the Pauli exclusion principle and the protons and neutrons filling separate 'pools' of energy levels. The final term δ is the coupling term which accounts for even–A nuclei and the contributions due to the difference in energy between proton–proton/neutron–neutron pairs and proton–neutron pairs. This term is positive for odd–odd nuclei, negative for even–even and zero for even–odd nuclei. The last two terms represent corrections taken from the shell model. The values for the constants may be obtained by fitting to nuclear binding energy per nucleon data, with values typically close to $a_v = 15.5$ MeV,

$a_s = 16.8$ MeV, $a_c = 0.72$ MeV, $a_{sym} = 23$ MeV. The δ term is zero for odd–A nuclei, $\delta = +a_p A^{-\frac{3}{4}}$, for even–even nuclei and $\delta = -a_p A^{-\frac{3}{4}}$ for odd–odd nuclei ($a_p = 34$ MeV) [13].

The spatial extent of the nucleus is a fundamental property that can be measured and reproduced in models. The mean–square charge radius or root–mean–square (rms) charge radius of a nucleus gives a description of the proton distribution, the mean is used as the nucleus does not possess a well defined boundary. This is the second radial moment of the charge distribution and is usually the most readily obtainable and accurate description of the nuclear spatial extent from experimental techniques. For a sphere of radius R with a constant charge distribution the mean–square charge radius is given by

$$\langle r^2 \rangle = \frac{\int_0^R r^2 \rho(r) dr^3}{\int_0^R \rho(r) dr^3} = \frac{3}{5} R^2 = \frac{3}{5} r_0^2 A^{\frac{2}{3}}, \tag{2.4}$$

where ρ is the charge distribution, hence the integral in the denominator is just the nuclear charge Ze. This represents the mean–square charge radius for the liquid–drop model (where the surface term leads to spherical nuclei). The differential effect for small changes in A is

$$\delta\langle r^2 \rangle = \frac{2}{5} r_0^2 A^{-\frac{1}{3}} \delta A. \tag{2.5}$$

Observations of deviations from this liquid–drop model prediction infer the presence of microscopic nuclear structure features such as the development of neutron skins, deformation (see section 2.1.3), nucleon pairing and shell closures. Absolute values for the mean–square charge radii may be obtained from K_α X–ray data, muonic X–ray data and electron–scattering experiments, however these techniques require either bulk material samples or long–lived isotope samples, making them impractical for studies of weakly produced, short–lived isotopes. Absolute values may also be extracted from Mössbauer spectroscopy however the range of elements suitable for study with this technique is limited, and usually requires bulk samples. Electron scattering experiments reveal the nuclear charge distribution $\rho(r)$, whereas electronic K_α X–ray provides changes in mean–square charge radii $\delta\langle r^2 \rangle$ between isotopes but with modest accuracy. Transitions in muonic systems are heavily dependent on the size of the nucleus, and a Barrett radial moment [14] may be model–independently determined from the experimental transition energy, giving an Barrett equivalent radius (the radius of

a sphere with constant charge density that provides the required Barrett moment).

2.1.2 The shell model

The shell model was proposed to explain the occurrence of the nuclear 'magic numbers' (shell closures) at N,Z = 2, 8, 20, 28, 50, 82, 126 where the liquid drop model is observed to underestimate the binding energies, even more so for 'doubly magic' nuclei with magic numbers of both protons and neutrons. These nuclei are more stable, as indicated through the enhanced natural abundances of nuclei with a magic number of protons or neutrons. There are also characteristic jumps in the nucleon separation energies at the magic numbers, similar to the changes in ionisation energy at closed shells in the atomic shell model. The nuclear shell model is analogous to the atomic model, where the nucleons fill shells of progressively higher energies above an inert core. However, unlike the atomic electrons, the nucleons in the nucleus move in a potential they themselves create. The nucleons are described by the quantum numbers n, l, j (just like the wavefunctions of individual electrons in atomic physics). The protons pair and neutrons pair (in spin up and spin down partners) to fill the shells. In the basic (extreme single particle) shell model only the unpaired valence nucleons contribute to the total angular momentum of the nucleus, and the magic numbers correspond to major shell closures. The nucleons take well–defined spatial orbits, and are able to move unhindered by each other in low–lying orbits as the Pauli exclusion principle prevents the nucleons from scattering between occupied orbitals. The description of the potential has important physical consequences, for instance the infinite well potential possesses a sharp cut off, which the observed nuclear potential does not. However a harmonic oscillator potential possesses an overly soft cut–off compared to the observed nuclear potential. The energy levels can be calculated by solving the Schrödinger wave equation, usually with a Woods–Saxon potential function (equation 2.6), with the addition of a spin–orbit coupling term to correctly reproduce the sub–shell separations. This coupling term leads to the large energy gaps present at the observed magic numbers, where nuclei are found to be more stable and calculations match observed behaviour. The Woods–Saxon potential plus coupling term is given

by

$$V(r) = -\frac{V_0}{1 + exp(\frac{r-R}{t})} + V_{LS}\mathbf{l}\cdot\mathbf{s}, \tag{2.6}$$

where V_0 represents the potential well depth ($\sim$ 50 MeV), R is the nuclear radius, t is the nuclear surface thickness ($\sim$ 0.5 fm) and V_{LS} is the strength of the potential due to the spin–orbit coupling. The nucleon–nucleon spin orbit term leads to a splitting of degenerate l states into the j states with degeneracy $(2j+1)$ from the $m_j = 0, \pm 1 \cdots \pm j$ values (as with this coupling scheme m_s and m_l are no longer good quantum numbers).

The shell model can explain energy levels within nuclei, whereby unpaired nucleons are raised to higher energy states to create the excited states. Alternatively nucleon pairs can be broken to produce excited states. The physical energy states are often described by a linear combination of pure shell–model state wave functions. The model can also provide the spins, parities and magnetic moments (see next section) of the nuclear ground states for many odd–A isotopes.

Magnetic dipole and electric quadrupole moments

The extreme single particle model can provide estimates for the nuclear dipole moments (known as Schmidt estimates) and nuclear quadrupole moments. The nuclear magnetic dipole moment, $\boldsymbol{\mu}$, is predicted to arise from the magnetic moments of the unpaired (valence) nucleons, as

$$\boldsymbol{\mu} = g_l\mu_N\mathbf{l} + g_s\mu_N\mathbf{s}, \tag{2.7}$$

where g_l and g_s are the gyromagnetic ratios (g–factors) of the orbital and intrinsic spin angular momentum, respectively and $\mu_N = \frac{e\hbar}{2m_p}$ is the nuclear magneton. An orbiting proton produces a magnetic field along with the intrinsic spin ($s = \frac{1}{2}$) generating an intrinsic magnetic field. The g–factors result from the way the individual nucleons contribute to the total magnetic moment and so contain information on the detailed nucleon structure of the nucleus. Neutrons do not provide any orbital contribution as they have no charge so $g_l(n) = 0$ for neutrons and $g_l(p) = 1$ for protons. Both protons and neutrons provide spin contributions with $g_s(p) = 5.5858$ and $g_s(n) = -3.8261$. In the nucleus a magnetic dipole moment exists only if the nuclear spin, I, is greater than or equal to $\frac{1}{2}$. The interaction energy of the magnetic moment with an external magnetic field $\mathbf{B}$ is $\boldsymbol{\mu}\cdot\mathbf{B}$ or (if $\mathbf{B}$ is in the direction of the z axis) equal to $\mu_z\mathbf{B}$. Thus

the observed moment is the expectation value of μ_z (the z–direction component of the dipole operator), which is $< jm|\hat{\mu}_z|jm >$ with the odd nucleon in state $|jm >$. The magnetic moment is defined as the maximum value of $< jm|\hat{\mu}_z|jm >$ and is thus

$$\mu = \frac{1}{j+1} < \boldsymbol{\mu} \cdot \mathbf{j} >= \frac{\mu_N}{j+1} < (g_l \mathbf{l} + g_s \mathbf{s}) \cdot \mathbf{j} > . \tag{2.8}$$

This leads to two solutions for $j = l \pm \frac{1}{2}$, which are known as the Schmidt estimates or limits. Measured moments are generally found between these limits, suggesting that the wave function of the nuclear state cannot be simply described by the wave function of the odd nucleon. The magnetic moment is influenced by the presence of other nucleons which can be accounted for using effective single–particle magnetic moment μ^{eff} where the single nucleon g_s factors are reduced to $\sim 70\%$ of their free nucleon values.

In the extreme single particle shell model pairing of like nucleons to $J = 0$ gives rise to a spherical mass distribution and a spherical potential. If an odd valence nucleon is present it moves within this spherical potential, however the spatial distribution of the nucleon is non spherical (unless $I = \frac{1}{2}$). The single–particle quadrupole moment,$Q_{s.p}$ for an unpaired nucleon in an orbit with an angular momentum, $\mathbf{j}$, is

$$Q_{s.p} = -e_j \langle r_j^2 \rangle \frac{(2j-1)}{2j+2}, \tag{2.9}$$

where e_j is the effective charge and $\langle r_j^2 \rangle$ is the mean–square charge radii of the single nucleon. So for $J = \frac{1}{2}$, $Q_{s.p}$ is zero. For odd–A, odd–N nuclei the quadrupole moment is predicted to be zero as the neutron has zero charge. More generally a non–spherical distribution of charge in the nucleus gives rise to an (intrinsic) electric quadrupole moment, Q_0 with the classical definition given by

$$Q_0 = \int \rho(r)(3z^2 - r^2) d\tau, \tag{2.10}$$

where z chosen as the symmetry axis of the nuclear shape and the integral is over the enclosed volume τ. The quadrupole moment gives a direct measure of the charge distribution deformation from spherical, however large observed differences between some measured and calculated (from the single particle model) quadrupole moments led to the development of models with collective motion (see section 2.1.3). The intrinsic quadrupole moment is not directly measured, instead the *spectroscopic* quadrupole

moment, Q_S, is measured, which is the projection of Q_0 onto the lab axis. For axially symmetric nuclei this is given by

$$Q_s = Q_0 \frac{3K^2 - I(I+1)}{(I+1)(2I+3)}, \tag{2.11}$$

where K is the projection of J along the symmetry axis, see figure 2.2. A spectroscopic quadrupole moment only exists if the nuclear spin $I \geq 1$, hence a spin 0 or $\frac{1}{2}$ may possess an intrinsic deformation but it cannot be measured through the quadrupole moment.

2.1.3 Collective motion, deformation and the Nilsson model

Collective motion and deformed shell models were introduced to account for the discrepancies between measured and calculated quadrupole moments (mainly for middle shell nuclei) and to explain the observation of low–lying 2^+ excitation states in even–even nuclei, that lie below the energy required to break a nucleon–nucleon pair. Collective motions often modeled as a vibrating/rotating nuclear liquid drop. Collective motion can be treated as vibrations around a spherical shape or a rotation of a deformed nuclei (a cranked model). In the vibrational model phononic excitations describe the energy levels, with vibrational level triplets formed from 2–phonon excitations. Many nuclei below A=150 show reasonable agreement with the vibrational model, where the energy of the 2–phonon state is about twice the energy of the single phonon state. The quadrupole moment of the first 2^+ state for (spherical) equilibrium shapes is approximately zero (giving further evidence for a vibrational model and a single phonon level causing the observed 2^+ state below the 2 MeV required to break a nucleon pair).

Rotational excitations are a form of collective motion observed only in nuclei with non–spherical equilibrium shapes as nuclear rotation is quantum mechanically forbidden around the symmetry axis. Deformed nuclei can be prolate ($\beta_2 > 0$) or oblate ($\beta_2 < 0$) in shape, where β_2 is defined below, and most typically described by axially symmetric quadrupoloids. In a triaxial nucleus none of the three principal axes are equal, the triaxiality parameter γ measures the deviation from an axially symmetric shape. In a rotating nucleus the nuclear spin, I, is no longer a good quantum number, the energy of the states is dependent on the orientation of the orbit and its overlap

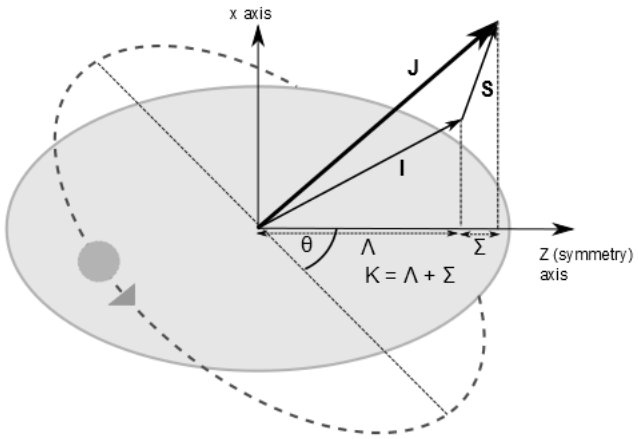

Figure 2.2: The projections of the angular momenta of a valence nucleon onto the symmetry axis of a prolate nucleus.

with the deformed nuclear core. The orientation is specified by the spin projection, K, onto the symmetry axis (see figure 2.2). The nucleons with orbits that have better overlap with the nuclear core will interact more strongly, i.e. in a prolate nucleus the low K values represent equatorial motion near the core and possesses a lower energy. Observing the ratios of the E(4^+) to the E(2^+) allows for identification between collective vibrations and rotations as well as giving an indication of how close to a collective rigid rotor a certain nuclei is behaving. In an adiabatic scenario (where the internal nucleon velocities are much greater than the collective motion) the rigid rotor model can be used to give reasonable limiting estimates of the rotational energy levels.

The deformed nucleus is often pictured as an quadrupoloid, with a surface described by equation 2.12 such that

$$R(\theta, \phi) = R_0[1 + \beta_2 Y_{20}(\theta, \phi)], \tag{2.12}$$

where Y_{20} is the $l = 2$ spherical harmonic and β_2 is the quadrupole deformation parameter. This leads to an alteration in the mean–square charge radii expression of 2.5 to give

$$\langle r^2 \rangle = \langle r^2 \rangle_{sph} + \frac{5}{4\pi} \langle r^2 \rangle_{sph} \beta_2^2, \tag{2.13}$$

where $\langle r^2 \rangle_{sph}$ is the radius of a spherical nucleus with the same volume. This relates the mean–square charge radii (and importantly the changes in mean–square charge radii) to the deformation of the proton distribution.

Nuclear deformation may be static or dynamic, where the nuclear shape oscillates around an equilibrium, leading to changes in observed nuclear radii. Dynamic nuclear deformation consists of time dependent fluctuations, which can affect the observed nuclear radius. The quadrupole deformation parameter, β_2, describes magnitude of the quadrupole deviation from a spherically symmetric nucleus and can be written as a sum of the static and dynamic contributions $\langle\beta_2^2\rangle = \langle\beta_2^{stat}\rangle^2 + \langle\beta_2^{dyn}\rangle^2$, where β_2^{dyn} possesses a time dependence.

Extension of shell model to deformed potential.

The Nilsson model extends the single particle shell model to one with a deformed nuclear potential (many forms of potential can be used from the harmonic oscillator to a Woods–Saxon potential). The solutions to the Nilsson Hamiltonian provide descriptions of how deformation affects the nuclear energy levels, a Nilsson diagram plots the changes in the energy levels (for positive and negative parity states) as a function of the deformation parameter, an example of one is shown in figure 2.3. The Nilsson orbitals for large deformations are described by the asymptotic Nilsson quantum numbers, $K^\pi[Nn_z\Lambda]$, where π is the parity of the state, N is the principle quantum number, n_z is the number of nodes the wave–function possesses along the symmetry axis and Λ is the projection of the orbital angular momenta onto the symmetry axis (where $K = \Lambda + \Sigma$), see figure 2.2. The principle quantum number, N, and the parity of the state relate to Λ and n_z such that if N is even then $\Lambda + n_z$ is even, and if N is odd then $\Lambda + n_z$ is odd. Mixing between similar states can occur, with physical energy levels often described as a superposition of several pure Nilsson states. The mixing occurs between states of similar K^π and spin orientation, with increased mixing as the energy separation between the states reduces. However, due to the Pauli exclusion principle, no two states can share the same quantum number and parity, so a 'pseudo–crossing' is formed at which the degree of mixing and character in the two states is interchanged.

The droplet model

The droplet model provides a description of macroscopic properties of nuclei, such as the extent of the proton and neutron distributions and their root mean–square charge

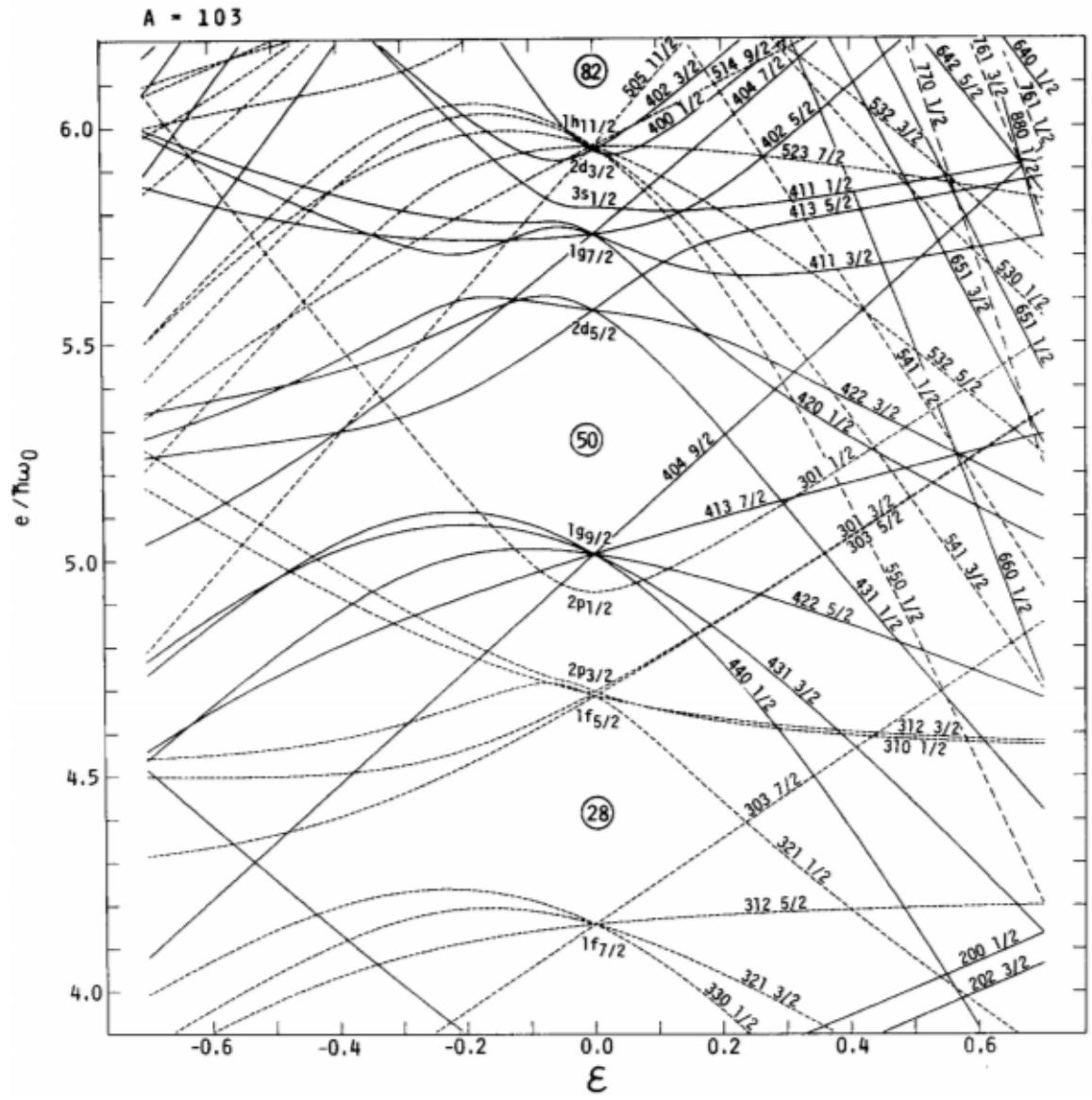

Figure 2.3: A Nilsson diagram of single particle levels for A=103, as a function of the deformation parameter ϵ, where $\epsilon \simeq 0.95\beta_2$. The positive parity states are shown as solid lines and the negative are shown as dotted lines and the circled numbers represent spherical shell gaps [15].

radii. Originally developed by Myers and Swiatecki [16] as a refinement to the liquid drop model (LDM), it includes separate distributions for protons and neutrons and combines a macroscopic description with deformation effects. This model was extended to nuclei of arbitrary shape [17], and deals with smooth, average nuclear properties that do not include shell effects (although extensions to include microscopic shell model effects have been attempted [18]). The proton and neutron distribution radii are found by minimising the macroscopic energy of the system, described by a combination of a volume energy, a surface energy and a Coulomb energy term. This results in the prediction of a neutron skin for many heavy, neutron–rich nuclei due to the greater neutron distribution radius and a small redistribution of nucleons due to the Coulomb force. The droplet model provides an accurate description of the observed mean–square charge radii compared to the liquid drop model, where the observed isotopic shift in mean–square charge radii was on average half that predicted by the LDM. The droplet model also leads to a better description of the observed isotone shifts, which on average where greater than predicted by the LDM. This improved description was due to the extra free parameter allowing for differences in proton and neutron distributions, leading to proton redistribution and the development of a neutron skin with excess neutrons.

The size of the nucleus (protons and neutrons together) can be calculated from the expression

$$R = r_0 A^{\frac{1}{3}}(1+\epsilon), \tag{2.14}$$

where,

$$\begin{aligned}
\bar{\epsilon} &= (-2a_2 A^{-\frac{1}{3}} B_s + L\delta^2 + c_1 Z^2 A^{-\frac{4}{3}} B_c)/K, \\
\bar{\delta} &= \frac{I + \frac{3}{16}(\frac{c_1}{Q}) Z A^{-\frac{4}{3}} B_v}{1 + \frac{9}{4}(\frac{J}{Q}) A^{-\frac{1}{3}} B_s}, \\
I &= \frac{N-Z}{A}.
\end{aligned}$$

The parameter $\bar{\epsilon}$ is the "bulk–density excess" and $\bar{\delta}$ is the "bulk–neutron excess"; B_s represents the ratio of the surface area of a deformed shape with a sphere of equal volume, while B_c represents a Coulomb energy term and B_v represents the changes in the Coulomb potential over the surface when a nucleus is deformed. The term r_0 is the nuclear radial constant, a_2 is a surface energy coefficient, L is the density symmetry

coefficient, c_1 is the Coulomb energy coefficient, K is the compressibility coefficient, Q is the effective surface stiffness, J is the symmetry energy coefficient and b is the nuclear surface diffuseness [19]. Many different parameterisations exist for the droplet model, refined to match different data sets.

The rms radii can be expressed as

$$\langle r^2 \rangle = \langle r^2 \rangle_u + \langle r^2 \rangle_r + \langle r^2 \rangle_d, \tag{2.15}$$

where $\langle r^2 \rangle_u$ is the contribution from the size and shape of the uniform distribution, $\langle r^2 \rangle_r$ is the redistribution term and $\langle r^2 \rangle_d$ is the diffuseness contribution. These 3 terms are given by

$$\begin{aligned}
\langle r^2 \rangle_u &= \frac{3}{5}R^2(1 + \alpha_2^2 + \frac{10}{21}\alpha_2^3 - \frac{27}{35}\alpha_2^4 + \frac{10}{7}\alpha_2^2\alpha_4 + \frac{5}{9}\alpha_4^2 \cdots) \\
\langle r^2 \rangle_r &= \frac{12}{175}C'R^2(1 + \frac{14}{5}\alpha_2^2 + \frac{28}{15}\alpha_2^3 - \frac{29}{5}\alpha_2^4 + \frac{116}{15}\alpha_2^2\alpha_4 + \frac{70}{26}\alpha_4^2 \cdots) \\
\langle r^2 \rangle_d &= 3\sigma^2,
\end{aligned}$$

where the α_2, α_4 and α_6 coefficients are of relative order ϵ, ϵ^2 and ϵ^3, $C' \simeq 0.0156ZA^{-1/3}$ and $\sigma = 0.99$ fm for all nuclei.

Many extensions to the droplet model have been developed, including macroscopic–microscopic finite–range droplet models that include shell model single particle potentials to calculate ground state masses [20]. Other approaches using similar macroscopic and microscopic contributions also exist, including potential energy surface calculations from the finite–range liquid drop model with a deformed Woods–Saxon potential [21]. Full, self–consistent mean–field calculations are further employed to calculate nuclear properties, making use of symmetries in the mean field to reduce computing time. The nucleons are described as relativistic particles moving independently in an average potential, modeled with the exchange of mesons. The relativistic Dirac single particle equation is solved for the system, with increasing number of nucleons leading to a much greater increase in calculation time. The Hartree–Fock method provides a way to solve the time independent wave equations, with the chosen mean field interaction. Two such examples are the Skyrme interaction, where the Sly4 parameterisation was used, for example, to calculate nuclear binding energies in reference [22] and the Gogny–D1s interaction used in reference [23] where charge radii were calculated for even–even nuclei and compared to available data.

2.1.4 Nuclear decay and electromagnetic transition rates

Radioactive nuclei can decay via various processes, gamma ray emission, beta decay, alpha decay, internal conversion, electron capture and proton/neutron emission. Heavy nuclei can also undergo fission, whereby the nucleus splits into daughter fragments. The initial states all have a lifetime associated with them, determined by the wave–functions of the initial and final states and of the decay commuting the transition. Analogous to transitions between atomic states, excited nuclear states can decay via electromagnetic transitions, potentially in competition with internal conversion or beta decay. When nuclei are produced in nuclear reactions or through nuclear decay they are often formed in excited states, which decay rapidly by gamma ray emission (10^{-9}–10^{-15} s). The photon energies can be from the X–ray region ($\sim$ 100 keV) up to tens of MeVs. Studying gamma rays through gamma ray spectroscopy has provided a wealth of information on the energies of excited states, their lifetimes, nuclear spins and parities, magnetic moments, nuclear deformation parameters and rotational/vibrational collective motion.

Photons have an intrinsic spin $\mathbf{s} = 1$ and remove a total angular momentum $\mathbf{L} = \mathbf{l} + \mathbf{s}$ during a transition, where $\mathbf{l} = \mathbf{r} \times \hbar\mathbf{k}$ and $\mathbf{k}$ is the electromagnetic wave vector. Monopole ($L = 0$) radiation is forbidden as the $s = 1$ and l cannot be coupled to give zero. An electromagnetic transition is described by two characteristic types, magnetic (M) and electric (E), both being two independent solutions for spherical waves in free space (with their own rules for parity changes between initial and final states). The operators E1 and M1 conventionally represent the electric and magnetic dipole transitions ($\mathbf{l} = 0$). E2 and M2 operators are the quadrupole transitions, with the increasing number representing a higher order multiple of the transition. The gamma ray transition rates are given by the Fermi golden rule

$$\lambda = \frac{2\pi}{\hbar} \left| \int \psi^* M(\sigma L) \psi \mathrm{d}\nu \right|^2 \frac{\mathrm{d}N}{\mathrm{d}E},$$
$$M(\sigma L) \sim \frac{1}{k} (kr)^L P_l(cos(\theta)),$$

where $M(\sigma L)$ is the transition operator for $\sigma =$ E or M and $\frac{\mathrm{d}N}{\mathrm{d}E}$ is the density of final states. Gamma ray transition rates for single particle transitions are referred to as Weisskopf estimates. The Weisskopf estimates predict that the higher order transition rates are increasingly hindered as the photon has to carry away more orbital angular

momentum. Generally a transition will decay via the allowed transition with the lowest L value. Collective motion of many protons can lead to 'enhanced' rates for the electric multipole transitions compared to the Weisskopf estimates, with many protons taking part in the transition the estimates need to be modified by a factor of N^2 (so a enhancement of 100 would be due to 10 protons moving collectively).

Experimentally E1 transitions are often found to be inhibited compared to the Weisskopf transition rate estimates, while E2 rates are often enhanced, leading to M1 and E2 transitions having comparable rates. Enhanced E2 transitions are often found in rotational bands.

The reduced quadrupole transition probabilities, B(E2), are often larger than predicted by Weisskopf estimates and reflect the quadrupole distortion of the nuclei. The quadrupole deformation parameter, β_2 is related to the B(E2) (reduced matrix element) values by

$$\beta_2 = \frac{4\pi}{3ZR^2}[B(E2)/e^2]^{\frac{1}{2}}, \tag{2.16}$$

where $R = r_0 A^{1/3}$.

2.2 Atomic hyperfine structure

The hyperfine structure (HFS) is analogous to the well known fine structure splitting caused by the interaction of the electron spin with the magnetic field of the electron cloud resulting in a coupling of the intrinsic electron spin and its orbital angular momentum. The hyperfine splitting effect is many orders of magnitude smaller than the fine structure energy level splitting. The effect can be treated as the nuclear interaction with a multipole expansion of the electromagnetic field produced by the valence electrons across the nucleus. The monopole term relates to the charge (Ze) of the nucleus and the HFS effect tends to be dominated by the magnetic dipole and electric quadrupole terms, higher order terms are found to be negligible in most cases [24].

The interaction of the electromagnetic field produced by the atomic electrons with the nuclear charge and magnetism distributions results in the splitting of the J states in the atomic energy levels. This results from the coupling between the nuclear and electron angular momenta, giving a total angular momentum, $\mathbf{F} = \mathbf{I} + \mathbf{J}$, about which

the total electron angular momentum, **J**, and the nuclear spin, **I**, precess.

2.2.1 The magnetic dipole interaction

The nuclear magnetic moment is given by equation 2.7, and is related to the nuclear spin, I, by

$$\boldsymbol{\mu_I} = g\mu_N \mathbf{I}. \tag{2.17}$$

In states where J of the electrons is non–zero an effective magnetic field $\mathbf{B}_e$ can be produced at the nucleus. The nuclear magnetic dipole moment interacts with this magnetic field, leading to a splitting in the energy levels, appearing as a dipole term in the multipole expansion. The dipole interaction Hamiltonian can be expressed as

$$\hat{H} = -\boldsymbol{\mu} \cdot \mathbf{B}_e. \tag{2.18}$$

Since the magnetic field $\mathbf{B}_e$ is created by the atomic electrons (and dependent on **J**) and μ is proportional to **I**, it follows that equation 2.18 can be written as

$$\hat{H} = A\mathbf{I} \cdot \mathbf{J}, \tag{2.19}$$

where A is the magnetic hyperfine constant which can be determined from experimental measurements. This IJ coupling form assumes that the hyperfine splitting is small compared to fine structure, and treated as a small perturbation on the atomic states, which is produced by a net magnetic field along J (all other field components average out to zero). The quantum mechanical expectation value of the term $\mathbf{I} \cdot \mathbf{J}$ can be expressed as

$$\langle \mathbf{I} \cdot \mathbf{J} \rangle = \frac{1}{2}[F(F+1) - I(I+1) - J(J+1)]. \tag{2.20}$$

Therefore the energy splitting is given by the expectation value of the Hamiltonian, which can be written as

$$\Delta E = A\langle \mathbf{I} \cdot \mathbf{J} \rangle = \frac{AK}{2}, \tag{2.21}$$

where $K = F(F+1) - I(I+1) - J(J+1)$. If J is greater than I then there are $|2I+1|$ components of the hyperfine multiplet (or $|2J+1|$ if I is greater than J).

2.2.2 Electric quadrupole interaction

If the nuclear spin $I \geq 1$ then a nuclear spectroscopic quadrupole moment, Q_s, may exist and cause a splitting in the presence of a non–spherical electric field. To produce

an electric field gradient at the nucleus the orbital electrons must possess $J \geq 1$. The nucleus can be considered as a finite charge distribution (with the nuclear centre at the origin) of charge density $\rho(r, \theta, \phi)$ and volume τ. The potential at the origin can be expanded as

$$V = V_0 \left(\frac{\partial V}{\partial z}\right)_0 z + \frac{1}{2}\left(\frac{\partial^2 V}{\partial x^2}\right)_0 x^2 + \frac{1}{2}\left(\frac{\partial^2 V}{\partial y^2}\right)_0 y^2 + \frac{1}{2}\left(\frac{\partial^2 V}{\partial z^2}\right)_0 z^2 \ldots, \tag{2.22}$$

where the $(\partial V/\partial x)_0 = (\partial V/\partial y)_0 = 0$ and $\partial^2 V/\partial x^2 = \partial^2 V/\partial y^2$ in the case of axial symmetry of the **E** field. If the source of the **E** field is external to the volume, τ, then $\nabla \cdot \mathbf{E} = 0$ and $\partial^2 V/\partial x^2 = -\frac{1}{2}\partial^2 V/\partial z^2$, so equation 2.22 reduces to

$$V = V_0 - E(z)_0 z - \frac{1}{4}\left(\frac{\partial \mathbf{E}}{\partial z}\right)_0 (3z^2 - r^2) \ldots. \tag{2.23}$$

The energy, E, of the charge distribution in the electric field is

$$E = \int \rho V d\tau = V_0 q - (E_z)_0 d_z - \frac{1}{4}\left(\frac{\partial \mathbf{E}}{\partial z}\right)_0 eQ + \ldots, \tag{2.24}$$

where $q = \int \rho d\tau$ is the total charge, $d_z = \int \rho z d\tau$ is the z component of the electric dipole moment (expected to be zero due to time reversal invariance) and Q is the electric quadrupole moment given by

$$Q = \frac{1}{e}\int \rho(3z^2 - r^2) d\tau. \tag{2.25}$$

This is the classical representation of the quadrupole moment, quantum mechanically we define the electric quadrupole operator as

$$\hat{Q} = 3z^2 - r^2 = r^2\sqrt{\frac{16\pi}{5}} Y_{20}. \tag{2.26}$$

The expectation value of the quadrupole interaction Hamiltonian $\hat{H}$ acting on a state gives the energy splitting as

$$\Delta E_E = \langle \alpha I J F M_F | \hat{H}_E | \alpha I J F M_F \rangle = \frac{B}{4} \frac{\frac{3}{2}K(K+1) - 2I(I+1)J(J+1)}{I(2I-1)J(2J-1)}, \tag{2.27}$$

where α represents non–angular quantum numbers, K is as defined earlier, and B is the electric quadrupole hyperfine constant and is defined as

$$B = eQ_s \left\langle \frac{\partial^2 V}{\partial z^2} \right\rangle. \tag{2.28}$$

2.2.3 Evaluation of hyperfine parameters and the hyperfine anomaly

The nuclear magnetic and quadrupole moments can be extracted for a given isotope as long as the value for another (usually stable) isotope is known. These can be extracted using the ratios of the A or B coefficients as

$$\frac{A^N_{u,l}}{A^{N'}_{u,l}} = \frac{\mu^N/I}{\mu^{N'}/I'}, \tag{2.29}$$

and

$$\frac{B^N_{u,l}}{B^{N'}_{u,l}} = \frac{Q^N}{Q^{N'}}. \tag{2.30}$$

For these ratios to hold the magnetic field and the distribution of magnetism must be constant across the nucleus. The magnetic hyperfine anomaly arises due a non–uniform distribution of magnetism across the nucleus. This difference leads to a correction to the A factors which is usually less than 1% [25]. This effect is described by the hyperfine anomaly parameter $\Delta^{A,A'}$ and is used as a correction to equation 2.29 to give

$$\frac{\mu_I(A')}{\mu_I(A)} = (1 + \Delta^{A,A'})\frac{A_{A'}I_{A'}}{A_A I_A}, \tag{2.31}$$

where

$$1 + \Delta^{A,A'} = \frac{1 + \epsilon_{A'}}{1 + \epsilon_A} \sim 1 + \epsilon_{A'} - \epsilon_A, \tag{2.32}$$

and $\epsilon_{A'}$ and ϵ_A represents the Bohr–Weisskopf [25] factors for the isotopes A' and A respectively.

2.2.4 First order hyperfine splitting

The combination of the magnetic dipole and electric quadrupole interactions gives rise to the first order hyperfine splitting (in zero external magnetic field) which is expressed as

$$\frac{\Delta E}{h} = \frac{AK}{2} + \frac{B}{4}\frac{\frac{3}{2}K(K+1) - 2I(I+1)J(J+1)}{I(2I-1)J(2J-1)}. \tag{2.33}$$

The matrix elements of μ and Q_s are contained within the hyperfine constants A and B respectively, assuming the magnetic field from the electrons and the magnetization through the nuclear volume is constant. For a given transition between an upper (u) and lower (l) J states, the observed hyperfine peak frequencies are given by

$$\gamma = \nu + \alpha_u A_u + \beta_u B_u - \alpha_l A_l - \beta_l B_l, \tag{2.34}$$

where ν is the transition centroid and α and β are given by

$$\alpha_{u,l} = \frac{K}{2},$$
$$\beta_{u,l} = \frac{1}{4}\frac{\frac{3}{2}K(K+1) - 2I(I+1)J_{u,l}(J_{u,l}+1)}{I(2I-1)J_{u,l}(2J_{u,l}-1)},$$

with K evaluated for the upper or lower state respectively.

2.3 Isotope shift

The isotope shift is a shift in the hyperfine centroid of a given atomic transition observed along an isotope chain. It consists of two main components (to an excellent approximation), the field shift (FS) and the mass shift (MS) [26]. The mass shift dominates in lighter atoms whereas the field shift dominates in heavier atoms (with both being comparable around Z=30). The mass shift comprises of the specific mass shift (SMS) and the normal mass shift (NMS), together the total shift in frequency is shown in equation (2.35).

$$\delta\nu = \delta\nu_{NMS} + \delta\nu_{SMS} + \delta\nu_{FS}. \tag{2.35}$$

2.3.1 Field shift

The field shift of a transition arises due to the changes in the electrostatic potential experienced by the atomic electrons as the finite spatial distribution of the nuclear charge changes. This leads to alterations in the electronic binding potentials in the nuclear region and causes a small energy shift. Higher Z nuclei tend to have a greater extended charge distribution, leading to a more pronounced energy shift (and a large Z scaling). This results in the field shift tending to dominate in the $A > 100$ region. The dependence of the field shift on the changes in $\langle r^2 \rangle$ was shown by Bodmer [27].

For two isotopes of atomic mass A and A', where $A' > A$ (which is the convention adopted throughout this thesis), the field shift can be written as

$$\delta\nu_{fs} = \nu^{A'} - \nu^{A} = F_i \lambda^{A,A'}, \tag{2.36}$$

where F is the field shift factor, $\lambda^{A,A'}$ represents the Seltzer moment, which is a multipole expansion of the nuclear charge radius. This expansion takes into account

possible non–uniformity of the charge distribution across the nuclear shape, and is written as

$$\lambda^{A,A'} = \delta\langle r^2\rangle^{A,A'} + \frac{C_2}{C_1}\delta\langle r^4\rangle^{A,A'} + \frac{C_3}{C_1}\delta\langle r^6\rangle^{A,A'} \cdots , \tag{2.37}$$

where the C_i values are constants, tabulated for a large range of nuclei [28]. Since the Seltzer moment is dominated by the $\delta\langle r^2\rangle^{A,A'}$ term it can be re–written as

$$\lambda^{A,A'} = \delta\langle r^2\rangle^{A,A'}\left(1 + \frac{C_2}{C_1}\frac{\delta\langle r^4\rangle^{A,A'}}{\delta\langle r^2\rangle^{A,A'}} + \frac{C_3}{C_1}\frac{\delta\langle r^6\rangle^{A,A'}}{\delta\langle r^2\rangle^{A,A'}} + \cdots\right) = K(Z)\delta\langle r^2\rangle^{A,A'}. \tag{2.38}$$

The factor $K(Z)$ has to be calculated (which requires input from a nuclear model), however for light nuclei ($A \leq$150) $K(Z) \sim 1$, and even for nuclei in the ($A >$ 150) region the value only deviates from unity by a few percent, with little model dependence. Thus $\lambda^{A,A'}$ is often replaced by $\delta\langle r^2\rangle^{A,A'}$.

The field shift factor, F_i, is given by [29]

$$F_i = \frac{\pi a_0}{Z}\Delta\psi(0)^2 f(Z), \tag{2.39}$$

where $\Delta\psi(0)^2$ represents the change in the electronic density at the origin and contains information on atomic configuration mixing between the two states as well as electron screening changes. The $f(Z)$ is a correction factor for relativistic effects due to electron proximity to the nucleus. The factor, F_i contains all the atomic information while λ or $\delta\langle r^2\rangle^{A,A'}$ contains the nuclear contributions. Electron transitions involving changes in number of $s_{\frac{1}{2}}$ or $p_{\frac{1}{2}}$ produce the largest field shifts, courtesy of $s_{\frac{1}{2}}$ and $p_{\frac{1}{2}}$ electrons having a finite density at the origin.

2.3.2 The mass shift

The mass shift in a transition arises due to the changing number of neutrons affecting the center of mass motion and reduced mass. The normal component represents the shift due to the change in finite nuclear mass (reduced mass) and the specific mass shift represents the corrections due to correlated electron orbital motion. The mass shift can be expressed as

$$\delta\nu_{MS}^{AA'} = \frac{(A' - A)}{AA'}M = \delta\nu_{SMS}^{AA'} + \delta\nu_{NMS}^{AA'}, \tag{2.40}$$

where A and A' represent the masses of two isotopes, M is the isotope independent mass shift factor and $\delta\nu_{SMS}^{AA'}$ and $\delta\nu_{NMS}^{AA'}$ represent the specific and normal mass shifts

respectively. The normal mass shift (NMS) always produces a positive isotope shift (for $A' > A$). A positive isotope shift occurs if, within a transition, the heavier isotope is shifted to higher frequencies. The specific mass shift can produce either positive or negative shifts, depending on the transition studied.

Equation 2.40 can be obtained from energy considerations, taking the kinetic energy of an atom as

$$KE = \frac{\mathbf{p}_n^2}{2m_n} + \sum_i \frac{\mathbf{p}_i^2}{2m_e}, \tag{2.41}$$

where $\mathbf{p}_n$ and m_n are the momentum and mass of the nucleus and $\mathbf{p}_i$ and m_e are the momentum and mass of the orbital electrons. For a stationary atom the total momentum is conserved, $\mathbf{p}_n + \sum_i \mathbf{p}_i = 0$. This gives

$$\begin{aligned} KE &= \frac{(-\sum_i \mathbf{p}_i)^2}{2m_n} + \sum_i \frac{\mathbf{p}_i^2}{2m_e}, \\ &= \frac{\sum_i \mathbf{p}_i^2}{2m_n} + \frac{2\sum_{i<j} \mathbf{p}_i \mathbf{p}_j}{2m_n} + \sum_i \frac{\mathbf{p}_i^2}{2m_e}, \\ &= \frac{1}{2}\frac{m_n + m_e}{m_n m_e}\sum_i \mathbf{p}_i^2 + \frac{\sum_{i<j} \mathbf{p}_i \cdot \mathbf{p}_j}{m_n}. \end{aligned} \tag{2.42}$$

The first term in equation 2.42 represents the normal mass shift and the second term represents the specific mass shift. The specific mass shift depends on the products of the electronic momenta and hence the products of electronic wave functions.

Combining the field and mass shifts produces equation 2.43, where it can be seen that the change in mean–square charge radius can be calculated if the M_i and F_i factors are known.

$$\delta\nu_i^{A,A'} = M_i \frac{A' - A}{AA'} + F_i \delta\langle r^2 \rangle^{A,A'}. \tag{2.43}$$

2.3.3 The King plot technique

The King plot technique provides a means of evaluating the F and M parameters, provided accurate charge radii values for at least three of the isotopes (two isotope pairs) have been previously measured along with their isotope shifts. Such charge radii data can come from a combined analysis of K X–ray data, muonic X–ray data or electron scattering experiments [30]. Including this non–optical data has the advantage

that the F and M and $K(Z)$ are calibrated, providing a nuclear model–independent way of extracting the optical factors F_i and M_i from experimental data alone. The relative mass shifts are the same for all optical transitions of an element across the isotope chain, however the ratio of MS to FS can change depending on the transition.

In the King plot technique a modified isotope shift is plotted against a modified $\delta\langle r^2\rangle$, where the intercept gives the mass shift of the pair A,A' and the gradient gives F_i. The modification factor is

$$\mu^{A,A'} = \frac{AA'}{A'-A}\frac{A^{ref'}-A^{ref}}{A^{ref'}A^{ref}}, \tag{2.44}$$

where A^{ref} and $\mathrm{A}^{ref'}$ are a reference isotope pair. This leads to

$$\mu^{A,A'}\delta\nu^{A,A'} = \delta\nu_{MS}^{A^{ref},A^{ref'}} + \mu^{A,A'}F_i\lambda^{A,A'}, \tag{2.45}$$

where $\delta\nu_{MS}^{A^{ref},A^{ref'}}$ is the mass shift.

This plot can consist of points between adjacent isotopes, a ladder type, or between isotopes and a given reference isotope. The inclusion of the reference pair varies across the literature, but the modified isotope shift is plotted as this ensures that points obtained from various transitions still lie on a straight line.

For the case where no charge radii is available the plot can be evaluated between two transitions, j and i, equation 2.45 can be applied to both resulting in

$$\mu^{A,A'}\delta\nu_j^{A,A'} = \frac{F_j}{F_i}(\mu^{A,A'}\delta\nu_i^{A,A'}) + k(M_j - \frac{F_j}{F_i}M_i), \tag{2.46}$$

where

$$k = \frac{A^{ref'}-A^{ref}}{A^{ref}A^{ref'}}. \tag{2.47}$$

The gradient and intercept provide a relationship between the atomic parameters of the two transitions, the gradient is given by F_j/F_i and the intersection of the regression line is

$$y = (M_j - M_i\frac{F_j}{F_i})k. \tag{2.48}$$

Deviation from the linear relationship shows that second–order effects are present in the transitions (where the hyperfine splitting is comparable to the fine level splitting). In cases where no previous experimental data is available to form a King plot the electronic parameters F and M have to be calculated. Empirical estimates exist for M in simple transitions however the dependence on the specific electron correlations make

calculations difficult. The field shift parameter can be calculated using the Landé–Goudsmit–Fermi–Sergé (LGFS) formula, usually modified by a calculated electron shielding factor [26].

Chapter 3

Experimental set–up

3.1 The IGISOL facility

Since the mid 1990s a UK–Jyväskylä collaboration (including the University of Manchester) has been performing in–flight collinear laser spectroscopy on radioactive ion beams from the Ion Guide Isotope Separator On Line (IGISOL) facility, which is located at the accelerator laboratory (JYFL) in the University of Jyväskylä, Finland. The IGISOL facility has recently resumed operation after its latest upgrade, making this the 4th generation of the facility. The final collinear laser spectroscopy experimental campaign at IGISOL–3 was completed in 2010 with the upgrade and relocation to a new, purpose built laboratory commencing soon afterwards. A major addition to the new laboratory was a dedicated light ion cyclotron for the IGISOL group which, in conjunction with beams from the existing K130 cyclotron, provides unparalleled beam time for experimental campaigns (section 3.1.1). The new laboratory provides greater space for experimental equipment, enabling a major redesign of the main beam–line. A low energy section provides optical access to multiple sections of the beam–line and access to ion beams at different energies. The layout of the new laboratory is shown in figure 3.1.

The IGISOL technique was developed in the 1980s, and differs from conventional ISOL techniques. The primary beam impinges on a thin foil target and the reaction products are thermalised and transported in a helium buffer gas jet. This provides a fast, chemically insensitive process (appropriate for a wide range of elements) for reaction product extraction. A (dual) sextupole ion guide (SPIG) guides the ions to

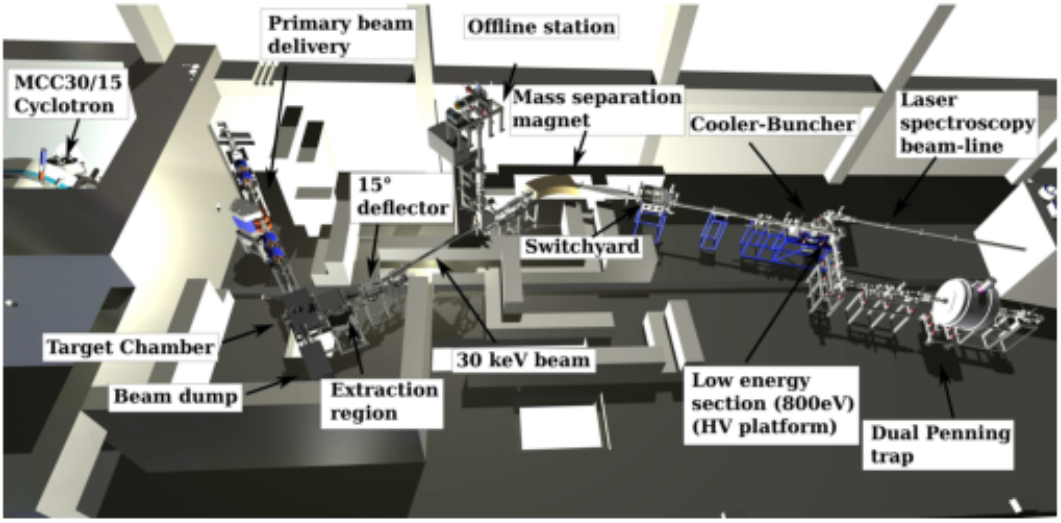

Figure 3.1: The new IGISOL–4 laboratory with the experimental layout. The location of the new MCC30 cyclotron is shown as well as the (re–designed) beam–line, Cooler–Buncher, and the locations of both the collinear laser experiment and the Penning trap experiment.

the extraction region where a compound electrode system focuses the ions as they are accelerated up to an energy of 30 keV. The ion beam is transported to an adjustable dipole magnet for $\frac{q}{m}$ mass separation before entering the switchyard (section 3.1.3) where the beam can be directed to a dedicated spectroscopy line or on towards the Cooler–Buncher (section 3.1.4). After the Cooler–Buncher a hammerhead delivery system consisting of quadrupole deflectors, XY steering electrodes and einzel lenses directs the ion beam to the collinear laser beam–line or the Penning trap beam–line.

3.1.1 K130 and MCC30/15 cyclotrons

The first beams from K130 heavy ion cyclotron at Jyväskylä were successfully produced in 1992 [31]. The cyclotron is equipped with two electron cyclotron–resonance sources (ECRs) and a multicusp light ion source enabling the production of a wide variety of primary beams. The cyclotron can produce ion beams with energies up to 130 q^2/A MeV. The average laboratory use per year is between 6000 and 7500 hours and a third of the beams produced are proton beams, meaning the cyclotron is always in high demand. Reducing the load on the K130 and expanding available beam time was one

of the incentives behind the acquisition of the new MCC30 cyclotron, mainly to expand proton beam production. Originally for the K130 cyclotron the protons were produced within the multi–cusp ion source in the form of positive ions, the source provided singly charged ions from which around 1 mA could be transported to the cyclotron for acceleration. However only 60–70 % of the beam could be extracted leading to beam dumping within the cyclotron. This caused vacuum problems, excessive thermal loading and lead to many internal components becoming highly radioactive, limiting possible beam currents to 10–20 μA. A new method was introduced whereby H^- ions were accelerated and extracted with 100% efficiency, through a thin carbon electron stripper. This allowed proton beam currents of up to 60 μA at 30 MeV and 100 μA at 45 MeV.

The installation of the MCC30/15 light ion cyclotron began in 2009, with the first ion beam production in 2010. The MCC30 cyclotron produces accelerated beams of 18–30 MeV protons and 9–15 MeV deuterons, with intensities up to 200 μA and 62 μA respectively (measured during recent tests). The delivery beam–line is designed such that both the MCC30 and K130 can be operated simultaneously and primary beams from either can be delivered to the IGISOL facility.

3.1.2 Target cave

As shown in figure 3.1 the target chamber is located within a cave, which is constructed from concrete blocks to provide radiation shielding for the rest of the laboratory during experiments. This level of shielding is required for the use of high intensity primary beams as well as a neutron converter currently under development. The primary beam–line delivers beams from the K–130 cyclotron or the MCC30/15 cyclotron to the target chamber where they impinge upon the reaction target, mounted in one of the various ion guides developed at JYFL, with each one designed specifically for different types of reactions. A differential pumping system operates between the relatively poor vacuum of the target chamber ($\sim 10^{-3}$ mbar) and the high vacuum (10^{-5}–10^{-6} mbar) of the ion extraction region and primary beam–line. The differential pumping system consists of 3 oil–free Roots blowers (with an oil–free twin Roots backing pump) pumping the target chamber, and oil diffusion pumps on the primary beam–line and

extraction region. This creates a differential pumping allowing for the primary beam–line and extraction chamber to be at high vacuum, while the bulk of the helium gas is handled by the high throughput Roots blowers. For IGISOL–4 the modification to an oil free operation of the Roots pumps will in future enable the helium used during an on–line run to be recycled through a closed loop purification system located within the radiation shielding.

The increased space, combined with the 15 degree deflector enables collinear (and anti–collinear) laser access points, both from behind the chamber (for in guide ionisation techniques) and from the beam–line direction for laser interactions within the SPIG. A third path exists for perpendicular laser access to the chamber. For more details on the FURIOS laser system see section 3.1.5.

The reaction products are created in high charge states and rapidly thermalise and neutralise as they lose energy and capture electrons in the buffer gas. The majority of elements have a second ionisation potential above the first ionisation potential of helium, thus are expected to reach a 2^+ charge state, however impurities in the gas (such as O_2, N_2, Ne and H_2O) undergo charge transfer reactions, leaving the majority of ions as a singly charged species [32]. Approximately 1% of the reaction products survive as ions and are guided into the SPIG, predominantly in the 1^+ charge state. The impurities in the gas at ppm levels can cause neutralisation of the ionic products, these are frozen out of the helium gas by passing it through a liquid nitrogen cooling trap before entering the target chamber. The levels of oxygen and nitrogen are reduced by factors of 30 and 5 respectively, while H_2O is frozen out completely [32]. The helium buffer gas not only thermalises the reaction products but it also provides efficient cooling for the targets, protecting them from damage due to heating from the primary beam.

A dual SPIG guides the reaction products to the extraction section. A SPIG is employed instead of a (previously used) gas skimmer electrode as it is less sensitive to alignment errors, the extended region allows for improved gas removal, and the strong axial containment provided prevents space charge blowing up the ion plume. The final extraction occurs after the SPIG, away from the high pressure section at the guides exit. This, combined with the small DC potential needed for extraction, minimises the energy and spatial spread of the ion beam. The SPIG also provides greater ion

extraction efficiency (by factors of 1.3 to 5) compared to a skimmer electrode [33, 34]. The sextupole is preferred over a quadrupole structure, as it produces a potential with higher and steeper walls, with a deeper, broader pseudo–potential providing higher ion beam current transport [33]. The extraction region at IGISOL–4 consists of two extraction electrodes, providing a two step extraction/acceleration from the target chamber. The target chamber, part of the primary injection beam–line and the beam dump are held at the platform voltage of +30 kV. The first extraction electrode is held at a potential difference of +10–15 kV, while a second extraction electrode is usually operated between +2 kV and +5 kV creating the two step extraction from the 30 kV platform voltage. This provides more control over the ion beam extraction and focusing to optimise beam transport and delivered intensity. The 30 keV ion beam is transported through the 15 degree deflector and towards the dipole electromagnet for mass separation.

Ion guides

The most extensively used method for production of neutron–rich, radioactive isotopes of the refractory elements is proton (or light ion) induced fission of a natural uranium target. The light ion fission ion guide, as shown in figure 3.2, consists of a water–cooled housing with a natural uranium target mounted at 7 ° to the primary beam to maximise the effective target thickness in the beam direction. The primary beam impinges on the target producing a plasma of high momentum reaction products (emitted nearly isotropically in space), which lose energy as they pass through the separation foil and enter the stopping region. Havar is often used for the separation foil, although if stable reference beams are required then a foil of a specific element can be employed. Ions of the chosen element are knocked from the foil as the reaction products deposit energy, creating a stable reference ion beam. Havar windows are used to separate the ion guide from the target chamber, which the primary beam passes through as it enters and leaves the ion guide. This geometry provides separation of the reaction products from the primary beam, removing the problem of ionisation by the primary beam.

Two other ion guides are also available at IGISOL, the light ion fusion guide and the heavy ion fusion guide (HIGISOL). The light ion guide uses fusion evaporation reactions with light ions (such as p, ^{3}He, α) to produce neutron–deficient isotopes.

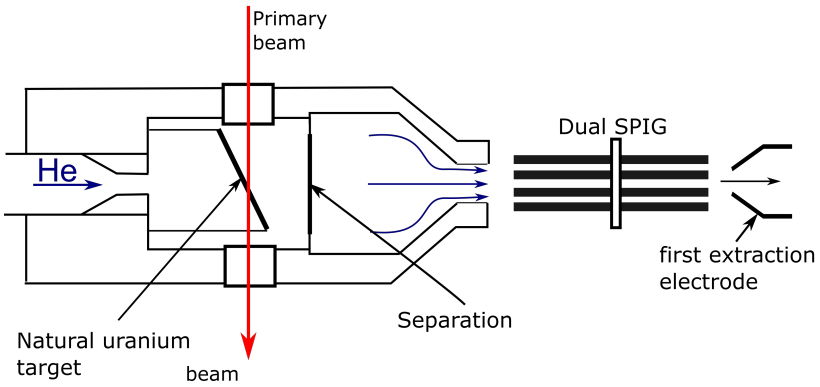

Figure 3.2: A schematic diagram of the fission ion guide and dual SPIG extraction region.

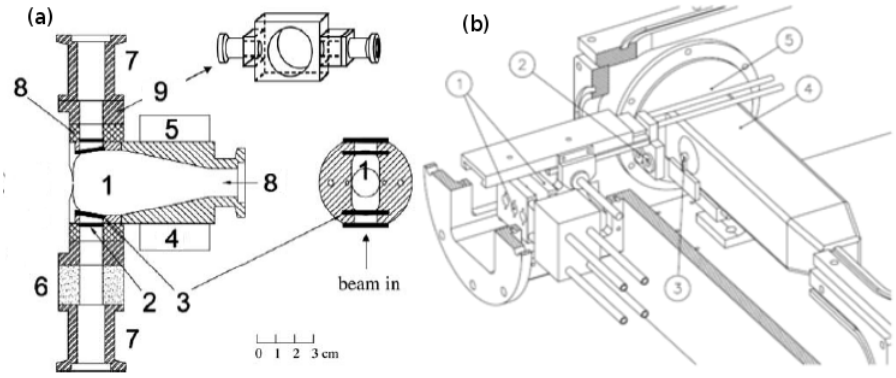

Figure 3.3: The light ion guide (a): (1) stopping volume, (2) beam window, (3) target, (4) heating block , (5) cooling block, (6) graphite collimator (7) beam tube, (8) helium inlet, (9) supporting frame. The heavy ion fusion guide (HIGISOL) (b): (1) Degraders, (2) targets, (3) beam stopper, (4) stopping chamber, (5) skimmer plate. The entrance window is behind the beam stopper. This figure is adapted from [32].

Lower gas pressures and a smaller stopping volume are required compared to the fission ion guide due to the lower energy of the recoiling reaction products. The heavy ion guide is designed for the study of short lived products from heavy ion induced fusion evaporation reactions, typically with production close to the N=Z line.

Neutron converter

A neutron converter is one of the latest planned additions to the IGISOL experimental array, with initial tests held in early 2014. The efficiency of neutron converters is usually $< 10\%$, making a converter impractical with the intensities the K–130 can

provide (due to low neutron beam production). For IGISOL–4 high intensity proton beams are available from the MCC30 cyclotron, enabling the use of a neutron converter to produce fast neutron beams for neutron induced fission reactions. Neutrons allow for a colder (lower energy) fission reaction compared to protons (protons require extra energy to overcome the Coulomb barrier of the target nuclei), such that the products suffer less neutron evaporation. Therefore neutron induced fission (like photon induced fission) has a peak yield further into the neutron–rich side of the nuclear chart, leading to improved yields for neutron–rich isotopes.

3.1.3 Mass separation and the switchyard

The ion trajectory in a magnetic field, unlike within electrostatic elements, depends upon the velocity (and charge) of the ions. Since the ions are accelerated to the same energy a magnetic dipole field allows for $\frac{m}{q}$ selection. The dipole magnetic field is adjusted to select the required mass for transmission into the switchyard. With the reduced energy spread provided by the SPIG the mass resolving power ($\Delta M/M$) of the magnet is around 1100. The gas pressure throughout this section of the beam–line, including the switchyard, is $\sim 10^{-6}$ mbar.

The mass separated beams leave the dipole magnet and enter the switchyard (at the focal plane of the magnet). The switchyard has 3 possible outward beam–lines, with curved electrostatic deflectors employed to guide the ion beam to one of them. The left exit (from the beam direction) can be used for a small monitoring station, the dedicated decay spectroscopy line is on the right and the primary beam–line (straight) to the Cooler–Buncher is the central line. The switchyard contains a movable, narrow slit Faraday cup and actuator mounted micro–channel plates (MCPs) for ion beam monitoring and tuning. A surface–barrier silicon detector is also present for radioactive ion detection and beam tuning.

The dedicated spectroscopy line guides and focuses the ion beam with electrostatic steering elements and a quadrupole lens triplet. Silicon detectors are present for radioactive beam monitoring and rate counting. Positions are available for germanium detectors at the end of the line, where thin windows allow gamma rays to pass through and enter the detector. A decay tape station is located at the end of the spectroscopy

beam–line for isotope implantation. The ions are implanted in the tape, which is periodically cycled around to provide a fresh area for implantation while the implanted ions are moved towards a detector for the observation of decays from isotopes (with half lives in the minutes to hours range).

3.1.4 The Cooler–Buncher and low energy section

The Cooler–Buncher is a gas filled, segmented Radio–Frequency Quadrupole (RFQ) Paul trap, as shown in figure 3.4. On entry the ion beam is decelerated to roughly 100 eV (through 3 decelerating electrodes) and injected into the quadrupole structure. Viscous cooling with the high purity helium buffer gas (of order 0.1 mbar) causes the ions to lose energy while the RF fields constrain the ion motion transversely along the RFQ axis. The motion of an ion within a quadrupole field is governed by the Mathieu parameter q,

$$q = \frac{4QV}{mr_0^2\Omega^2} \tag{3.1}$$

where Q is the charge, V is the RF voltage, Ω is the angular frequency, m is the ion mass and r_0 is one half the distance between opposite rods. For stable ion motion within the RFQ $0 < q < 0.91$ must be satisfied. The depth of the radial potential well is given by

$$D = \frac{qV}{4}. \tag{3.2}$$

The Cooler–Buncher is operated with a AC potential of $\sim$150 V, providing a suitably deep potential for capture of ions upon injection. The voltage, frequency and buffer gas pressure are adjusted to provide optimal cooling and transport for the chosen mass.

A shaped DC electric field gradient guides the ions along the segmented RFQ towards the extraction region. At the extraction region a miniature RFQ extracts the ions out of main structure, providing a region for differential pumping of the helium gas. A miniature RFQ is employed instead of an extraction or skimmer electrode as it produces a smaller final ion energy spread and emittance, but a temporally longer ion bunch [35]. A 50 V trapping electric potential applied to an end plate electrode (located before the miniature RFQ) can be pulsed to bunch the ion beam. The emittance and energy spread of the ion beam is reduced to $<3\pi$ mmrads and <1 eV respectively [36].

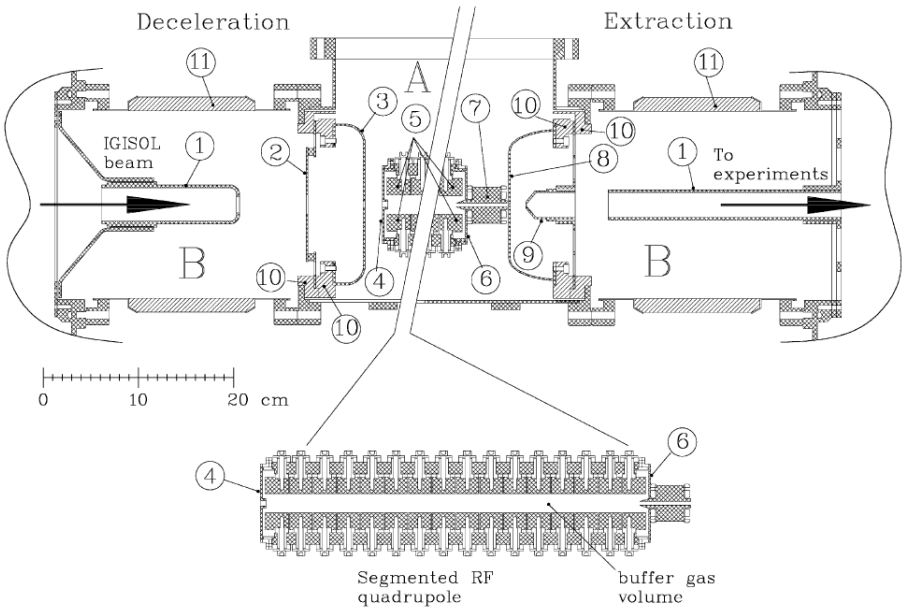

Figure 3.4: Schematic of the Cooler–Buncher, (1) ground electrode, (2) first deceleration electrode, (3) second deceleration electrode, (4) third deceleration electrode, (5) RF quadrupole rod segments, (6) end plate, (7) mini–quadrupole, (8) extraction plate, (9) extraction electrode, (10) insulator ring, (11) HV insulators, (figure adapted from [36]).

The ions are extracted at 800 eV into the low energy section after the Cooler–Buncher, figure 3.5, a fast–switching quadrupole deflector guides the ion beam either towards the collinear laser experimental beam–line or towards the Penning trap beam–line. Optical windows allow access to ion ensembles within the Cooler–Buncher and the low energy section (as marked in figure 3.5). The ions guided towards the laser beam–line are re–accelerated up to the HV platform voltage on exiting the low energy section, shortly after traversing the second quadrupole deflector.

The Cooler–Buncher provides a suitable location for optical manipulation of ions (see section 3.2) with pulsed lasers as the ions are trapped within the Cooler–Buncher for periods up to 1 s. The ions are located in a well defined potential area with a low energy and velocity spread, ensuring good overlap with the laser beam and allowing for the whole ensemble to be on resonance (section 3.2, optical manipulation of ions).

The low energy section also provides a region of well defined potential at a low ion velocity (in comparison to that at 30 keV). Ions of mass 100 take 20 μs to traverse this section, with the ion plume being $\sim$15 μs long. As shown in figure 3.6 the ions

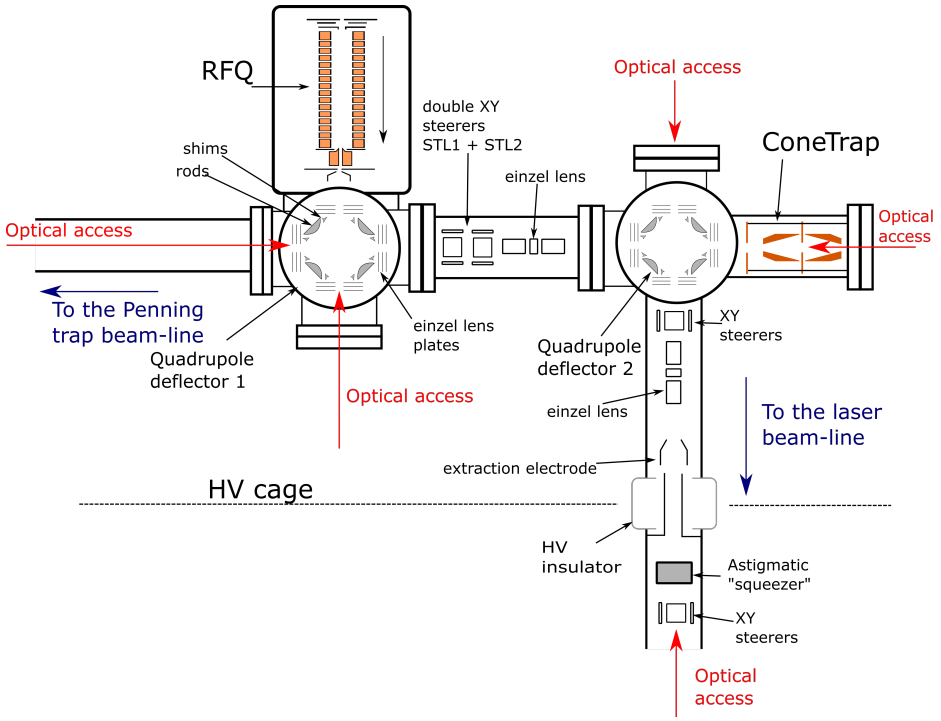

Figure 3.5: The low energy section with ion optics labeled and potential optical access points highlighted.

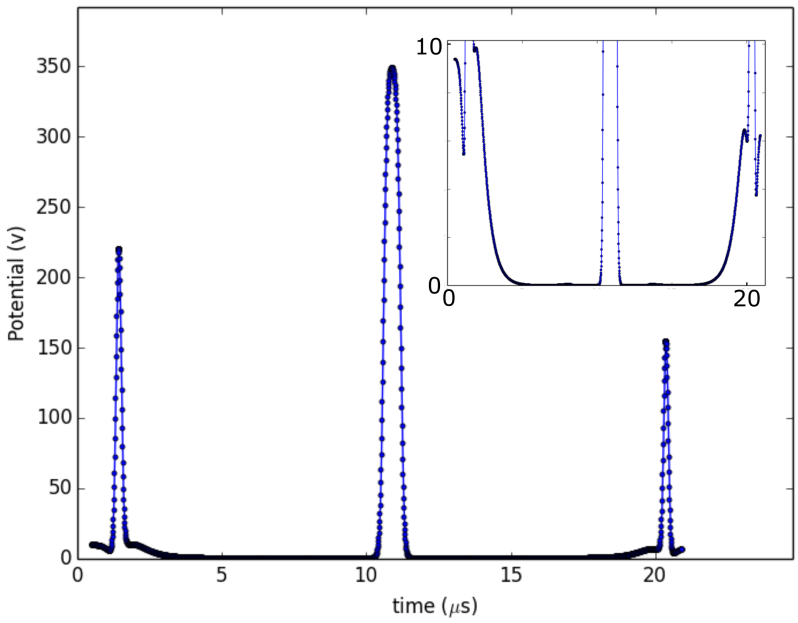

Figure 3.6: A plot of the potential (A=100) ions experience, with respect to time of flight, while traversing the low energy section between the first and second quadrupole deflectors.

spend approximately 15 μs of the 20 μs transit time within 10 volts of the beam–line potential. The time is recorded from the point where the ions leave the quadrupole deflectors, with the potential peaks from left to right representing the einzel lens plate on the first quadrupole, the einzel lens in the beam–line and the einzel lens plate at the second quadrupole deflector. The electrostatic steering elements have been omitted from the figure, however their operating voltages are within 20 V of the beam potential, creating only a small reduction to the effective interaction length. This section also provides a plume matched path for optical manipulation. The Cooler–Buncher release can be matched to the master clock signal of the pulsed laser system (with a suitable delay) to ensure the ion ensemble overlaps temporally with the laser pulse for optimal interaction probability.

3.1.5 Fast Universal Resonant laser IOn Source (FURIOS)

The FURIOS system (as shown in figure 3.7) comprises of a 10 kHz frequency doubled neodymium–doped yttrium aluminium garnet (Nd:YAG) laser, with a maximum output power of 80 W at 532 nm, pumping 3 broadband ($\sim$ 5 GHz [37]) Z–shaped cavity titanium sapphire (Ti:Sa) lasers (532 nm is near the Ti:Sa absorption peak). The Ti:Sa lasers are tunable, with fundamental output wavelengths in the 690–960 nm range. This range can be expanded towards deep UV by utilising higher harmonic generation. Intra–cavity frequency doubling of the Ti:Sa lasers allows for a greater power output in the second harmonic, compared to the power achieved with an external doubling cavity. Further tripling and quadrupling stations provide access to the short wavelength UV regions of the EM spectrum required for many of the transitions within this work. With the higher harmonic generation the final accessible wavelength range spans 205 nm to 900 nm [37], covering a broad range of atomic and ionic transitions.

A grating based Ti:Sa laser and an injection locked Ti:Sa laser are pumped by a second Nd:YAG laser located in the first cabin. The grating Ti:Sa is used for ionisation scheme development (due to the ease of wide range frequency scanning) while the injection locked Ti:Sa was developed in collaboration with the University of Mainz [38]. The key advantage of the injection locked laser is the reduction of the output linewidth to $\sim$20 MHz from the 5 GHz Ti:Sa linewidth. This is achieved

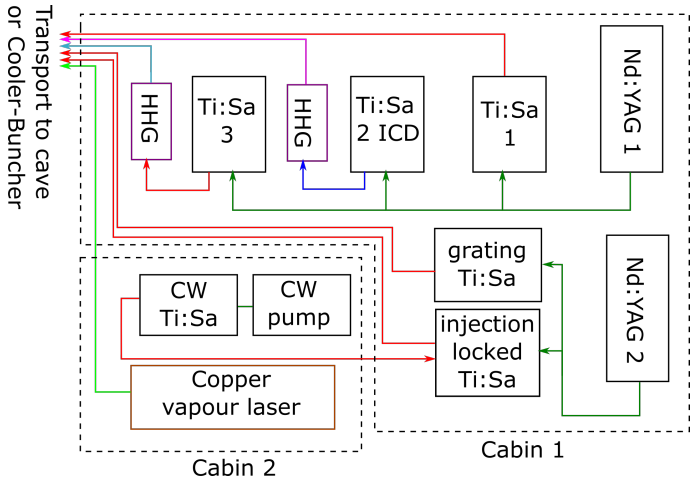

Figure 3.7: A schematic diagram of the laser organization across the two FURIOS cabins.

through injection locking, a technique where the output from a narrow width CW Ti:Sa (master) laser is amplified through a pulsed resonant cavity (the slave injection locked Ti:Sa), where the cavity is tuned to the frequency output of the CW laser. This narrow linewidth laser was employed to study the hyperfine structure in the ground state of ^{229}Th [39]. A pulsed copper vapour laser (CVL) along with a Matisse CW Ti:Sa laser and pump laser are located in the second laser cabin, where the CW Matisse provides narrow bandwidth light for the injection locked Ti:Sa in the first cabin. The CVL is primarily employed for non–resonant final ionisation steps, due to the high output intensity (average output power of 30 W).

The primary aim of the FURIOS system is to provide selective resonant ionisation of neutral products within the ion guide or extraction region, thus producing a pure ion beam of a desired isotope. The laser path length to the target chamber is ∼11 m from the first cabin, with transport via 3 mirror sets reflecting at 90 degrees for the in–jet pathway, and 2 sets for the in–cell pathway. Secondary applications of the FURIOS system include the optical manipulation of ion ensembles, primarily within the Cooler–Buncher or low energy section, but also potential for manipulation of ions in the SPIG. A further application currently under development is the ionisation of the singly charged ion species to a doubly charged state, for the purpose of producing isobarically pure bunches, or removing contaminants, for subsequent spectroscopy. The Cooler–Buncher provides a suitable location, with the long bunching times (and well–defined ion potential) providing maximum interaction chance with the pulsed

laser beams. An ion species of interest can be ionised to a doubly charged state, the change in ion charge leads to a reduction in the ions time of flight through the low energy section and laser beam–line, separating out the doubly charged ions temporally from the rest of the ensemble. Time gating on detection signals or a pulsed deflector would allow for the temporally separated sections of the ensemble to be accessed or removed as required.

3.2 Optical manipulation of atoms and ions

The primary methods of interaction of light with atoms/ions are the three processes of stimulated absorption, stimulated emission and spontaneous emission. When an ensemble of N atoms, each possessing two electronic energy levels E_1 and E_2 (where $E_2 > E_1$), interacts with a external EM field an electron in the lower state, E_1 can be excited by absorbing a photon of energy $\hbar\omega = E_2 - E_1$ (stimulated absorption). Alternatively electrons in the upper state, E_2 can relax to state E_1 (emitting a photon), via spontaneous or stimulated emission. The populations of the two energy states (N_1 and N_2 respectively) are related by the rate equation

$$\frac{dN_1}{dt} = -B_{12}\rho N_1 + B_{21}\rho N_2 + A_{21}N_2, \tag{3.3}$$

where B_{12} and B_{21} are the Einstein B coefficients for stimulated absorption and emission, ρ represents the energy density of the EM field and A_{21} is the Einstein coefficient for spontaneous emission. For a steady state situation the population of N_2 tends towards $(N_1 + N_2)/2$, stimulated absorption and emission compete, limiting the maximum population in E_2, this is why a simple two level system cannot achieve the population inversion required for lasing (in the weak field limit).

From the semi–classical consideration of the transitions the electric potential of a laser can be treated as a time varying perturbation on the Hamiltonian of the atomic system. Taking an E field of the form $\mathbf{E} = E_0 \cos\omega t$ and the resulting wave function ϕ as a superposition of the two unperturbed wave functions

$$\phi = C_1(t)e^{-i\omega_1 t}\phi_1(\mathbf{r}) + C_2(t)e^{-i\omega_2 t}\phi_2(\mathbf{r}), \tag{3.4}$$

with the coupling factors C_1 and C_2 satisfying $|C_1|^2 + |C_2|^2 = 1$. This leads to a pair

of coupled differential equations

$$\frac{dC_1}{dt} = -i\Omega \cos\omega t e^{-i\omega_0 t} C_2$$
$$\frac{dC_2}{dt} = -i\Omega \cos\omega t e^{i\omega_0 t} C_1,$$

where Ω is the Rabi frequency, defined as

$$\Omega = \frac{E_0}{\hbar}\langle\phi_1|e\mathbf{r}|\phi_2\rangle. \tag{3.5}$$

This term characterises the size of the interaction through the amplitude of the radiation and the strength of the atomic response. Solutions to the equations are considered in two limiting conditions, firstly the weak field limit where the transition probability is small (the light source has a low spectral intensity). If the system is initially in state one then $C_2(t) << C_1(t)$ and $c_1(t) \simeq 1$ for all t. Therefore it follows that

$$C_2 = -\frac{1}{2}\Omega\left(\frac{1 - e^{-i(\omega-\omega_0)t}}{\omega - \omega_0}\right). \tag{3.6}$$

The transition probability is given by

$$|C_2(t)|^2 = \left(\frac{\Omega}{2}\right)^2 \left(\frac{\sin\frac{1}{2}(\omega-\omega_0)t}{\frac{1}{2}(\omega-\omega_0)}\right)^2, \tag{3.7}$$

this can be related the Einstein B coefficients through the volume energy density $\rho(\omega)d\omega = \frac{1}{2}\epsilon_0 E_0^2$ then assuming the response of the interaction is narrow compared to the bandwidth of the radiation leads to

$$\frac{|C_2(t)|^2}{t} = \frac{\pi}{3\epsilon_0\hbar^2}|<\phi_1|e\mathbf{r}|\phi_2>|^2\rho(\omega_0) = B_{12}\rho(\omega_0). \tag{3.8}$$

In the strong–field limit, such as excitation by monochromatic radiation of angular frequency ω, the rate equations become

$$\frac{dC_1}{dt} = -\frac{1}{2}i\Omega e^{i\delta t} C_2$$
$$\frac{dC_2}{dt} = -\frac{1}{2}\Omega e^{-i\delta t} C_1,$$

where $\delta = \omega - \omega_0$ is the detuning of the radiation from the atomic transition. For the case of resonant excitation ($\omega = \omega_0$) the solution for the upper state is

$$\frac{d^2C_2}{dt^2} = -\frac{1}{2}\Omega^2 C_2. \tag{3.9}$$

Assuming that initially $C_2(0) = 0$, the state probabilities are given by,

$$|C_1(t)|^2 = \cos^2 \frac{1}{2}\Omega t,$$
$$|C_2(t)|^2 = \sin^2 \frac{1}{2}\Omega t,$$

and the system oscillates from state 1 to state 2 with a period of $\frac{2\pi}{\Omega}$. This is known as Rabi oscillation and its a coherent effect that deviates from the steady state picture obtained from the rate equations, where the population in the upper state is steady and has a maximum value of $\frac{N}{2}$. For off–resonant excitation the solutions are non trivial where the probability of population in state 2 is given by

$$|C_2(t)|^2 = \frac{\Omega^2}{\Omega + \delta^2} \sin^2 \left(\frac{t}{2} \sqrt{\Omega^2 + \delta^2} \right), \tag{3.10}$$

the system is never found in state 2 with unity probability, unlike the resonant case, and the population oscillates rapidly at $\sqrt{\Omega^2 + \delta^2}$.

3.2.1 Optical pumping

The optical manipulation of atoms and ions has been an important tool in a broad range of research areas for many years. Optical pumping was first shown by Brossel, Bitter and Kastler in 1952 [40], where they demonstrated the effect in mercury vapour and measured the lifetime of the $^3P_1$ state from the resonance linewidths. Optical pumping provides a method for producing significant changes in the electron energy level population distributions of atoms or ions, which in turn can affect the ion motion, mobility and spatial decay distribution. The atomic electrons are selectively stimulated by a monochromatic beam of light, with a frequency and polarisation matching that of an atomic transition, from a lower lying energy state to a higher lying state, (after which they can relax down into lower lying states via photon emission (EM radiation) or non radiative processes). The EM radiative decay processes within an atom follow specific selection rules for different transitions, which are the electric and magnetic multipoles of the EM field. If we assume the spatial distribution of the electrons ($\sim 10^{-9}$ m) in the atom is small compared to the wavelength of light ($\sim 300 \times 10^{-9}$ m) any resulting phase difference due to spatial origin can be neglected. This approximation (the dipole approximation) leads to the electric dipole transition probability for a 1

electron atom given as

$$A_{E1} = \frac{\omega_{ik}^3}{3\pi\epsilon_0\hbar c^3}\frac{1}{g_k}\Sigma_{m_k m_i}| < Km_k|e\mathbf{r}|Im_i > |^2, \tag{3.11}$$

where ω_{ik} is the angular frequency of the light, g_k is a weighting factor, K and I represent the angular momenta of final and initial states respectively and $e\mathbf{r}$ is the electric dipole operator. The selection rules are given as for E1 transitions $\Delta J = 0, \pm 1$ ($0 \rightarrow 0$ forbidden), $\Delta M = 0, \pm 1$, and parity must change between the initial and final states.

Optical pumping was first employed in conjunction with collinear laser spectroscopy at IGISOL–3 by Cheal et al. in 2005 with an off–line demonstration on yttrium and a full on–line campaign studying niobium in 2009 [41]. Both experiments employed broadband, pulsed titanium sapphire lasers from the FURIOS cabin (see section 3.1.5). The pumping transition can be selected to enhance population within a specific state allowing for improved efficiency or just access to spectroscopy from the state. As electrons are pumped into an intermediate higher state the initial equilibrium of states is disturbed. The electrons can relax into any available lower states. If the lifetime of one of these states is sufficiently long the distribution can be greatly altered, with the full depletion of the ground state possible. The excited electrons relax following allowed transition routes. In cases where an electric dipole transition is forbidden by parity considerations only the magnetic dipole or electric quadrupole transitions can occur, these are much slower processes leading to long lived populated states, the so called metastable states. Collisional processes can also cause the state to de–populate via a non–radiative process, which can greatly affect metastable populations when the ion/atom density is sufficient for many collisions to occur. For optical pumping cases strong transitions are preferable, with high $A_{(E1)}$ coefficients (or high oscillator strength values, f) and a high electron population in the initial state. If the J values are kept low it reduces the number of peaks and increases the intensity in each hyperfine component. Applications of this technique include increasing population in a metastable state for optical spectroscopy purposes, where no accessible transitions from the ground state are available. Another potential application for spectroscopy involves populating a metastable state with a larger charge exchange cross–section than the ground state, this allows for resonance to be detected by loss of ions.

An initial goal of employing the technique was to enable spectroscopy on molybdenum as transitions from the ground state were in the deep UV region. However a metastable state was observed to be sufficiently populated, independent of production method, which allowed for spectroscopy from this $4d^4\ 5s\ {}^6D_{1/2}$ state (which is also exploited in this work).

3.3 Collinear laser spectroscopy

Collinear laser spectroscopy has been employed since the 1970s for the study of the hyperfine structure in atoms and ions and is still a key experimental tool for studies at many radioactive beam facilities [42]. The concept of employing a collinear geometry was first proposed by Kaufman [43], it relies on the forward velocity compression experienced by an ensemble upon acceleration. On electrostatic acceleration the energy spread of an ionic ensemble remains unchanged but the velocity spread is greatly reduced. The reduction of the initial velocity spread ν_0 under acceleration is given by

$$\delta\nu \approx \frac{1}{2}\left(\frac{E_0}{eV}\right)^{\frac{1}{2}} \delta\nu_0, \tag{3.12}$$

where E_0 is the energy spread and V is the accelerating potential. This reduction in velocity spread upon acceleration can clearly be seen in figure 3.8.

The velocity compression under electrostatic acceleration is exploited experimentally to reduce the Doppler broadening of resonantly scattered fluorescent photons from an accelerated ion beam. Acceleration of the ions up to tens of keV causes a reduction of the Doppler broadening to less than the natural linewidth for the majority of atomic/ionic transitions. A narrow linewidth, coherent light source, of fixed frequency near a chosen atomic or ion transition, is used to probe the transition in collinear (or anticollinear) geometry with respect to the ion beam path. An acceleration potential is applied to the ion ensemble, changing its velocity and causing a Doppler shift in frequency of the light source with respect to the ion rest frame. The provides a simple and readily reproducible approach for scanning through frequency space. At a particular acceleration voltage the ion ensemble perceives the shifted light source at the transition frequency, and photons are resonantly scattered and detected. The Doppler broadening reduction allows for the hyperfine structure to be resolved,

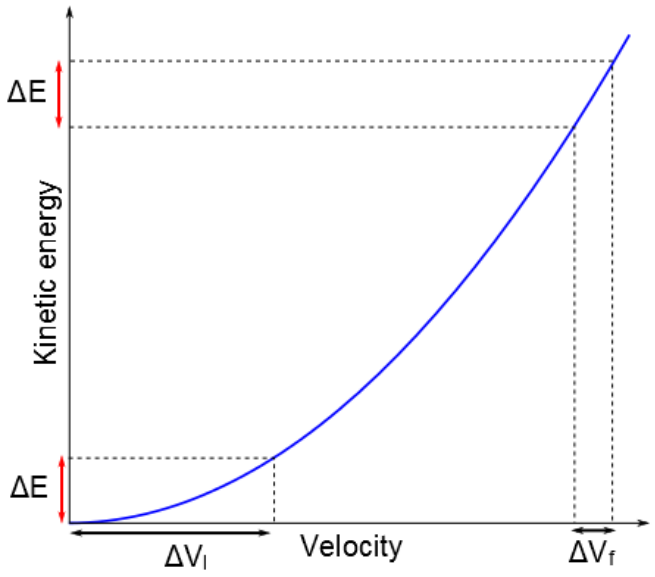

Figure 3.8: A plot displaying the (non–relativistic) kinetic energy as a function of velocity, the dashed lines show the corresponding velocity spread for the same kinetic energy spread in two different velocity regions.

with the lineshape width dominated by the natural linewidth of the transition and the linewidth of the light source.

At IGISOL–4 this technique is employed, with the experimental setup shown in figure 3.9. A frequency doubled, narrow linewidth dye laser (section 3.3.1) provides the light source in a anti–collinear geometry, with the laser beam and an ion beam positioned and shaped to provide optimum overlap within the light collection region (LCR). An accelerating potential is applied to the LCR, to further accelerate the 30 keV beam from the Cooler–Buncher, and altering this potential provides a means of Doppler tuning the ions. A series of quartz lenses image the resonantly scattered photons onto a segmented photomultiplier tube (PMT), which are recorded by a data acquisition system (section 3.4). Only two of the 8 segments are used as this covers the spatial spread of the resonant photon emission from the ion ensemble and limits the laser scatter background detected. The ion beam from the Cooler–Buncher can be continuous or bunched. Operating in the bunched mode the ions are held within the RFQ structure, by a fixed +50V potential applied to an end plate electrode, for 10–1000 ms. The end plate potential is subsequently dropped for 100 μs, to allow sufficient time for the ions to exit the Cooler–Buncher as well as preventing any potential kicks to the back of the ensemble. The continuous/bunched beams are guided through the low

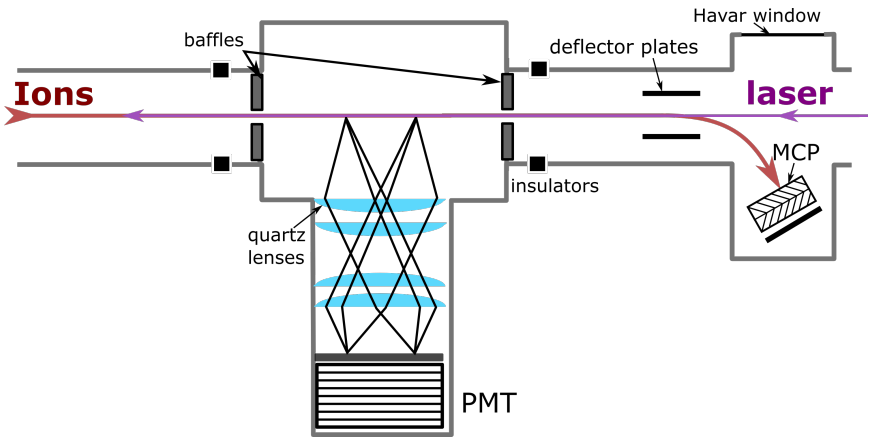

Figure 3.9: The light collection region of the collinear laser beam–line. Resonantly scattered photons are imaged by a series of lenses onto a segmented PMT and detected. The post LCR micro–channel plates (MCPs) and Havar window are also shown.

energy section before re–acceleration to 30 keV. The ion transit time to the LCR (from the Cooler–Buncher) is mass dependent, usually between 60–100 μs, so ion bunches will arrive at the LCR within a specific time window from their release. A time gate applied to the photon signals that coincides with the presence of the ion ensemble within the LCR ensures maximum resonant photon detection while minimising the fraction of random beam light and photon scatter detected. Only the background contribution within the 15 μs window is recorded, reducing the background rate by a factor of 10^4 compared to continuous ion beam operation, making the bunched operating mode greatly preferred for laser spectroscopy. Figure 3.10 shows the relationship between the Cooler–Buncher release signal (controlled by the data acquisition system) and the subsequent ion flight time and photon signal gating. The adjustable Cooler–Buncher containment time allows for variable ion bunch sizes, and access to longer interaction times for optical manipulation within the Cooler–Buncher.

3.3.1 The dye laser

A frequency stabilised Spectra Physics CW (continuous wave) 380D ring dye laser, pumped by a Coherent 532 nm Verdi solid state laser (maximum power output of 5 W), is used for the collinear laser spectroscopy at the IGISOL facility. Both lasers are located within a purpose built cabin, at the end of the collinear laser beam–line. Dye lasers generally have a wide tuning range, (depending on the dye used for the

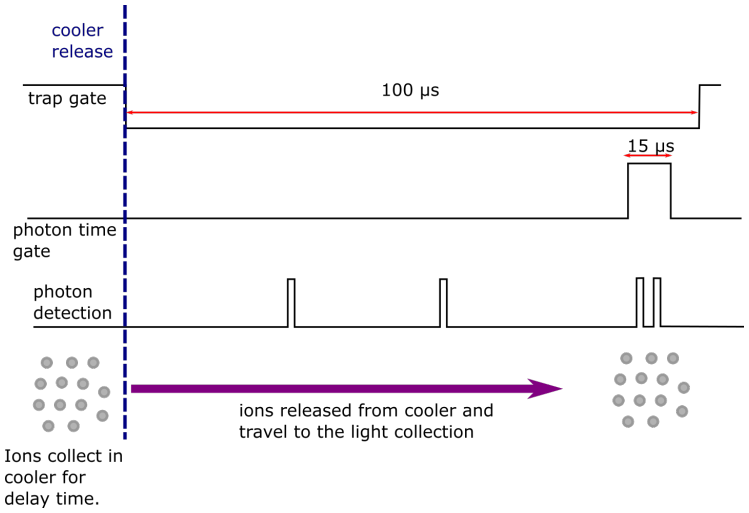

Figure 3.10: The relative timings of the photon time gating and ion release signals for the Cooler–Buncher, the ions are collected and stored for the delay period before the end–plate potential is dropped for 100 μs and the ions are released.

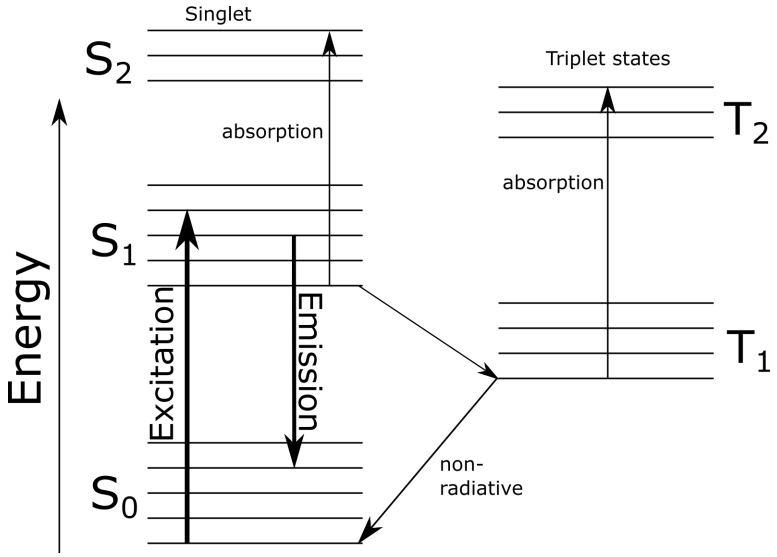

Figure 3.11: A diagram of the various energy levels associated with a lasing dye.

lasing medium), which makes them advantageous for use in laser spectroscopy. The organic dyes, once in solution, possess a large number of rotational and vibrational (rovibrational) excited atomic states, creating broad, continuous energy bands that account for the continuous absorption and emission spectra. As show in figure 3.11 a population inversion is achieved by pumping (using the fixed frequency solid state laser) the population from the ground S0 band into the low–lying S1 singlet band, where they relax into the lowest level of the S1 band by non–radiative processes. Depopulation of the lowest S1 state occurs via photon emission, repopulating the excited S0 states, with the emission photons at a longer wavelength (lower energy) than the absorbed photons (due to non radiative relaxation through the S1 states and photon emission to higher lying S0 states). The most frequently used dye at IGISOL is Rhodamine 6G, an organic dye, which is used in solution with ethandiol, providing a laser tuning range of 570–620 nm in the fundamental output. The dye solution has to be constantly circulated through the system to prevent cavity losses caused by population build up in the triplet states and limit heating degradation of the dye by the pump laser. This circulation is achieved through a closed loop pump system, creating a laminar dye jet within the laser cavity (at Brewsters angle to the pump laser). As shown in figure 3.12 the pump laser beam is reflected from the pump mirror through the dye jet, and the bow–shaped cavity is formed from mirrors M1–M4. the pump laser is usually operated between 3 W and 4 W of output power.

Only wavelengths that satisfy $\lambda = L/n$, where L is the cavity round trip length and n is an integer number, can propagate within the cavity, leading to a frequency separation of modes of around 200 MHz. A Uni–Directional Device (UDD) within the cavity prevents the cavity lasing in both directions, which leads to mode hopping and instability in the frequency output. The UDD consists of a Faraday rotator coupled to an optically active quartz compensator, both of which rotate the polarisation of the light by a few degrees. The rotation of the Faraday rotator is direction independent but the rotation of the compensator is not, as such light traveling in one direction will incur no net polarisation change. Light traveling in the opposite direction will suffer a polarisation rotation (in the same direction) from both components (about 7 degrees), leading to further rotation with many passes through the UDD. This light is lost during propagation through the cavity as many of the laser optical components

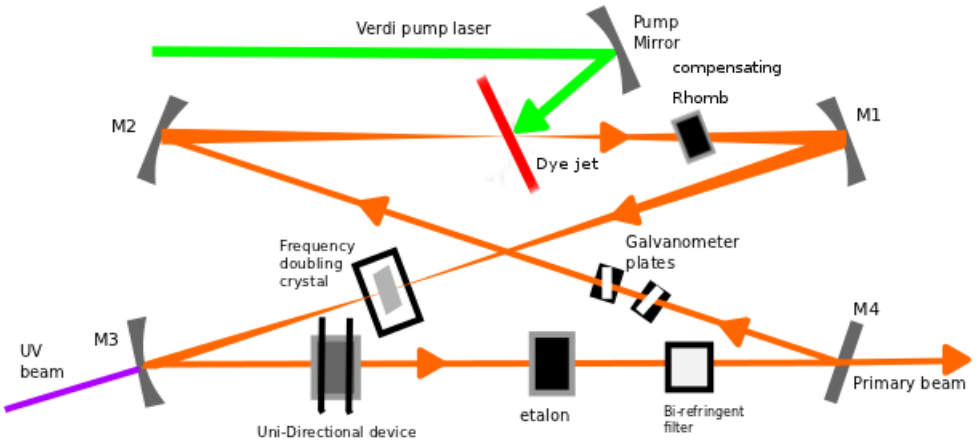

Figure 3.12: A schematic of the Spectra Physics 380D ring dye laser, showing the 4 mirrors that create the bow–tie cavity, the pump laser, dye jet and the optical components that help stabilise and select the required single mode output.

sit at Brewster's angle. The UDD is essential for single mode operation of the Spectra Physics 380 dye laser. The laser output mode is selected using a combination of a birefringent (Lyot) filter, a 'thick' etalon and a 'thin' etalon. The birefringent filter consists of three birefringent plates, which can alter the polarisation of light (from linear to elliptical) that passes through them depending on wavelength and angle of the plates. The plates can be rotated to change the frequency point at which the polarization is rotated by 180 degrees (or multiples thereof), selecting the required modes while inhibiting others as the polarisation shift differing from multiples of 180 degrees leads to photon loss at Brewster surfaces. The thick and thin etalons are used in conjunction with the filter to select a single cavity mode (as shown in figure 3.13). The thick etalon consists of two mirrors with a reflectivity of 30% and a piezoelectric element. Applying a voltage to the piezoelectric element provides a shift in the path length between the two mirrors, used for tracking of the laser mode. The thin etalon contains a piece of glass with a broad light transmission profile, which, when used in conjunction with the thick etalon, suppresses neighbouring transmission maxima to prevent mode hops. Small angles between components and a compensating rhomb help to reduce the effect of astigmatism of the laser light. Astigmatism occurs when light incident on a curved mirror surface creates a reflection with an ellipsoidal profile,

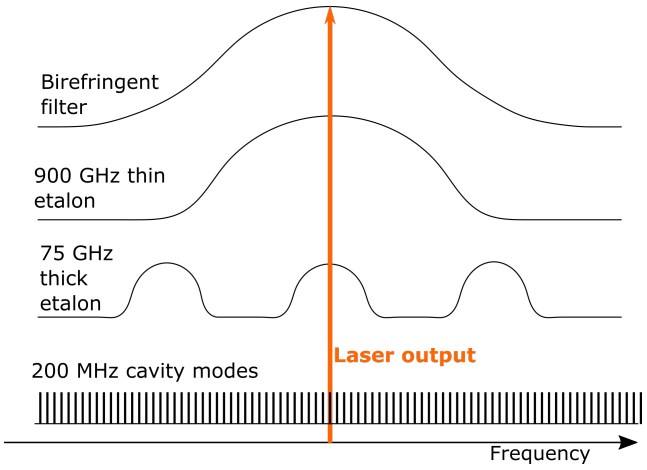

Figure 3.13: A representation of the birefringent filter and etalon transmission peaks, showing how they are combined to give single cavity mode selection for the laser output. The transmission profiles and laser mode spacings are not to scale.

where the light on the major and minor axes have different focal points. The cavity has two laser beam waists, one located at the dye jet and a second waist where a frequency doubling crystal is placed.

Frequency stabilisation

Any vibrations or thermal fluctuations can alter the laser cavity length, leading to changes in the output frequency or potentially mode jumps. These changes increase the linewidth of the laser light, and reduce the resolution and efficiency of spectroscopy. Therefore the dye laser is actively stabilised by locking the fundamental frequency to an absorption peak in molecular iodine in this work. The commercial Spectra Physics Stabilok^{TM} is used for frequency stabilisation. The Stabilok consists of two etalons, a high finesse reference etalon (500 MHz FSR) and a low finesse slave etalon (8 GHz FSR). The laser frequency is locked to the side of the high finesse etalon, with a free spectral range greater than the mode separation. The slave etalon takes care of large frequency changes such as mode hops. The absorption spectra of molecular iodine is used as an absolute frequency reference to account for any long term thermal drift within the two etalons. The frequency is locked to the minimum of an iodine absorption peak by a $\sim$ 3 MHz phase locked modulator. 'Error signals' are converted into voltage signals and used to drive the cavity back to the correct frequency. The feedback servo loop adjusts the piezo–controlled M2 for small frequency shifts or the

galvanometer plates (and tracked etalon) if a large frequency excursion is encountered.

Frequency doubling

The low–lying 'atomic' transitions in ions generally lie within the UV (ultraviolet) section of the EM spectrum. The fundamental output of the dye laser lies within the visible to infra–red spectrum. A non–linear, frequency doubling crystal is employed to generate the second harmonic of the laser light. The crystal used is β–barium–borate (β–BBO), which is placed into the cavity between the M2 and M3 mirrors, where the secondary waist of the laser beam is located. This placement at the beam waist maximises the power density entering the crystal, increasing the power of the UV output. The UV laser light is coupled out of the cavity through mirror M3, after which it is transported and focused into the LCR. The frequency doubling crystal (β–BBO) is a non–linear optical medium, which enables the wavelength range of the (dye) laser to be extended into the UV region. This UV generation occurs within the negative uniaxial, birefringent crystal due to the laser electric field inducing a non–linear polarisation wave through the atomic electric fields. This polarisation wave may be expressed as

$$\vec{P} = \epsilon_0(\chi_1\vec{E}_1 + \chi_2\vec{E}_2^2 + \chi_3\vec{E}_3^3 \ldots), \tag{3.13}$$

where $\vec{P}$ is the polarisation and χ_n are the electric susceptibility tensors. If the applied field is sinusoidal ($E = E_0\sin(\omega t)$), a second harmonic will be generated ($E = E_0\cos(2\omega t)$) via the χ_2 response as

$$\vec{P} = \epsilon_0\chi_1\vec{E}_0\sin\omega t + \frac{\epsilon_0\chi_2}{2}\vec{E}_0^2(1-\cos 2\omega t) + \ldots. \tag{3.14}$$

As light with a high power density passes through the medium (note the E_0^2 dependence of the second term) the second harmonic of the light field can be generated. The refractive index of the birefringent crystal for the fundamental frequency and second harmonic frequency can be matched ($n_\omega = n_{2\omega}$) by adjusting the tilt angle of the crystal optical axis with respect to the incident laser beam. In matching the refractive indices the phases of the two components are made equal and $\Delta k = k_{2\omega} - 2k_\omega = 0$, resulting in maximum generation efficiency (the second harmonic is generated constructively throughout the crystal).

3.3.2 Atomic spectral lineshapes

All atomic absorption lines have an associated intrinsic natural linewidth due to the finite excited state lifetimes. The natural linewidth follows the uncertainty principle, leading to a mean lifetime of the state, $\tau = \hbar/\Gamma$, where Γ is the FWHM of the lineshape profile. The resultant lineshape is given by

$$I(\omega) \propto \frac{1}{(\omega - \omega_0)^2 + \frac{\Gamma^2}{4}}, \tag{3.15}$$

where ω_0 is the resonance centroid. This is the Breit–Wigner formula, producing a Lorentzian spectral lineshape for the natural width of the line. Most absorption lines have linewidths in the 20–50 MHz range.

Several broadening processes can further increase the linewidth (and alter the shape) of the emission profile, which are separated into homogeneous and inhomogeneous broadening. Homogeneous broadening affects all absorbing species equally, leading to a range of frequencies each atom can absorb (such as collisional broadening). Inhomogeneous broadening is when individual atoms possess differing absorption frequencies, the most common type being Doppler broadening. Doppler broadening occurs due to the finite thermal energy distribution of an ensemble creating a spread in the velocities of the atoms. In the atom/ions reference frame the light angular frequency, ω_0, appears to be shifted by $\omega_0(1 \pm \frac{v}{c})$,where the atom/ion has a velocity component $v$in the propagation direction of the light. From the Maxwell–Boltzmann distribution the fraction of atoms with velocity between v and $v + dv$ is given by

$$\frac{df(v)}{dv} = \sqrt{\frac{m_A}{2\pi kT}} e^{-\frac{m_A v^2}{2kT}}, \tag{3.16}$$

where m_A is the mass of the atom, k is the Boltzmann constant and T is the temperature. Using the Doppler shift $dv = \pm\frac{c}{\omega_0} d\omega$ the radiation probability function $S(\omega)$ is given by

$$S(\omega) = \sqrt{\frac{m_A c^2}{2\pi\omega_0^2 kT}} e^{-\frac{m_A c^2(\omega-\omega_0)^2}{2kT\omega_0^2}}, \tag{3.17}$$

with a full width at half maximum of

$$\mathrm{FWHM} = \omega_0 \left(\frac{8\mathrm{kTln2}}{\mathrm{m_A c^2}}\right)^{\frac{1}{2}}. \tag{3.18}$$

The width of the Gaussian Doppler profile depends on the transition frequency, temperature (energy spread) and the mass of the atom/species involved.

Pressure (or collisional) broadening occurs when the emitting or absorbing atom experiences collisions with other atoms, causing a perturbation in the energy levels. Collisions interrupt the oscillator, limiting the time period over which a coherent wave train is emitted, these interruptions cause a broadening in the frequency line profile. The broadening width is inversely proportional to the rate of collision, so keeping the pressure and ion density low greatly reduces this contribution to the final line shape.

Power broadening produces a Lorentzian contribution to the final profile, given in equation 3.19. Power broadening occurs due to the light intensity, as it exceeds the saturation intensity for the chosen transition the atoms/ions spend a greater amount of time in the excited state. The increase in laser intensity, I, increases the rate of stimulated emission (effectively reducing the lifetime of the upper state), increasing the observed width of the transition. For CW laser interactions this is dependent of the steady state population of the excited state $\langle P_2 \rangle$ as

$$\langle P_2 \rangle = \frac{1}{2} \frac{(I/I_{sat})}{1 + ((\omega - \omega_0)/\beta)^2 + (I/I_{sat})}, \tag{3.19}$$

where I_{sat} is the saturation intensity for the transition and β is a width parameter (a combination of spontaneous emission and relaxation processes). The broadening differs for pulsed laser systems, particularly when the pulse length is less than the relaxation times at which point coherence becomes important and the rate equation description becomes invalid.

The final line shape is result of the combination of all the line broadening contributions, resulting in a convolution of the Lorentzian and Gaussian functions, known as a Voigt profile.

3.4 A new data acquisition system

The current laser spectroscopy data acquisition system consists of a VME crate mounted controller, a dedicated serial terminal and a Sunblade desktop computer. The desktop communicates with the VME crate via the serial terminal, transferring run parameters and initiating or ceasing the scan. During an experimental acquisition scan the LCR voltage is set, the ion ensemble is released from the Cooler–Buncher (after the chosen containment time has elapsed) and photons detected by the PMTs are recorded by

the acquisition system. The LCR potential is altered by the chosen step size, before the next Cooler–Buncher release. This is repeated for the channel range chosen, after which the LCR potential is re–set to the initial value and the next data acquisition scan commences. The time gates applied to the photon signals and the Cooler–Buncher release timings (figure 3.10) are implemented through hardware gate and delay NIM modules, located within the laser cabin. The delay from the Cooler–Buncher release and the width of the photon acceptance gate are adjusted manually for each experiment, with the time–of–flight width depending on the mass (to charge ratio) of the ions. The system is controlled through the user interface of the spectroscopy software, with up to four separate data input channels (referred to as scalar 1 to 4). These recorded the total photons counted per channel, the photons counted within the time gate and the other two channels are available for uses such as two photon burst spectroscopy. The age of the system makes any replacements or alterations to the software and hardware challenging.

3.4.1 Experimental incentives for a new system

For bunched laser spectroscopy a temporally narrow ion bunch is preferred, as a reduced time gate applied to the photon signals reduces the fraction of background contributions from laser scatter or beam light. However time focusing of the ion bunch during the Cooler–Buncher release was observed to create a uniformly varying energy distribution across the ion bunch. The finite time for the potential drop on the end plate causes ions with a higher energy to exit first, the ions at the (temporal) front of the ion bunch are more energetic than the ions at the back. This increase in the energy spread of the ion bunch leads to a greater velocity spread and a broadening of the observed resonance lineshapes. This effect can be seen in figure 3.14, shown by the sloping ellipsoidal structure in the 2D plot of Doppler tuning voltage and photon detection time. Different sections of the bunch are on resonance at different accelerating voltages, causing a ‘broadening’ to the recorded photon peaks. This effect can be corrected for if the photon time of arrival is known, the correlation between photon arrival time and Doppler tuning voltage can be used to remove the artificial broadening from the spectrum. This is the main experimental incentive for a new DAQ system, one that records photon timing data during the run. With the capability to correct

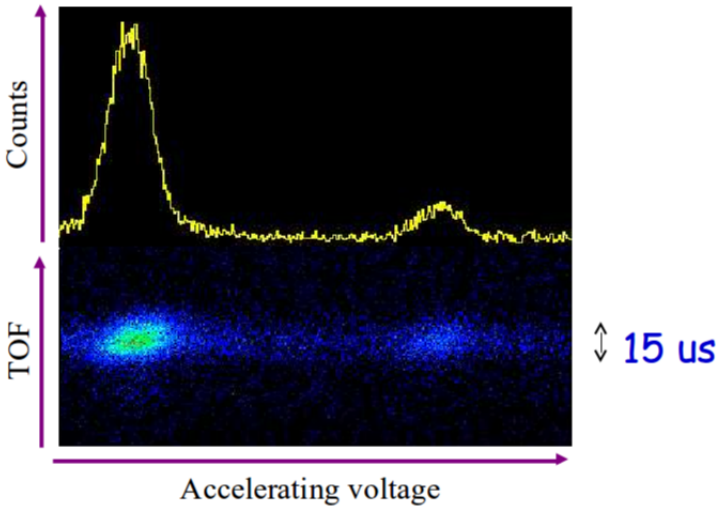

Figure 3.14: A plot of the photon counts across two resonance peaks with the corresponding time of flight plot below. A structure is present in the time–of–flight plot within the 15 μs bunch, a correlation between the time of flight and the accelerating voltage.

for this effect the back of the ion bunch can be intentionally 'kicked' upon release, increasing the velocity spread but compressing the temporal length of the bunch. This would provide a reduction in background contributions through a narrower temporal gate on the photon signals. With multiple ions per bunch it becomes possible to observe multiple resonant photons per bunch, identifiable as the photons arrive within 15 μs of each other. A suitably large ion bunch can be formed by increasing the ion count rate or increasing the ion bunching time (>10 ions per second and >100 ms). A system that can identify multiple photons per bunch (photon bursts) can be used to vastly improve the signal to background ratio of a scan.

3.4.2 The new DAQ system

A new, compact DAQ system based around the Arduino^{TM} microcontroller has been developed in this work. (shown in figure 3.15). The system allows for 'time stamping' of photons within an ion bunch, photon burst spectroscopy and provides full software control over the time gating window (post data acquisition). Also a new data acquisition software, specifically designed for the system, has been written using the Python scripting language. The modest 16 MHz central processing unit (CPU) can provide ~250 ns resolution for the photon time stamping, more than sufficient for the arrival

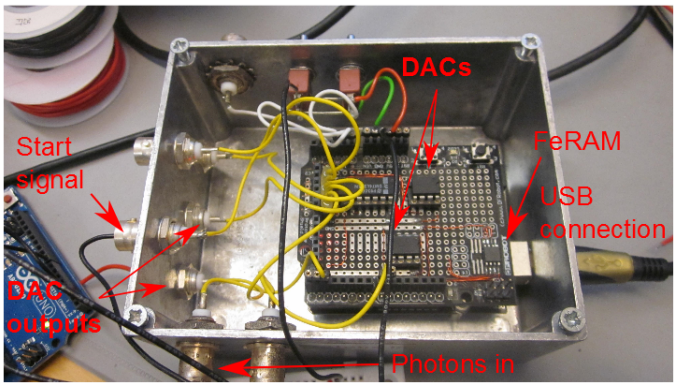

Figure 3.15: Photograph of the microcontroller based data acquisition system.

time corrections shown in figure 3.14. All photon data within a 100 μs window from the PMT is collected by the system in a single input, with all time gating and photon burst counting happening as a post process implemented by the control software on the PC.

In a standard counting mode the system records photons counted during the dwell time between Cooler–Buncher releases (triggered by an interrupt service routine) without recording time stamping information. A second operating mode sends a release signal to the Cooler–Buncher, waits a preset amount of time (~50 μs), and then digitizes the amplified (and shaped) positive TTL signal from the PMT over 100 μs. The position of the photon signal recorded (with a resolution of 250 ns) within this 100 μs provides the 'time stamping' of the photon events. After this the system alters the DAC output by a pre–set step size, changing the Doppler tuning voltage supplied by the Cooknell power supply. Altering the voltage at the end of each release cycle provides ample time for the DAC (and Doppler tuning voltage) to settle. This process is displayed in figure 3.16.

The system provides portability and flexibility, allowing for use at any facility with minimal installation time. Full software control over the time gating online is available, combined with time stamping of the photon arrival removes the requirement of calculating and setting the gates manually before the scan begins. All recorded data is stored on a ferromagnetic RAM (FRAM) chip and written to file (through the USB connection) on an event–by–event basis. Each entry contains the channel (related to the DAC output) of the photon observation, the time stamp, and the number of photons observed in that channel (for easy photon burst identification). This provides

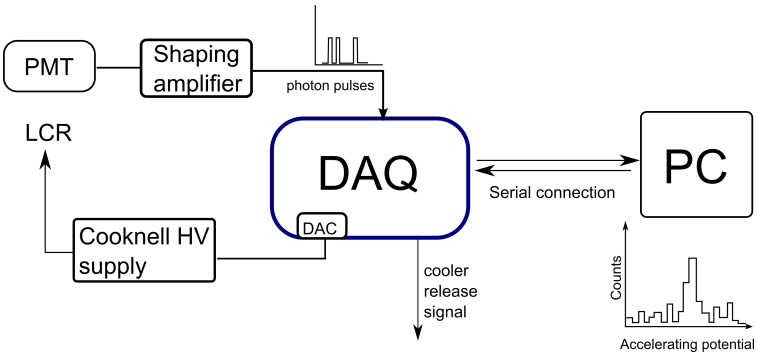

Figure 3.16: A schematic diagram of the new data acquisition system layout.

access to all the data collected over the 100 μs window, allowing for time gating off–line, the creation of photon burst spectra and any photon arrival time corrections.

3.4.3 Initial testing

To test the systems suitability for the collinear laser line a bespoke microcontroller (based on an ATtiny85) was used to simulate experimental photon data, identical to that expected at the IGISOL. The scanning voltage (created from the DAC output of the data acquisition) is read by the ATtiny85 which relates to the x–axis of a predefined Lorentzian distribution (mimicking a resonance structure). A random number is tested against this distribution, which, if valid, signals the addition of a photon to a random position in the produced photon train, as shown in figure 3.17. This photon train is sent a set time after the release signal, imitating the ion time of flight from the Cooler–Buncher, and is recorded by the DAQ. Important design considerations were the time stamping resolution, timing stability, accurate, reproducible DAC output voltages and data storage. The microcontroller timing was observed to 'walk', with a few large deviations during the transmission stage, resulting in a couple of spurious counts. The DAC showed a consistent output, with any deviation well below the intended voltage step sizes.

The availability of microcontrollers with greater RAM provides the potential for a system without the FRAM, as many mobile devices allow for serial communication enabling any data acquisition software to be run from a mobile phone or a suitable tablet. This allows for a truly flexible and portable system, with minimal requirements for installation and use.

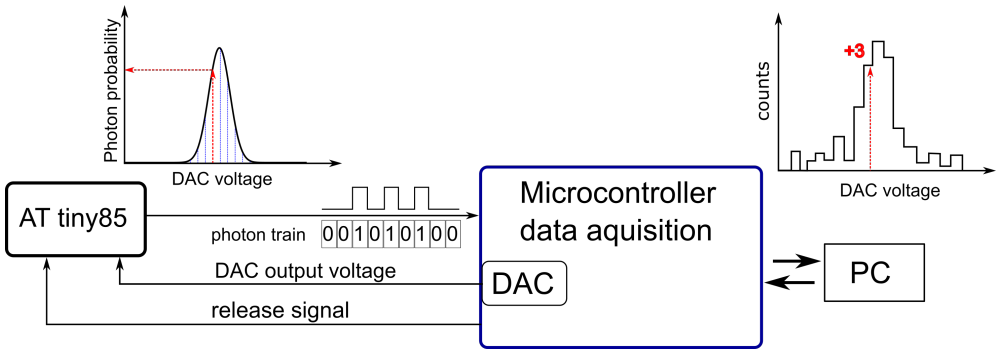

Figure 3.17: A diagram of the data simulator setup for testing the data acquisition system.

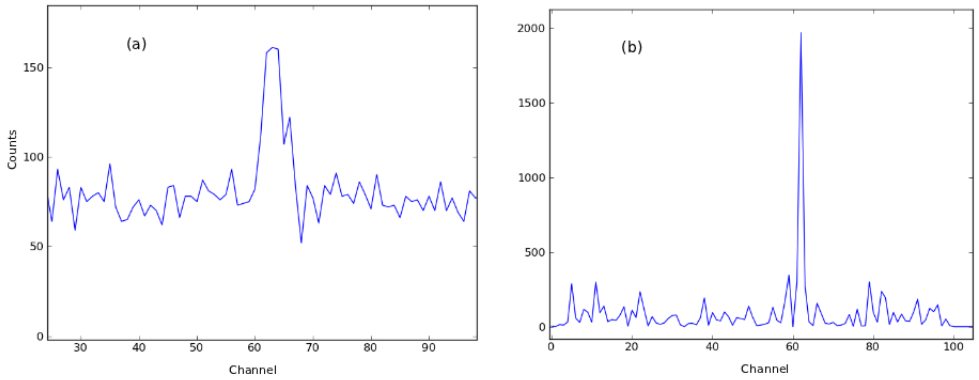

Figure 3.18: Two spectra obtained over 30 minutes for a dwell time of 100 ms taken from the ATtiny85 data simulator. Panel (a) shows a spectrum with a uniform dwell time per channel. Panel (b) was taken using the "photon multiplication" method.

3.4.4 The 'photon multiplication' method

As well as the ability to detect photon bursts the new acquisition system employs a 'photon multiplication' method to aid in location of resonances. The method was previously explored in [44] and consists of adjusting the number of dwells per channel from the usual uniform scanning rate. The number of dwells is set to equal 1+ *total photons already detected in channel*, this allows the scan to spend more time on channels where more photons have been observed. With the simulated data its clear to see the increase in total number of counts observed over a peak (for identical acquisition time), as displayed in figure 3.18.

The total number of dwells and detected photons for each channel are simultaneously recorded and stored. The obtained spectrum can be normalised for the total

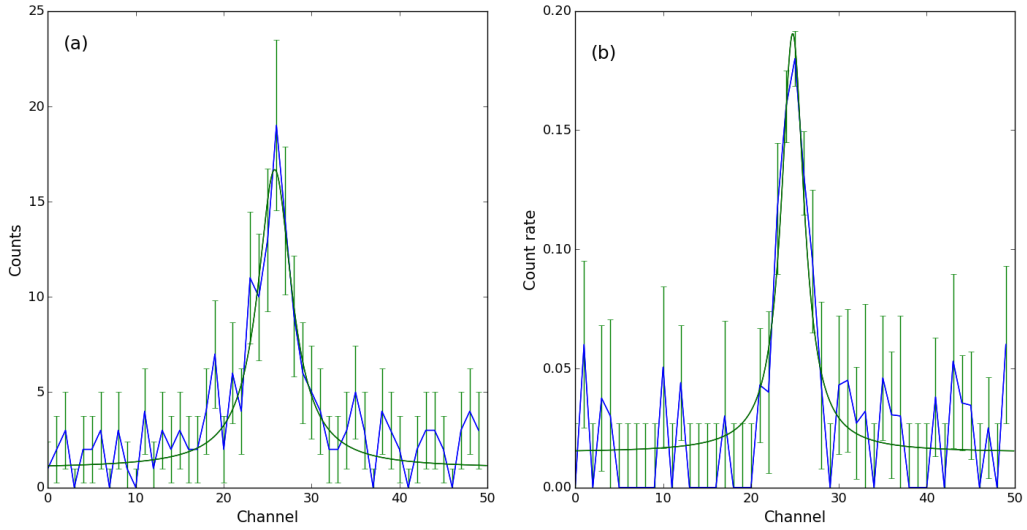

Figure 3.19: Two spectra demonstrating the "photon multiplication method" approach with spectrum (a) taken with the conventional method and (b) showing the rate spectrum taken over the same length of time. Both show a similar signal to background ratio with a Lorentzian least squares peak fits displayed by the black line.

dwells per channel to obtain a photon count rate per dwell. This transformation of the data to photon count rate aids in eliminating statistical anomalies. The rate spectrum would reproduce the same level of signal to background ratio as a conventional scan but reduce the errors (due to the increased number of counts around the resonance peak centroid), enabling an improved determination of the centroid location, as demonstrated through a simulated case shown in figure 3.19. A Lorentzian centred at channel 25, with a FWHM of 4 channels was used as the simulated resonance peak. Panel (a) displays the conventional approach with a Lorentzian fit from least squares minimisation producing a centroid of 25.8 $\pm$ 0.36, whereas panel (b) shows the rate spectrum for the "photon multiplication" method with an extracted centroid of 24.8 $\pm$ 0.13. Crucially both spectra were collected over the same length of time, with a reduction in the centroid error for the latter case.

Chapter 4

ConeTrap, an electrostatic ion trap

The latest addition to the collinear laser beam–line at the IGISOL is an electrostatic ion trap (ConeTrap), mounted at the laser line quadrupole deflector in the low energy section (see figure 3.5). The design is based on an existing trap [10], which was employed to successfully trap ions for over 100 ms with background pressure of $1\times \sim 10^{-7}$ mbar and for periods of $\sim$ 20 s at low temperature ($\sim$ 28 K) and ultra high vacuum ($\sim 10^{-10}$ mbar) conditions [45]. The ConeTrap was previously designed and simulated using the SIMION [46] simulation software, with various electrode shape and configurations explored [9]. This trap consists of two copper, cone–shaped electrodes, separated by a ground potential region, as shown in figure 4.1. The cones are both 75 mm in length with opening diameters of 23 mm and 34 mm and a slope angle of 4.2 degrees. Positive voltages are applied to the front and back cone electrodes to create a potential well, harmonic in both radial and azimuthal directions. In operation the voltage on the front electrode is switched to less than the ion beam energy ($\sim$800 eV at IGISOL) to allow for injection of the ion bunch from the Cooler–Buncher, or extraction from the ConeTrap. The back cone electrode is kept at a fixed voltage above the ion energy to contain the ions within the trap. An asymmetric mode of operation involves higher voltages on the front than the back electrode to produce a 'hard' reflection in the front cone and a 'soft', gradual reflection in the back cone, where the ions are predominantly contained. The high voltage front cone reduces the spatial penetration and provides a greater axial acceleration, reducing the ion density compared to the rear of the trap. The further the ions penetrate into the cone the greater the convergent force they experience. For instance, this causes the ions to adopt wide

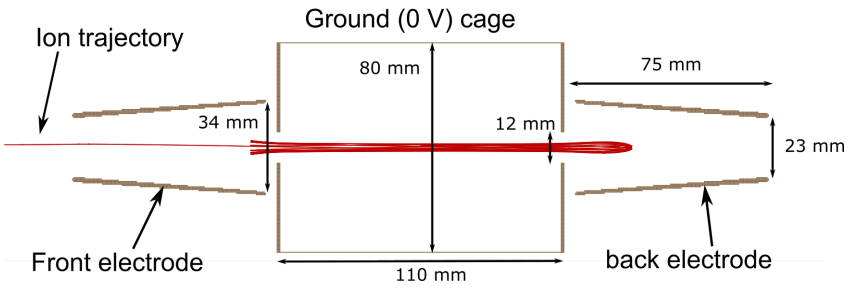

Figure 4.1: Ion trajectories and potentials of the expanded ConeTrap taken from the SIMION simulation program, the red line represents the trajectory of an 800 eV ion of atomic mass 100.

arc trajectories within the low voltage cone, with radial bunching as the ions pass through the central axis. This asymmetric operational mode ensures the ions spend the majority of their flight time within the back cone or the central region, reducing ion losses during injection and extraction through the front electrode. As the shape of the potentials from the electrostatic cones are fixed the stability depends solely on the magnitude of the potentials. For stability the ion trajectories upon leaving the low voltage (LV) and high voltage (HV) cones must match, so that the ions remain on a similar trajectory throughout the trapping time. Differences in the trajectories are due to the changing ratios of the radial and axial force felt by the ion as the voltage (or ion energy) changes, and the distance the ions penetrate into the cones.

The central region has a narrow ion waist, allowing for optimal overlap with a laser beam for optical manipulation. A quartz optical window located in the centre of the mounting flange allows axial optical access to the ConeTrap for optical pumping. The central region is of a well defined electric potential with the two ground plates shielding the potentials of the cone electrodes. A well defined uniform interaction region is required for laser interactions as ions traveling at different velocities (with respect to the direction of the laser) experience different Doppler shifted frequencies. At a mean energy of 800 eV a change of 1 V leads to a Doppler shift of ∼80 MHz for ions of A=100 and light of 300 nm wavelength. Optically pumping within the trap benefits from the effectively long interaction times (due to many orbits around the trap per millisecond) and, unlike the Cooler–Buncher, from low broadening courtesy of low vacuum pressures (better than 10^{-6} mbar). This further suppresses any non–radiative metastable population relaxation.

The advantage of the ConeTrap is its simplicity compared to other ion traps, and the development was undertaken to provide a suitable location for optical manipulation of ions, as suggested by Schmidt [10]. The central region provides a suitable location for in–trap collinear laser interactions, with applications for high–vacuum optical pumping, taking advantage of greatly reduced metastable state relaxation due to background gas collisions, compared to the Cooler–Buncher. The ions can subsequently be released for conventional collinear laser spectroscopy. The ion ensemble can also be optically pre–pumped within the Cooler–Buncher, with the ConeTrap employed as a charge exchange cell, with the detection of a resonant laser effect through the measurement of the changes in ion rates due to the changes in the charge exchange cross–sections between the ground and metastable states. This provides a means of resonance determination through ion detections, which is more sensitive than the conventional photon detection, providing access to spectroscopy on beams that would otherwise be too weak for collinear laser spectroscopy (with the aim of spectroscopy on beams of 1 ion per second). Alternatively the ions can be optically pumped within the ConeTrap itself, taking advantage of the long interaction times and Doppler reduction provided, with a variable central potential region providing a means of Doppler tuning the contained ions. This allows for frequency scanning which can be coupled with either ion detection of a further laser interaction in the collinear laser beam–line. A tunable interaction region allows for spectroscopy with ion detection. The ions are optically pumped into a metastable state with a different electron capture cross–section, changing their survival rate within the ConeTrap. If the ions are Doppler tuned onto the laser frequency then resonance is detected by a change in ions exiting the trap. Several further applications were also explored by Johnson [9], including a radiation transparent 'mesh' ConeTrap for use as a decay spectroscopy station, a double trap design for the containment and separation of 1^+ and 2^+ ions and a 'potential elevator' design, able to change the ion energy during containment. The focus of this thesis will be on the results from the commissioning stages of the ConeTrap (section 4.6 and 5.2) and the exploration of adapted designs towards laser spectroscopy within the trap.

4.1 SIMION simulations

To design and test an optimal ConeTrap for the IGISOL full 3D simulations were constructed using the charged particle simulation program SIMION [46]. The SIMION package models charged particle trajectories through electromagnetic fields by numerically solving Laplace's equation. To facilitate the calculation electrodes/field sources are stored in potential arrays (PAs). Only the areas near relevant ion optics need to be calculated, reducing overall simulation times. The PAs can be 2D or 3D and can be created as planar or axially symmetric, defining each point as an electrode or non–electrode point. A fast adjust definition potential array (.PA#) is also created with each separate independently adjustable electrode structure numerically labeled, where the potentials can be adjusted during the simulation from the base solution through superposition. This approach allows for voltage changes without having to refine the PA each time (which is a relatively slow process). Predefined variables allow for changes to electrodes and access to charged particle properties such as position and time of flight. These can be used to make changes and collect data at any point during a simulated charged particles flight.

In this work the ConeTrap simulations were conducted using runs of 100 ions at a charge state of 1^+ and mass 100 amu, with an initial uniform energy spread of 799.7–800.3 eV. For the stability region plots an ion was considered stable if it survived within the trap for 1 ms. An einzel lens was present in all simulations, located 650 mm away from the front disc of the ConeTrap and set to +250 V to provide a soft focus into the back of the ConeTrap. Effects such as ion–ion collisions and collisions with residual gas were not included in the simulations but their consequences are investigated and described in section 4.5.

4.2 ConeTrap operation

The timing requirements of the ConeTrap and quadrupole deflector HV switches are shown in figure 4.2. Experimentally the ion beam from the Cooler–Buncher is focused onto a Faraday cup located behind the back cone with both cone electrodes and quadrupole elements set to the beam–line potential ('local ground') to allow the ions to pass unhindered. Maximising the current on the Faraday cup ensures a tapered

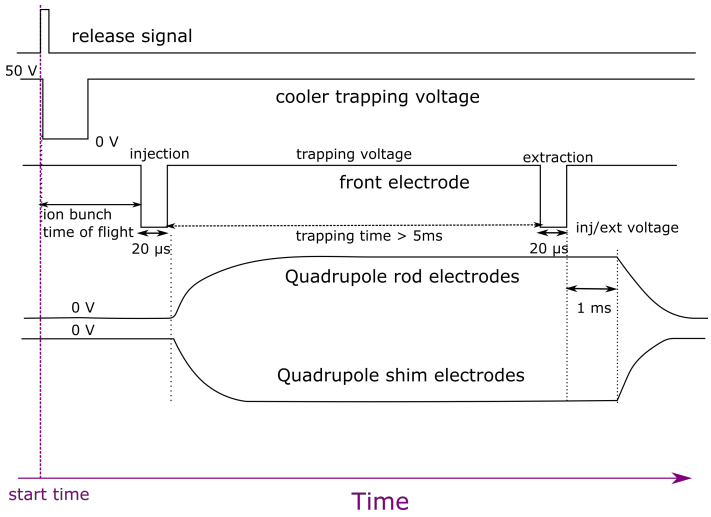

Figure 4.2: The ConeTrap switch timings, displaying the switching of the end–plate, front electrode and the quadrupole bend's rods and shim electrodes (in response to the Cooler–Buncher release signal).

focus into the back cone, which is favorable for ion trapping. When the ConeTrap is in operation the electrodes of the second quadrupole deflector in the low energy section are reduced to the beam–line potential, allowing the ions to pass through and enter the ConeTrap. The front electrode is reduced from around +1300 V to +650 V to enable injection into the trap, while also providing some further focusing into the back cone. The voltage is lowered for 20 μs to allow the $\sim$10 μs ion bunch to enter the trap. The custom built, high–voltage switches are controlled by a microcontroller based unit located at the beam–line platform voltage, more detail on the switches is presented in the Appendix, section A. The signal for the Cooler–Buncher release is relayed to the control unit (and optically decoupled due to the -800 V potential difference between the HV platform and the beam–line). The controller handles the timing and triggers the HV switches on the quadrupole electrodes and the front electrode. Due to the change in time of flight for different $\frac{m}{q}$ ratios the delay between the cooler release and the front electrode switch is adjustable at the control unit. The voltages for the quadrupole elements are only raised for extraction, spending the majority of the time between ion bunches at local ground. The voltages are raised immediately after the ions enter the ConeTrap, which allows at least 5 ms (the set minimum trapping time) for the electrodes to attain the required voltage. They are switched to local ground 1 ms after extraction. The trapping time can also be adjusted from the control box,

which allows for trapping times of 5–100 ms.

The voltage chosen for the ConeTrap injection/extraction provides a focusing effect as the ions pass through the front cone. This focusing can be tuned to obtain optimum injection or extraction. The finite time of switching on the ConeTrap front electrode will cause a "drift tube" like effect for ions traversing the electrode, altering their energy. Fast switching (<0.5 μs) is required to minimise this effect and maintain the ion energy upon injection and extraction. The back electrode is maintained close to the ion energy to maximise the acceptance time of the trap, the longer the ions spend in the back cone, shielded from the effects of the front electrode switching, the longer the temporal bunch the trap can accept. If the ions experience a change in trapping potential then their energy is shifted, increasing the energy spread of the ion bunch and potentially throwing the ions off stable trajectories. On release the potential on the front electrode is lowered to the injection/extraction voltage, allowing the ions to leave the trap after which the quadrupole bend deflects the ion bunch towards the collinear laser beam–line. The temporal bunch length the trap can accept (the acceptance time) is dependent on the voltage of the back cone, the closer the voltage to the ion energy the longer the ions spend in the cone. The acceptance time for +810 V is around 10 μs, which allows for the majority of the ion bunch from the Cooler–Buncher to be captured.

4.3 Collapsed geometry ConeTrap

The ConeTrap design shown in figure 4.1 relies critically on the alignment of the two electrodes, a skew in alignment can cause the ion motion within the trap to become unstable. Initial simulations [9] furthermore showed only narrow stability regions with respect to the front and back electrode potentials. A modified trap, for commissioning purposes, was proposed. In the modified trap the central ground section was collapsed to a single ground plate separating the two cones. This configuration has the advantage of reducing the size and effects resulting from misalignment, while simultaneously expanding the stability regions of the trap. The collapsed design is shown in figure 4.3, with a comparison of the stability regions between the collapsed and expanded traps for the asymmetric mode shown in figure 4.4, with dark blue (1.0

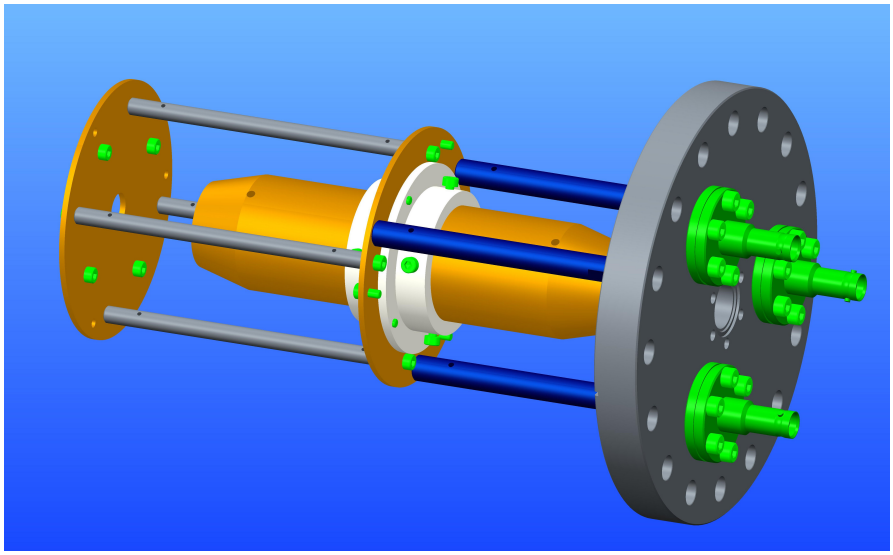

Figure 4.3: A CAD drawing of the collapsed design for the ConeTrap, mounted on the end flange with the electrode SHV feed–throughs and a central space for the quartz window.

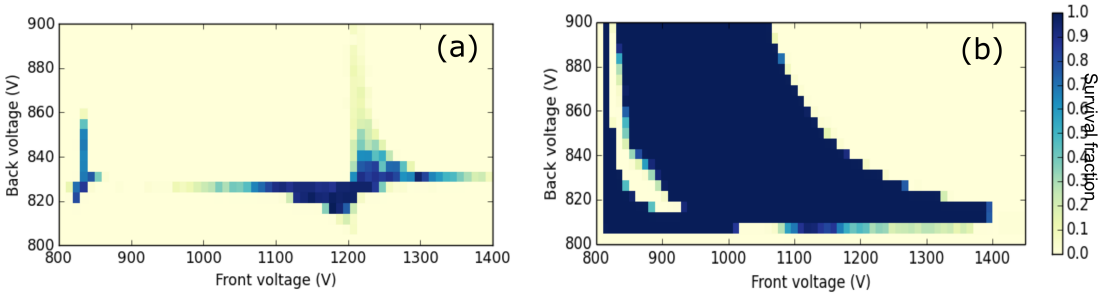

Figure 4.4: 2D plots of the asymmetric mode stability regions for the two ConeTrap designs, (a) and (b) are the expanded and collapsed geometry designs respectively. The huge increase in stable regions is clear for the collapsed compared to the expanded design.

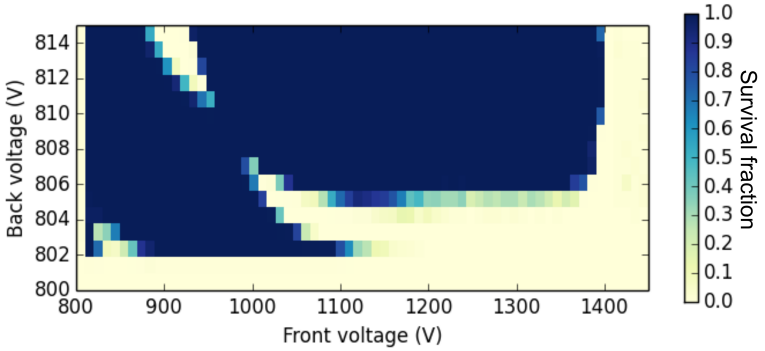

Figure 4.5: A 2D contour plot showing a more detailed scan of the collapsed ConeTrap stability regions at low back voltage settings, with back voltage steps of 1 V.

on the displayed scale) representing 100% ion survival over 1 ms. A more detailed 2D plot is shown in figure 4.5, focusing on the low back voltage region primarily of interest in this work. The vast increase in stable operating voltage regions for the back and front cone electrodes is clearly apparent and this configuration was selected for initial commissioning at the IGISOL–4, detailed in section 4.6.

Key ion trajectory parameters within the collapsed geometry trap (operating in the asymmetrical mode) are shown in figure 4.6, displaying the ion bunching towards the back of the trap. Panel (a) shows the ion trajectory within the trap, showing a hard reflection in the front cone and a soft, slow reflection in the back cone. This is reflected in the ion axial density within the trap (b) where the ions spend the majority of their time within the back cone, the low axial acceleration (c) causes the ions to bunch. Panel (d) shows the radial acceleration experienced by the ions within the trap. Maximum acceleration is experienced near the fringe fields around the central plate.

4.3.1 Optimising the injection and extraction voltages

The injection and extraction voltages provides a focusing effect as the ions enter and exit the trap. The injection potential affects the stability (due to the differing ion entry trajectories) of the trapping and the extraction potential affects the spatial spread (emittance) of the ion beam upon release. The SIMION software package provided a means of determining optimal value ranges for use in the initial commissioning stages

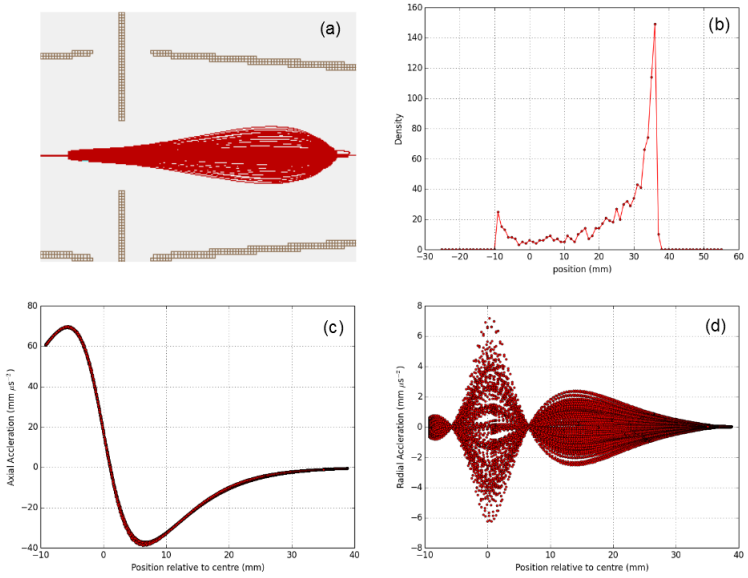

Figure 4.6: Results from a SIMION simulation of 800 eV ions within the ConeTrap with the front voltage at +1350 V and the back at +806 V. Panel (a) displays the ion trajectory with (b) showing the axial ion density within the trap, (c) is the ion axial acceleration and (d) shows the ion radial acceleration across the trap, all with respect to the axial position.

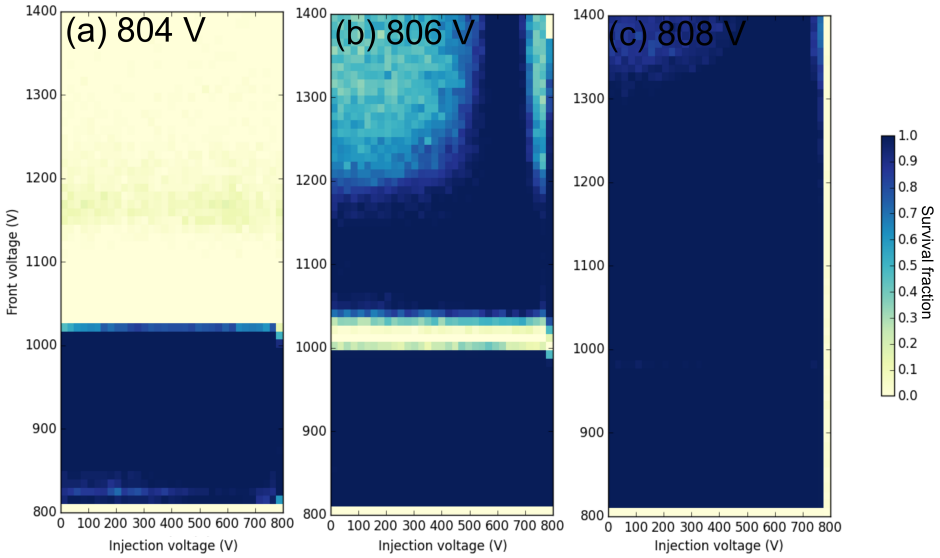

Figure 4.7: Three simulated 2D stability plots of trapping voltage against injection voltage for back voltages of (a) +804 V, (b) +806 V and (c) +808 V.

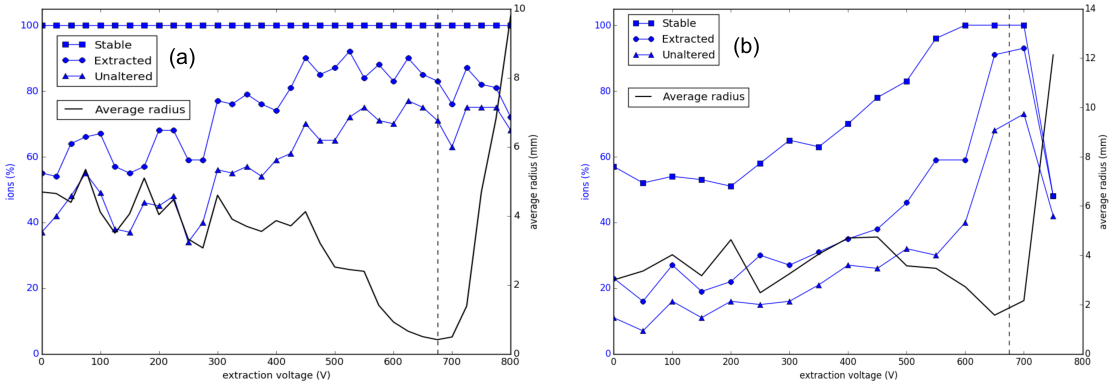

Figure 4.8: Two plots of the injection/extraction voltage, trap stability and the ion release from the trap, for a front cone voltage of (a) +900 V and (b) +1350 V, both with a back cone voltage of +806 V. The data labeled "Stable" shows the percentage of ions that remain stable within the trap, "Extracted" is the percentage of ions successfully extracted and "Unaltered" refers to the percentage of ions released with an ion energy between 799 and 800 eV with the average radius taken from the "Unaltered" ions only.

(section 4.6), with the stability and ion extraction performance explored, primarily focusing on the preferred low voltage region for the back cone. Several stability plots are shown in figure (4.7), for back voltages of +804 V, +806 V and +808 V. The stability regions are as shown in 4.5, with enhanced stability observed within the +550–700 V injection voltage region for back voltages of +806 V and +808 V.

For the extraction efficiency the percentage of ions successfully extracted, the percentage of ions that maintain an energy between 799 eV and 801 eV (unaltered) and the average ion radius (from the trap axis) were obtained from the simulation. The extraction and injection voltages are set equal, mainly due to the increased simplicity for actual trap operation. The average extraction radius was measured 120 mm from the front electrode disc. The results are shown in figure 4.8, which were taken with a back cone voltage of +806 V and a front voltage of, panel (a), +900 V and, panel (b), +1350 V, panel (a) is well within stability and panel (b) near the simulated stability limits. Panel (a) shows optimal ion extraction performance above an extraction voltage of +450 V and an average radius minimum at +675 V. Panel (b) displays the increased extraction performance following the improved stability up to +600 V and a sharp peak in performance between +650–700 V. The peak extraction efficiency reaches 80% for ions that maintain their energy near the initial injection energy. This

panel also displays an extraction radius minima around +675 V. Both plots display a sharp rise in the average ion radius past +700 V, displaying a strong focus out of the trap, which is diverging shortly after extraction. The improved extraction performance around the average radius minimum is due to a reduction in the extracted ions colliding with the grounded shielding disk electrode, mounted before front cone electrode. On extraction the ions may adopt trajectories that collide with the shielding disk electrode, or diverge sufficiently within the trap to be lost before extraction, due to a shift in ion energy from the varying front cone potential. The results show unaltered ion extraction efficiency between 70 and 80 %. For the initial commissioning stages injection/extraction voltages in the +600–700 V range are optimal, with a clear performance peak near +675 V region for the HV trapping potential region near the limits of stability.

4.3.2 Energy spread on extraction

A critical consideration for collinear laser spectroscopy is the energy spread of the ion ensemble. A wide ion energy spread greatly decreases the efficiency, due to the reduced fraction of the ensemble on resonance. It also causes a greater broadening to the measured hyperfine peaks, reducing the resolution and the accuracy of the results obtained. A wide energy spread on extraction would lead to the ion ensemble to be 'analysed' by the quadrupole deflector, with potentially reduced transmission efficiency to the end of the laser beam–line. The ion density within the trap homogenise around the trap after about 1 ms, so on release there is no structure to the energy spread unlike with the Cooler–Buncher where the higher energy ions leave the trap first. To maintain a small energy spread the switching of the trap potential needs to be fast ($\sim 1\mu$s), and the potentials must possess minimal drift and minimal noise. Details of the HV switches are presented in the Appendix, section A.

4.4 Central interaction regions

The greatly enhanced stability achieved with the collapsed geometry motivated a series of explorations of hybrid designs that maintained the attractive broad stability while providing a uniform field laser interaction region. A region of uniform potential

field will create a region of constant ion velocity and therefore constant experienced Doppler shift with respect to incident light. This will greatly increase the time available for a laser–ion interaction to occur. It was necessary to ascertain if the collapsed geometry trap possessed a reasonable region for laser interaction and also to provide a direct comparison for the hybrid designs. The energy spread of the ionic ensemble remains constant within the trap so the acceleration felt by the ions as they orbit the trap provides a velocity spread compression as the ion velocity increases, reducing the Doppler widths to ∼80 MHz at the velocity maxima at the centre of the trap. At the turning points the axial velocity reaches zero, and the energy spread of the ion ensemble affects the axial location spread of the turning point within the cone electrodes. Therefore the velocity maxima provide the narrowest linewidths for laser interactions and a clear option for an extended uniform potential region, combining the reduced Doppler width due to velocity bunching with an increased interaction time. The ion distribution across the velocity range is critical, increasing the time the ions spend within a given velocity region increases the interaction probability at that respective velocity/frequency. The turning points in the cone electrodes provide relatively long interaction times due to the low velocities. A well defined, constant potential minimises velocity changes over the region and ensures the ions experience a constant Doppler shift, providing suitable time for single frequency laser–ion interactions. At 800 eV the (A=100) ions traverse about 4 mmμs^{-1}, so an interaction length of 2 mm would provide about 1 m of interaction length and 250 μs of interaction time over 500 orbits in ∼5 ms.

To assess the photon interaction probability within the ConeTrap the axial velocity and time of flight over 100 orbits of an 800 eV ion within the ConeTrap were taken from the SIMION simulation. A histogram across the axial–velocity range was created, with the bin heights equal to the time spent by an 800 eV ion within the respective velocity bin range (over 100 orbits). This provides a clear indication of which velocity regions the ions predominantly inhabit over the containment time. The velocity range is used to create a profile across frequency space. For each velocity bin the Doppler shift is calculated relative to a reference frequency, a wavelength of 300 nm ($\sim 10^{15}$ Hz) was chosen as many of the optical pumping cases are in the UV region of the EM spectrum.

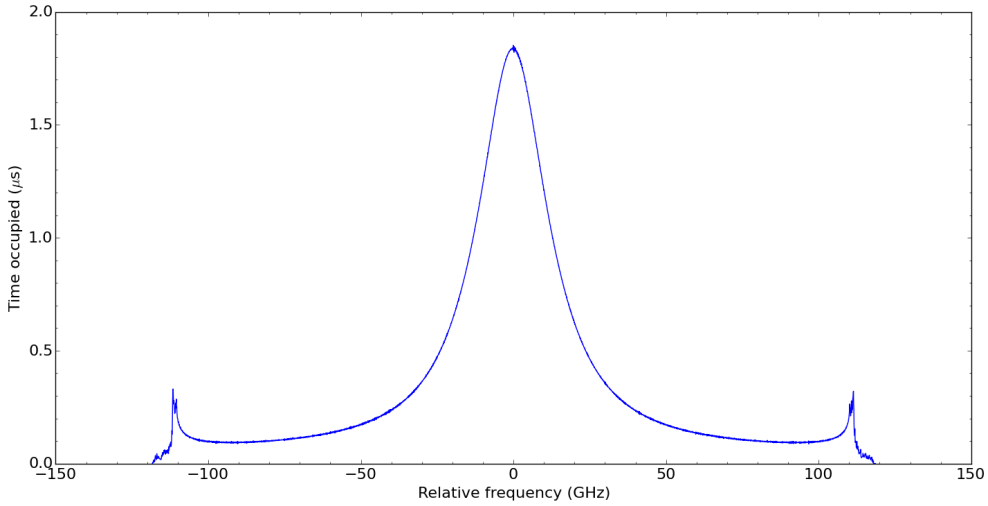

Figure 4.9: A plot of the time spent by an ion (over 100 orbits) across the axial velocity distribution of the trap, shown as frequency relative to a central frequency of $\sim 1.0 \times 10^{15}$ Hz (300 nm).

While the collapsed ConeTrap design greatly improves the stability regions and ease for commissioning its comes at the expense of a suitable well–defined laser interaction region, as shown in 4.9. The small, poorly defined peaks at the velocity maxima show the limited time the ions spend at the velocity maxima, combined with the non–uniformity of the potential shown by the range of velocity maxima from differing ion trajectories. For efficient laser interaction the ions and laser must overlap spatially, temporally if pulsed and the ions must be at a well–defined velocity over the interaction distances if narrow–width light sources are employed. To maintain some of the wide stability afforded by the collapsed design, while incorporating a suitable interaction region several designs were simulated.

4.4.1 A central tube insert

The addition of a central tube–electrode within the collapsed geometry ConeTrap, as shown in figure 4.10, allows for an adjustable, well–defined central field, while still maintaining much of the improved stability offered by the collapsed design. The additional electrode enables the potential of the central plateau to be adjusted through a specified range, Doppler tuning the ions with respect to the incident light within the ConeTrap (similar to the LCR setup, see figure 3.9). Any additional structure

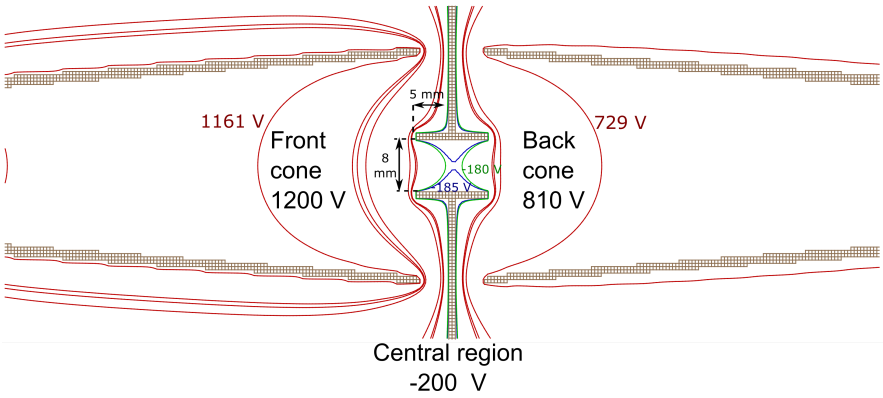

Figure 4.10: A contour plot produced in SIMION of the central potential region with the central tube insert. The back cone is at +810 V, the front at +1200 V and the central region is at –200 V.

to the central region restricts the voltage stability regions, leading to a compromise between stability, voltage range for the central section and definition of the central potential. A narrow, long tube will produce a better defined potential with a longer interaction length, but significantly reduces the stability regions compared to that achieved with open cones. This arises due to the field perturbation caused by the central structure and geometrical reduction of the acceptable emmitance from both cones. A wide stability range with respect to the front and back electrodes is required, to account for any voltage fluctuations (or differences from simulations) while still in this commissioning stage. To compromise between the stability and interaction length, a size of 11 mm in length and 8 mm inner diameter was chosen for the simulations, mounted in the central plate and isolated from the grounded casing as shown in figure 4.10. The central field region is represented by contours, with the voltage at the centre of the saddle point at –184.5 V (central electrode held at –200 V). The central region shows a variation of 5 V over 2.5 mm axially and 1 mm radially at the saddle point, providing more than 250 μs interaction time (over 5 ms). A spread over 5 V leads to a frequency spread of about 250–400 MHz (depending on ion mass and central potential), making this suitable for medium to broadband spectroscopy.

The 2D stability plots shown in figure 4.11 show a clear shift and a small reduction in the stability regions, compared to the collapsed geometry but still far improved over the initial extended design. With the addition of the central tube insert the low back voltage, high front voltage region of interest is narrower, with future commissioning (of the section) requiring operation at a reduced front cone voltage range (1100–1200

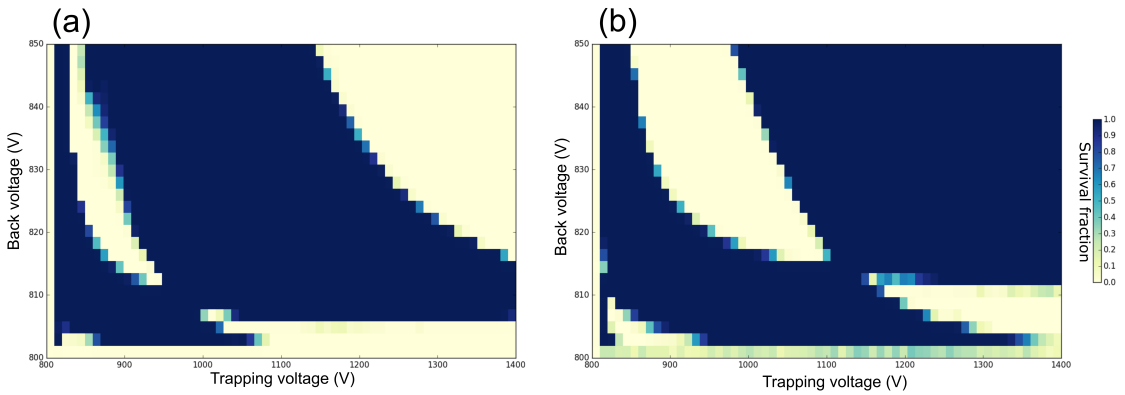

Figure 4.11: A 2D stability plot comparison of the collapsed ConeTrap without (a) and with (b) the central tube insert, held at a potential of 0 V.

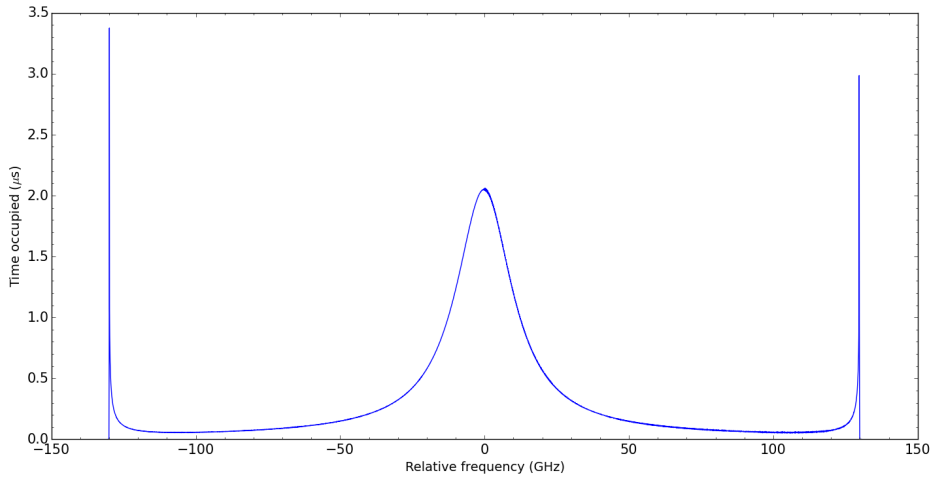

Figure 4.12: A plot of time occupied by an ion over 100 orbits as a function of Doppler frequency shift experienced relative to an initial frequency of $\sim 1.0 \times 10^{15}$ Hz.

V).

Figure 4.12 shows a histogram of the time spent by an ion across the axial velocity (frequency) range, calculated with the central tube insert present (which was set to 0 V). Compared to the collapsed geometry profile, shown in figure 4.9, it shows a great improvement in the ion occupation at the velocity extremes (within the central tube), due to the increased flatness of the potential at the centre, allowing for a longer time spent at that specific Doppler shift. As the negative scanning potential is increased the energy of the ions at the central region will increase, causing further reduction in the Doppler width.

For ion–laser interactions a good spatial overlap between the ion waist and the laser

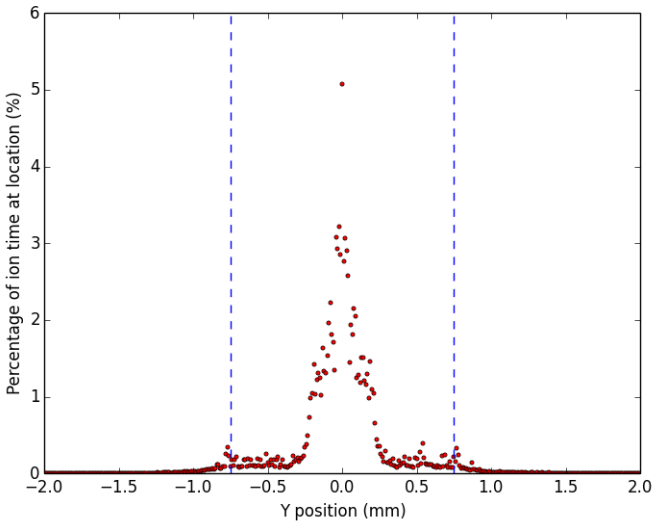

Figure 4.13: A binned histogram of the radial positions (perpendicular to the main trap axis) of ion traveling within the central region, binned at 0.01 mm spacings. The height of the bins represents the percentage of the total time spent within each 0.01 mm slice, with the ions spending 95% of the transit time within a 0.75 mm radius of the central axis.

beam is desired, the central tube insert can be set to negative voltages to further focus the ion beam within the central region. The 'saddle back' form of the central tube potential leads to a shift in ion potential away from the central axis (z–axis in SIMION), with a spread of axial velocities depending on the radial position of transit through. The SIMION simulations were used to extract the ion beam radial distribution as it passes through the central tube (at 0 V). To determine the average radius of the beam profile the x and y positions (the radial axis) of the ions were recorded within the central region every 0.01 μs, for a range of front and back voltages. Taking a projection of the data onto the Y axis, by binning the data every 0.01 mm, a plot representing the percentage time spent within each 0.01 mm segment. The ions spend 95 % of the flight time through the central electrode within a 0.75 mm radius of the central axis as shown in figure 4.13, leading to roughly 66 % of the ions remaining (radially) within 5 V of the central point potential.

Operational considerations

The SIMION simulation package can be powerfully used to develop strategies for the initial testing and development stages of the ConeTrap under on–line experimental

conditions. While scanning the central potential region it will be imperative that the chosen voltage combination for the front and back remains within the stability region over the scanning voltage range. The central tube electrode may be either positive or negative potential, leading to a range of possible scanning regions. The potential applied to the central electrode distorts the harmonic potentials near the cone openings, leading to changes in spatial penetration into the cones. Depending on the polarity of the central potential different voltage regions will be preferred for optimal stability. Figure 4.14 shows ion trajectories at the extreme limits for both polarities. A positive central region is more likely to have stable orbits at a lower front voltage due to the reduced spatial penetration caused by the central potential region raising the field. For a negative central field the ions penetrate further into the cones, making a higher front potential more preferable. The location of the ion beam waist moves depending on the ratios of the asymmetric voltages, for laser interaction a group of orbits with a narrow central waist are preferable to increase laser–ion overlap. The available range varies from +500 V to –2000 V central region depending on the cone voltages, however no one combination will be stable over the whole range. Combinations suitable for adjustment ranges of a few hundred volts are readily obtainable. A stability plot with respect to central tube voltage and the front voltage at a fixed back voltage of +806 V is shown in figure 4.15. Broad stable regions are readily obtainable with negative voltages, particularly favouring higher front cone voltage settings, however positive central voltages tend to produce significant instabilities and are not recommended for initial testing. The plot shows stable regions for larger negative tube voltages require larger trapping voltages. The regions are several hundred volts across, allowing for stability over a wide range of tube voltages for potential Doppler tuning.

4.4.2 A shielded central region

The addition of 'lipped' electrode plates has previously been successful in reducing fringing fields in electrostatic systems [9]. A modification to the central tube design that involves expanding out the two cones and enclosing the central tube region between two lipped ground plates has been explored here. This modification reduces the field distortions, allowing for the central field region to be tuned over a wider voltage range without disrupting the stability of the trap (with the ions returning to ground

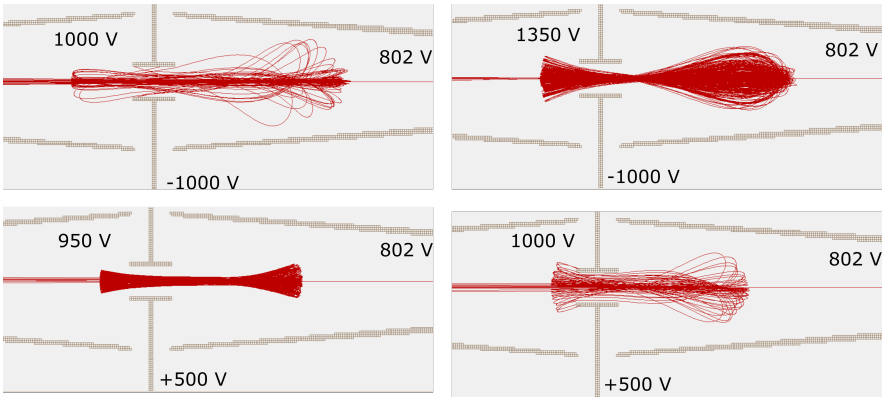

Figure 4.14: Four ion trajectory traces from SIMION, showing that for a large negative central potential a higher front potential leads to stability (and the opposite trend for positive central potential).

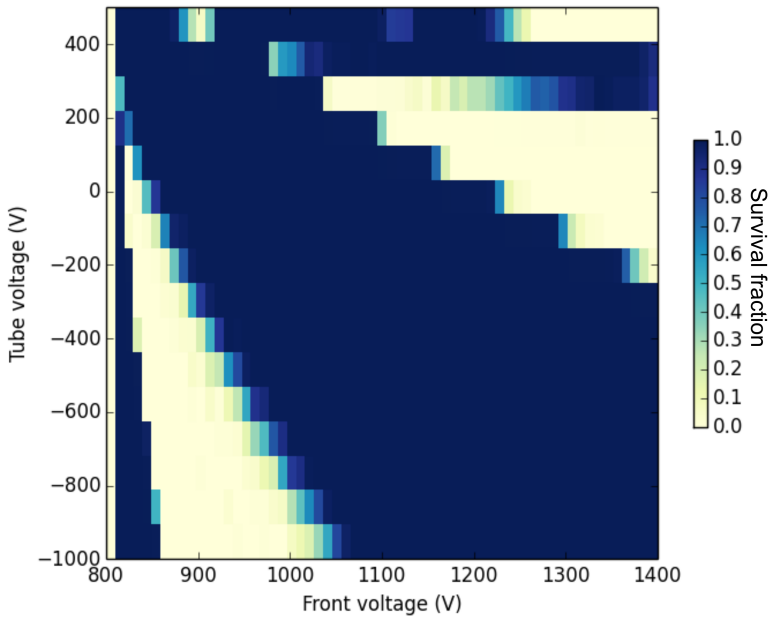

Figure 4.15: A 2D stability plot from simulation of the ConeTrap with a central tube section, the back cone voltage was kept constant at +806 V while the front and tube voltages were adjusted.

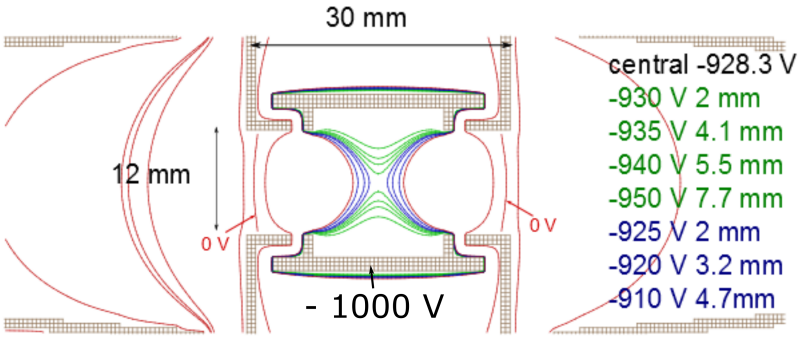

Figure 4.16: A drawing from SIMION showing the central region design with the two lipped ground plates. The back cone is at a voltage of +810 V, the front is +1200 V and the central electrode is –1000 V. The potential at the trap centre is −928.3 V, with each voltage and distance listed referring to the potentials of the contours vertically (and separation) and horizontally.

potential before re–entering the cones). The modified design considered is shown in figure 4.16. The potential on both sides reaches 0 V before the cone electrodes, allowing for the harmonic cone potentials to be unperturbed by the central region potential.

The distribution of time spent by an ion across the velocity regions (shown as a frequency shift) within the trap is shown in figure 4.17. This displays far greater potential for laser interactions compared to both the central tube insert, figure 4.12, and the collapsed design, figure 4.9. The increased size of the velocity maxima peaks compared to the collapsed trap and the central tube insert are due to the length and 'flatness' of the potential in the shielded central region. This displays a greatly improved region for laser interactions.

This design also allows for much higher central region voltages with the trap observed to be stable to –5000 V in simulation (although the stability regions are shifted by the change in central voltage as shown in figure 4.18). A shift and expansion is observed in the stability regions with increasing tube voltage, with the low back voltage stability region (of interest) expanding and shifting towards higher front voltage values. For a back cone potential in the range +805–810 V and a front cone potential between +1100–1200 V is observed to be an optimal initial value, displaying stability across the 0 V to –1500 V central region voltage range. Although this region is narrow at ground potential, it becomes much broader with a higher applied negative voltage.

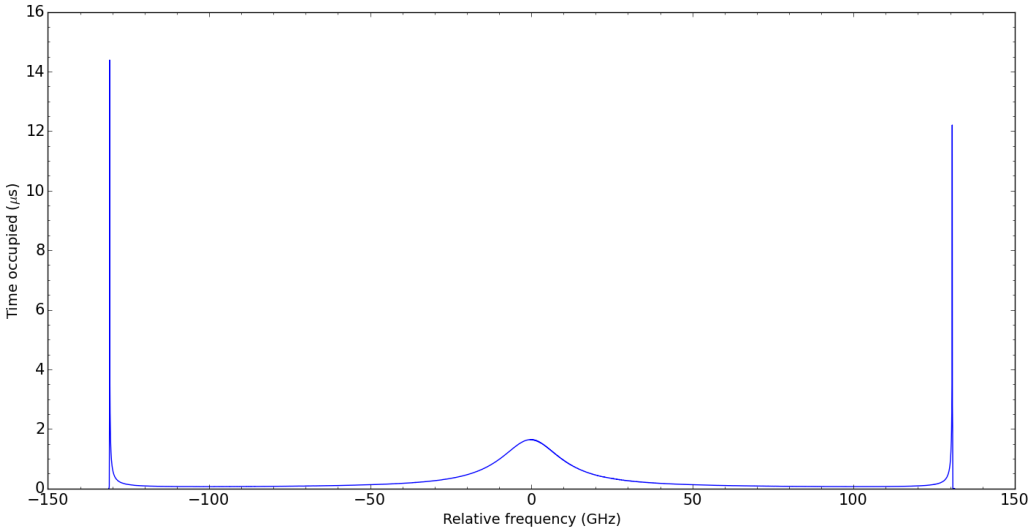

Figure 4.17: A plot of time spent by an 800 eV ion (over 100 orbits) at a particular Doppler frequency shift experienced within the ConeTrap (with the central region inserted) relative to an initial frequency of $\sim 1.0 \times 10^{15}$ Hz.

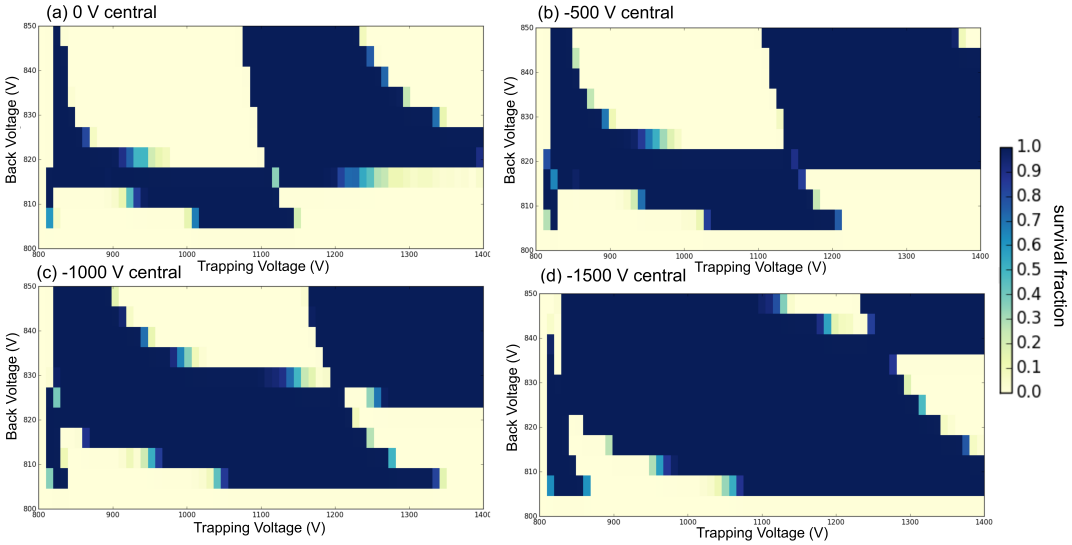

Figure 4.18: 2D plots showing the change in stability regions for the enclosed central region design, set at (a) 0 V, (b) –500 V, (c) –1000 V and (d) –1500 V.

This design provides a greater tunable laser interaction region compared to the central tube insert, while still possessing wider stability regions than the initial expanded trap design.

4.5 Loss methods and vacuum considerations

The two main processes resulting in ion losses within the ConeTrap are ion–ion and ion–gas collisions. These lead to changes in the ion energy, resulting in unstable trajectories, or charge exchange and neutralisation of the ions. Ion–ion collisions will dominate at high ion densities within the trap (and low vacuum pressures), limiting the total number of ions the trap can hold. Considering the total loss rate Γ as defined by the change in stored ions, dN, over an infinitesimal time, interval dt:

$$dN = -N\Gamma dt \tag{4.1}$$

where Γ will consist of contributions from all loss effects (but dominated by residual gas collisions [45]). At low ion densities where residual gas collisions dominate, Γ is just the residual gas collision contribution Γ_{rgc} and equation 4.1 becomes,

$$N(t) = N_0 e^{-t\Gamma_{rgc}}$$
$$\Gamma_{rgc} = \frac{1}{\tau}$$
$$\tau = \frac{k_\beta T}{< v.\sigma > P}$$

where N is the number of ions, t is time, τ is the average lifetime within the trap and σ is the electron capture cross–section. The average lifetime is affected by the temperature, T, the background pressure P and the average ion velocity multiplied by the electron capture cross–section (due to the changing ion velocity and hence cross section as the ions move within the trap) [11]. At low velocities the non–resonant electron capture cross–section will be weakly dependent on the ion velocity. If the ion density is high then ion–ion collisions dominate and a new term $\Gamma_{ii}(t)$ is introduced to the total rate Γ, which is dependent on the ion number and can be represented as $\Gamma^0_{ii}\frac{N(t)}{N_0}$. Here $\frac{\Gamma^0_{ii}}{N_0}$ is a constant depending upon the geometry of the trap and orbitals and the ion–ion collisional cross–section. Substituting into equation 4.1 gives a

differential equation with an analytical solution in the form of [45]:

$$N(t) = \frac{N_0}{(1 + \Gamma^0_{ii}\tau_0)e^{t/\tau_0} - \Gamma^0_{ii}\tau_0} \tag{4.2}$$

To increase the average lifetime of ions within the trap the ion number can be kept low, to reduce potential ion–ion collisions. The ion–gas collisional losses may be reduced by reducing the background pressure in the ConeTrap. The mean ion lifetime within the ConeTrap is lower for a symmetrical high voltage mode compared to a low voltage mode due to the higher average ion velocity [11], in both cases the ions travel the same mean distance before collision or charge exchange. The asymmetrical operating mode provides a compromise in survival for reduced losses on extraction and increased acceptance time on injection. During the initial tests the pressure within the ConeTrap was between 10^{-6} and 10^{-7} mbar, mainly due to the helium buffer gas leaking from the Cooler–Buncher.

Essential improvements are planned at the IGISOL and will include the addition of a turbo pump directly below the second quadrupole bend in conjunction with an ion pump already installed at the ConeTrap region. This will reduce the pressure in the ConeTrap to below 10^{-7} mbar.

4.6 Off–line ConeTrap tests

The collapsed geometry ConeTrap was successfully tested at IGISOL in 2014. Stable ion beams were produced in the IGISOL chamber via electrical discharge from a source of the element under study (nickel and barium were used for this off–line work). The ion bunches from the Cooler–Buncher were injected into the trap, stored for 5 ms before extraction and transported to the end of the laser beam–line where they were detected by the multichannel plates (MCPs). A 15 ms bunching time allowed sufficient time for the quadrupole shim and rod electrodes to switch to steady voltage. The ions released from the ConeTrap were reduced in intensity (by both use of an attenuating mesh before the Cooler–Buncher and reduced SPIG RF amplitude) to maintain a rate below 50 counts per second. This prevented saturation of the MCPs, ensuring rates below 100,000 per second, or a maximum of 1 ion within a 15 μs window (a rate of $\sim$ 66 per second at 15 ms bunching). The ion energy was measured by keeping the

front electrode at local ground and applying a voltage to the back cone electrode. The ions traveled through the back cone electrode until the applied potential was equal to or greater than the ion energy, this was found to be +798–800 V as read from a Cooknell power supply. With optimal beam–line transport a maximum of 1 ion detected at the MCPs for every 200 injected was observed for ^{130}Ba. This figure was calculated from the measured ion current on the Faraday cup located at the back of the ConeTrap, reduced by a factor of 3 (due to secondary electrons) and then scaling from the observed current of ^{138}Ba with a relative abundance of 71.7% to the ion count of ^{130}Ba with a relative abundance of 0.106%. This rate was observed at settings of +807 V for the back electrode, +1250 V for the front electrode trapping and +625 V for injection/extraction (as requested from the Cooknell and Hewlett Packard power supplies respectively). The injection/extraction voltage was kept at half the requested trapping voltage through a potential divider, which kept the voltage within the simulated optimal performance range (for front voltages of +1200 V and above) as previously explored in section 4.3.1.

A further off–line run in 2014 re–established the previous conditions, with minimal effort showing that the previous results were easily repeatable and providing a template for establishing ConeTrap operation for future runs. An injection/extraction efficiency of $\sim$ 1 in 200 was again observed.

4.6.1 Probing the stability regions

To measure the ion energy after extraction from the Cooler–Buncher the back cone electrode was employed as an electrostatic barrier and the ion current on a Faraday cup was monitored while raising the voltage on the back cone. The measured current reduces to zero when the voltage approximately matches the ions energy. A test was performed with a 95 pA ^{58}Ni beam (as read on the Farady cup), with a bunching time of 10 ms, and the results shown in figure 4.19. The current displays a drop off to less than 1 pA at a value of +800 V on the Cooknell power supply. The next point obtained at +810 V shows the beam is completely reflected. SIMION simulations predict total reflection at an applied voltage +802 V (due to the lower field at the centre of the cone), which matches well with the observed behaviour. An alternative method is observing the point at which, with respect to the back cone voltage, the operating

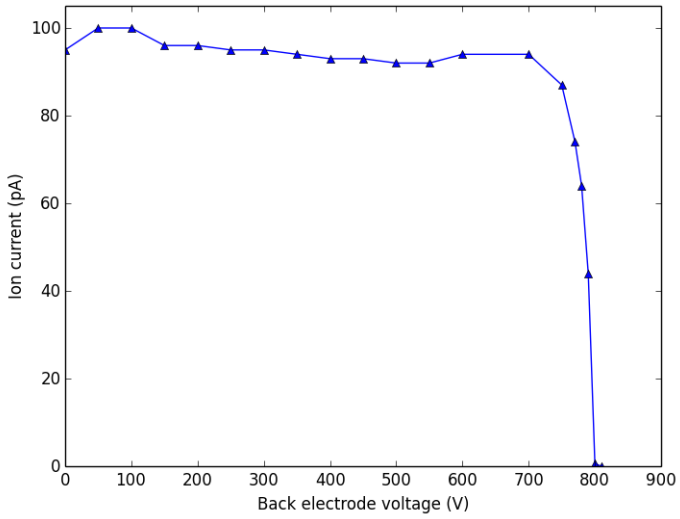

Figure 4.19: A plot showing the change in ion current measured on a Faraday cup located at the rear of the back cone, the current shows a sharp drop off after +750 V, reaching 0.7 pA at +800 V.

ConeTrap ceases trapping. This was performed in 2014 with the ion current measured by the MCPs while the back voltage was adjusted (the front electrode potential was kept constant at +1350 V). The ConeTrap was observed to continue trapping ions until a requested voltage of +795 V from a Cooknell power supply, 5 V below the expected ion energy, and 7 V below the simulated minimum required voltage for reflection of +802 V. For a uniform ion bunch of energy spread of 799.7–800.3 eV at mass 100 a, simulations show trapping starts at +805 V for front voltages above +1100 V (see figure 4.5). This suggested a systematic offset in the actual voltage supplied compared to the requested for either the Cooknell power supply or the accelerating potential supply or both.

Back voltage supply calibration

Due to the apparent stability below +800 V, (the requested ion accelerating potential) it was necessary to accurately calibrate the voltages applied from the Cooknell power supply. These were measured using a voltage divider stack and high impedance voltmeter, primarily used to record the applied HV platform voltage for the Cooler–Buncher. The measured voltages as a function of requested voltage (as read from the supply monitor) are shown below in figure 4.20, where a near constant offset of

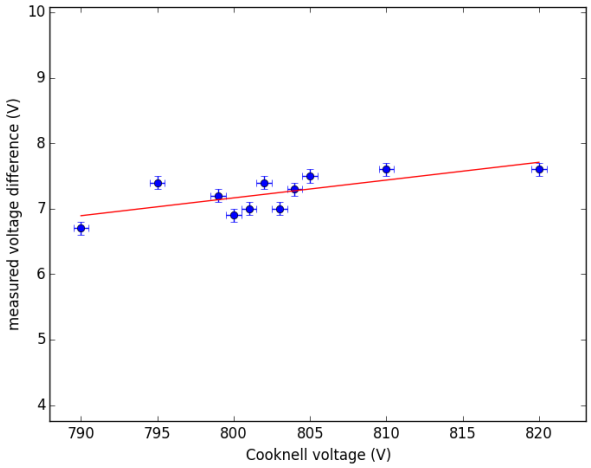

Figure 4.20: A plot of the difference in supplied and requested voltage from the Cookell HV power supply as a function of the requested voltage, the error on the measured value is 0.05 V.

+7–8 V between the requested and applied voltages is observed. A slight increase in offset is displayed as the requested voltage is increased. Correction of the readings for the linear fit from the data leads to the data taken for the ConeTrap being found to perfectly match the SIMION simulations, and all subsequent reference to applied back cone electrode voltages are not as read from the supply but have been adjusted using the linear fit from figure 4.20. This correction, while appearing applicable for the July data is at odds with the initial measurements of the ion energy, suggesting a potential long term drift in the offset of the power supply.

Stability regions

The stability regions, with respect to the front and back voltages, of the ConeTrap were observed and compared to the simulations. The back cone voltage was adjusted for incremental values of the front cone voltage and the total ion current was measured. The back voltage was increased until the edge of the stability region was reached, where the ion rate dropped to background (dark count) levels. The data is shown in figure 4.21. The stability range with respect to the back voltage increases as the front potential is reduced from +1400 V to +1100 V. The limits of stability as estimated by SIMION simulations are represented by dashed lines. The observed trap performance

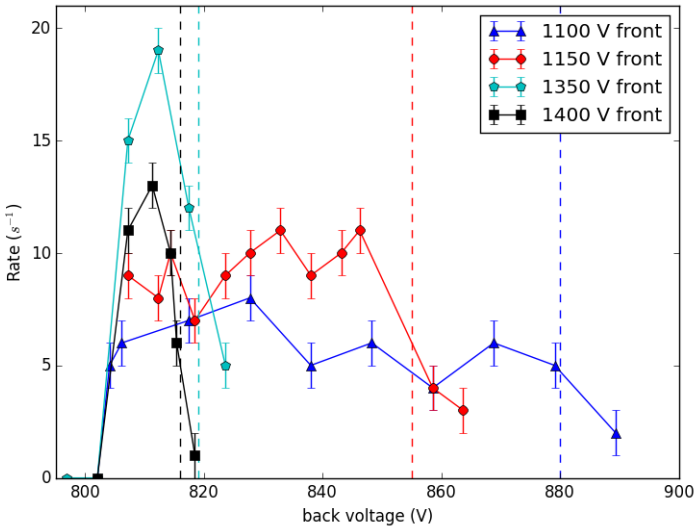

Figure 4.21: A plot displaying the extracted ion count rate from an operating ConeTrap (5 ms storage) as a function of the back electrode voltage. The simulated limits of stability are marked with dashed lines on the plot.

matches well with the general trend of the simulations, but it would appear the simulations systematically underestimate the stability range, particularly at lower front potentials.

The operational behaviour of the trap was compared in detail to the SIMION simulations for a front potential of +1150 V, for both stability and ion release parameters. The results are shown in figure 4.22. The expected stability regions and ions released match well, however the drop in the simulated unaltered energy ions (ions which are extracted and maintain an energy between 799 and 801 eV) is not observed in the real data, despite the quadrupole bend acting as an energy filter. This is probably due to the relatively broad energy acceptance range for the "IGISOL operating mode" of the quadrupole deflector [9].

The trap performance with respect to the front cone potential was also investigated, while maintaining a voltage of +814 V (807 V as requested from the Cooknell) on the back cone electrode. The plot shown in figure 4.23 clearly shows an instability region around +900 V, between about +880 V and +950 V, which compared to the fine voltage scan in figure 4.5 matches well with the simulated stability.

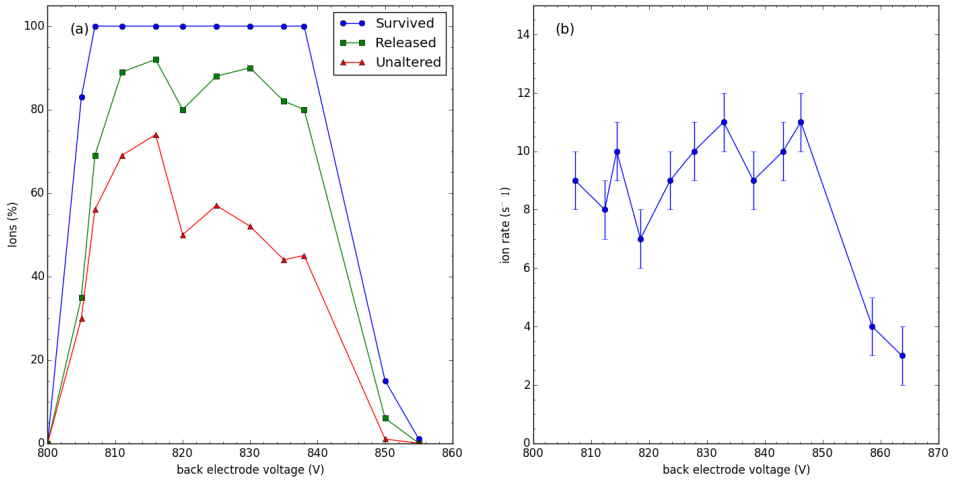

Figure 4.22: Panel (a) shows the simulated behaviour of the ConeTrap as a function of back voltage, displaying trapping survival and behaviour on extraction. Panel (b) show the ion count rates as a function of calibrated back electrode voltage (all with a front voltage of 1150 V).

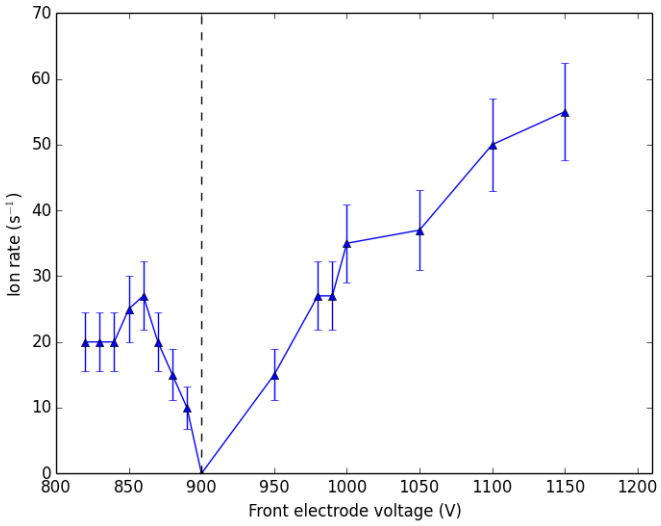

Figure 4.23: A plot showing the measured current ejected from the ConeTrap as a function of front electrode voltage (back electrode voltage at +814 V).

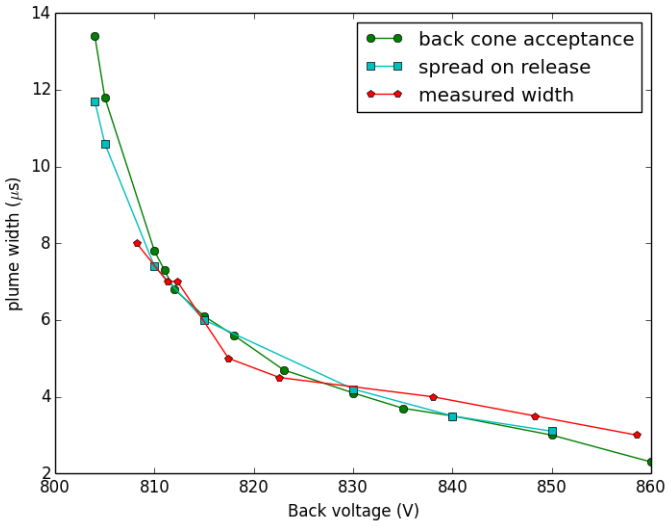

Figure 4.24: A plot showing the measured temporal bunch lengths as a function of back cone voltage (with the offset correction), compared to simulated values from the back cone acceptance and the simulated temporal spread on extraction (given at a fixed point from the front cone).

4.6.2 The temporal length of the ion ensemble

A sensitive probe of the ConeTrap simulations efficacy is provided by the temporal length of the ion bunches upon release, which was observed experimentally using a digital storage oscilloscope (DSO) using the amplified signal from the MCPs, with the Cooler–Buncher release signal as a trigger. The ion bunches were observed to arrive ∼5.2 ms after the Cooler–Buncher release, as expected with the requested 5 ms containment plus the ion time of flight before and after the ConeTrap. The ion bunch temporal length was measured from time–of–flight histograms, taken as the period between the start and the end of the bunch. The results are shown in figure 4.24, along with comparisons to the simulated values for the respective back electrode voltage. For the compression of the bunch in the simulations it is assumed that the temporal length is defined by the acceptance time of the back cone. This is the time window the ions spend deep enough within the back cone electrode to be shielded from the effects of the switching front electrode potential. Due to the field penetration in the collapsed design this was taken as 15 mm away from the ground plate into the back cone, as shown in figure 4.25. A distance of $\geq$ 15 mm was chosen due to the change in potential observed (at this point) being less than 1 V as the front electrode

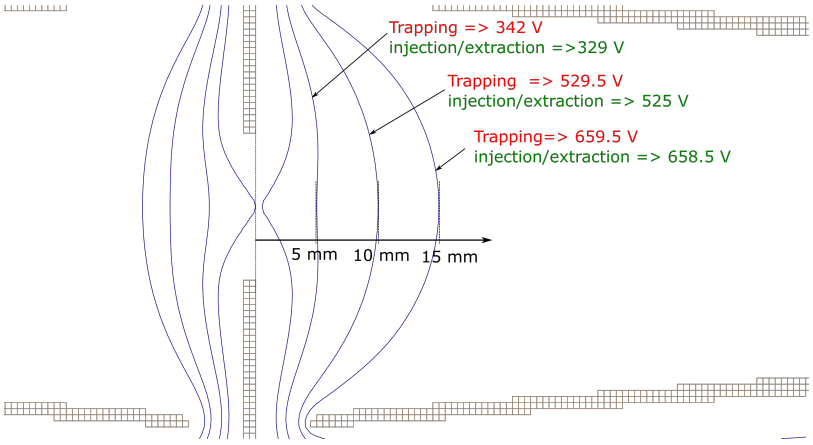

Figure 4.25: A figure from the SIMION simulation with potential contours showing the penetration of the front cone electrode field into the back cone, with the contours set at fixed distances from the central plate and their respective values with the front electrode set to +1150 V (trapping) or +575 V (injection/extraction).

is switched between the injection/extraction and trapping potentials. The ion time of flight on extraction for many ions was recorded at a set point 15 mm outside the front disk electrode, with the temporal length taken as the maximum extent of the times recorded. The temporal bunch length was also observed on release from the ConeTrap in the simulation, taken at a fixed distance from the front electrode. This simulated data shows a slight variation in temporal width due to ion energy changes on extraction, but overall displays that the acceptance of the back cone is an excellent indicator of the ion bunch width. The observed temporal lengths and the simulated both follow the expected behaviour, where the ions spend less time and penetrate less into the back cone as the voltage increases. The front voltage will have minimal effect on the release bunch temporal length. The observed ion rate at +858 V was at background level, with only a few ions per second identifying the edge of the stability region.

4.6.3 Initial optical pumping investigations

The possibility the ConeTrap survival rate is dependent on the stored ions atomic state was explored by optical pumping (section 3.2.1). In an initial experiment potential evidence of an optical pumping effect was observed with ^{138}Ba ions, optically pumped through the transition 6s $^2S_{\frac{1}{2}}(0.000\ \mathrm{cm}^{-1}) \longrightarrow$ 6p $^2P_{\frac{3}{2}}$ $(21952.404\ \mathrm{cm}^{-1})$, while held

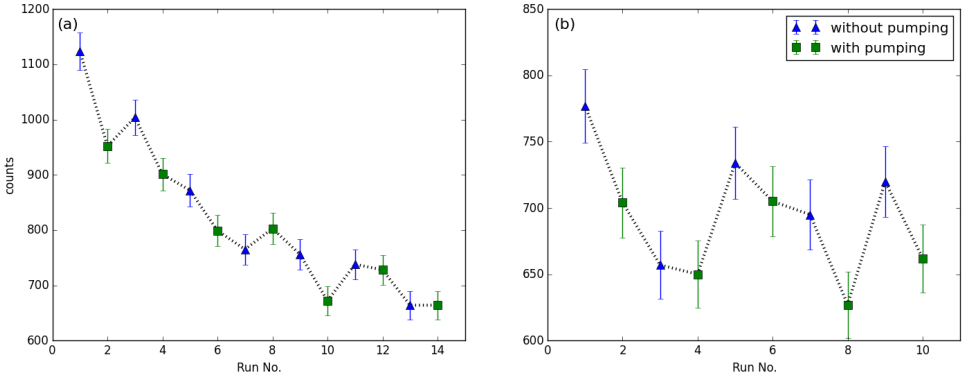

Figure 4.26: Two plots showing the results from the optical pumping of Ba, panel (a) shows the ion counts per 60 seconds for successive iterations with and without the pump laser injected. Panel (b) shows similar measurements following an additional 5 ms storage within the ConeTrap.

in the Cooler–Buncher. The 455.4029 nm light was supplied by a frequency doubled Ti:Sa laser from the FURIOS system. The ion rates were measured over 60 s for 7 successive iterations with and without the pump laser light injected into the Cooler–Buncher. The total ion counts were 13988 ± 118 with the pump laser present and 14878 ± 122 without. The effect of the pump laser was observed to cause a 6.0 ±1.7 % decrease in the total ions detected at the end of the line. In the tests a control experiment was conducted to determine whether the ion survival was changing within the Cooler–Buncher or was due to charge exchange within the ConeTrap. The results are shown in figure 4.26, an overall decrease in the ion rate is shown in panel (a) with the ConeTrap bypassed, with ion totals of 5923 ± 77 without the pump laser and 5519 ± 74 with the ions optically pumped, a decrease of 6.8 ±1.8 %. A definite conclusion could not however be drawn due to instabilities encountered with the discharge source used in the tests. For completeness though panel (b) displays the results (taken in the same test) after containment in the ConeTrap for 5 ms with ion totals of 3583 ± 133 without optical pumping and 3348 ± 129, the difference is within a factor of 2 of the combined error. Tests repeated, under stable on–line conditions are the subject of section 5.3.

Chapter 5

Experimental campaign at IGISOL–4

5.1 Initial experiments at IGISOL–4

The final experimental runs at the IGISOL–3 facility took place in 2010, after which the whole facility was dismantled and relocated to a purpose built laboratory, with a major redesign and replacement of the ion guide and the pre– and post–Cooler–Buncher ion optics. The initial off–line tests for the laser spectroscopy experimental setup took place in early 2013, with successful off–line tests in February 2013 and a later on–line test run in May 2013. Molybdenum was the element chosen for the initial collinear laser spectroscopy investigations due to the large number of stable isotopes for off–line work and the radioactive isotopes are intensely produced in fission. It was one of the last elements studied at IGISOL–3 [44, 47], which enabled a direct comparison of results and performance between IGISOL–3 and 4 to be drawn [9, 48]. The measurements of the ^{101,107}Mo isotopes (previously unobtainable at IGISOL–3) display the improved capabilities of IGISOL–4.

The ground state of the singly charged molybdenum ion possesses a half filled valence shell (d^5) that forms a tightly bound, spherically symmetric $^6S_{5/2}$ state. Excitations from this core produce high–lying excited states, with a high density of metastable levels. Excited metastable states are typically expected to relax within the Cooler–Buncher due to interactions with the buffer gas or impurities, however a naturally enhanced population in the first excited state, $4d^45s\ ^6D_{1/2}$, was observed

at IGISOL–3. This provided access to spectroscopic transitions from this metastable state without the aid of optical pumping.

5.1.1 The first off–line molybdenum tests

The initial off–line tests were performed with ion beams of stable molybdenum. The beams were produced via electrical discharge from a molybdenum cathode within the IGISOL target chamber at a helium buffer gas pressure of a few millibar. The continuous ion beams were extracted and delivered to the collinear laser beam–line at an energy of 30 keV, as detailed in chapter 3. The first collinear laser resonance observed was from the $4d^45s\ ^6D_{1/2}(11783.36\ cm^{-1}) \longrightarrow 4d^45p\ ^6F_{1/2}\ (45853.08\ cm^{-1})$ transition in ^{98}Mo, producing just a single peak (as the nuclear spin, I, is 0). The initial tests confirmed that the new experimental layout was ready for on–line experiments, with no major alterations needed to the laser spectroscopy beam–line. It was however, found that an astigmatism correcting electrode was required (in conjunction with the quadrupole triplet) to optimise the ion–laser beam overlap within the light collection region.

For all stable isotopes of molybdenum the isotope shifts and hyperfine A coefficients were extracted from the recorded resonance spectra, enabling a direct comparison to data from IGISOL–3 [9], as shown in table 5.1. There is discernible shift in the results between IGISOL–3 and IGISOL–4, but at a level well beneath systematic uncertainty. A potential divider stack (10000 to 1) is the main attributed source of systematic error, providing 0.1% error on Cooler–Buncher potential measurement, which is included in the total errors. Any deviation in the dividing fraction of the stack would lead to an apparent shift in the measured voltage, however its unlikely that this is the cause of the observed discrepancy. Alternative causes may include a shift in the potential felt by the ions at the LCR due to a difference in field penetration in the LCR area (between IGISOL–3 and 4) as the charge exchange cell section (before the LCR) has been replaced for IGISOL–4. Potentially the problem could just be with either of the ^{92}Mo measurements, as the relative shifts between the rest of the stable isotopes are much more agreeable between the IGISOL–3 and IGISOL–4 data.

The observed isotope shifts were combined with non–optical, model–independent charge radii data (taken from [30]) to produce a King plot (section 2.3.3) from which

		$\delta\nu^{92,A}$(MHz)	
A	I^{π}	IGISOL–3	IGISOL–4
92	0^+	0	0
94	0^+	-761(1)[9]	-768(1)[8]
95	$\frac{5}{2}^+$	-925(1)[13]	-933(1)[12]
96	0^+	-1390(1)[16]	-1401(1)[17]
97	$\frac{5}{2}^+$	-1391(1)[21]	-1400(1)[21]
98	0^+	-1842(1)[20]	-1847(1)[25]
100	0^+	-2645(1)[33]	-2650(1)[33]

Table 5.1: Comparison of isotope shifts between IGISOL–3 and IGISOL–4 measurements for the $4d^4 5s\ ^6D_{1/2}$(11783.36 cm^{-1}) $\longrightarrow$ $4d^4 5p\ ^6F_{1/2}$ (45853.08 cm^{-1}) transition in the stable molybdenum isotopes. The shifts are given relative to ^{92}Mo, with statistical errors in parentheses and total errors in square brackets [9, 48].

the electronic factor, F, and the mass shift factor were extracted. These were then used to refine the values of $\delta\langle r^2\rangle$ for the stable molybdenum and extract the charge radii from the isotope shifts of the radioactive molybdenum isotopes. The isotope shifts are quoted with respect to ^{96}Mo and both the shifts and the charge–radii are modified by a factor μ, as shown in equation 2.45, where a ^{96,98}Mo reference isotope pair was chosen. From the King plot, shown in 5.1, the atomic field parameter, F, and the nuclear mass shift factor, $\delta\nu_{MS}^{96,98}$, were extracted as $F = -3018(114)$ MHz fm^{-2} and the mass shift factor $\delta\nu_{MS}^{96,98} = 204(32)$ MHz. The fit was obtained by minimizing the ratio of the radial distance between the fit and the data points to the combined errors in the isotope shift and charge radii data. The dominating errors arise from the errors on the charge radii data [30].

In previous work [47] by Charlwood et al. (at IGISOL 3) a calibration of F=–3024(91) MHz fm^{-2} and $\delta\nu_{MS}^{96,98}$=+195(25) MHz were determined for Mo in this reference pair. The assignments, while comfortably consistent, differ in absolute value and on the assigned uncertainties. While it is possible an earlier source of non–optical charge radii data may have been used in the determination of the atomic parameters [49] it is likely that a different approach on the treatment of systematic errors was adopted in the earlier work. The non–optical charge radii data used here and in reference [47], is subject to significant systematic uncertainty from more than one source.

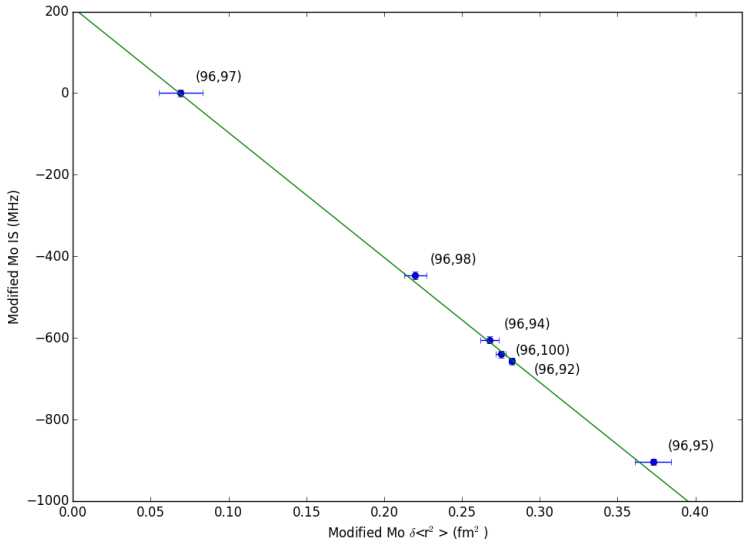

Figure 5.1: A King plot for the stable molybdenum isotopes, with isotopes shifts relative to ^{96}Mo and modified by a reference pair of Mo^{96,98}. The F and M parameters were extracted from the fit as $F = -3018(114)$ MHz fm^{-2} and $\delta\nu_{MS}^{96,98} = 204(32)$ MHz.

Calibration strategies may be adopted in which (initially) only statistical errors are considered and then a final allowance for systematic errors is made or, alternatively, strategies where full errors with appropriate covariances are used. In this work the values and statistical errors (a combination of the nuclear parameter and optical errors) from the combined analysis results of reference [30] were employed, which provided an apparent overestimation of the radial errors and a reduced χ^2 value for the fit of the king plot of 0.049 (as may be expected when large systematic errors are included in statistical fitting). When the errors from the nuclear parameter, λ, alone are used the fit to the data in the King plot is minimised at a reduced χ^2 value of 0.98. For the calibration here, the latter best fit parameters were adopted with the allowance for systematic uncertainties assigned following extraction of $\delta\langle r^2\rangle$.

5.1.2 First on–line molybdenum runs

In mid 2013 the first successful on–line tests of the collinear laser experiment at IGISOL–4 were completed. These tests were undertaken with a natural uranium target mounted in the fission ion guide. A primary beam of 30 MeV protons entered

through a Havar window into the guide and impinged upon the target, inducing fission. The fission fragment recoils were slowed and thermalised in the 250 mbar He buffer gas, and carried to the extraction region by the gas flow. The ions were mass separated and transported to the Cooler–Buncher, where they were held for up to 400 ms before extraction, re–acceleration of the ion ensemble to an energy of 30 keV and final transport to the collinear laser beam–line.

The first on–line resonance observed at IGISOL–4 was for the $4d^45s\ ^6D_{1/2}$(11783.36 cm^{-1}) $\longrightarrow$ $4d^45p\ ^6F_{1/2}$ (45853.08 cm^{-1}) transition in radioactive ^{104}Mo. The resonant photon counting rates for the ^{104}Mo were 2–3 times greater than for the previous run at IGISOL–3 (with a resonant photon counting rate of 2.7 s^{-1} compared to 0.9 s^{-1}), displaying the improvements in yield, beam purity or ion–laser spatial overlap. The ion beam purity has improved, due to the new gas handling system (section 3.1.2). A respectable fraction of the beam consisting of the radioactive isotope desired, as demonstrated by the observation of the decay of ^{98}Zr (half life of 30.7 s) from radioactive build up on the micro–channel plates, with values at IGISOL–4 observed to decay away to half the counts every thirty seconds. One such measurement had an initial ion rate of 6000 s^{-1}, building up to 8500 s^{-1} over a period of 90 s, after which the deflectors we switched off and the decays of ^{98}Zr were observed, with the count rate dropping to background over 150 seconds. This leads to a ^{98}Zr content in the ion beam of $\sim$2500 out of 6000 ions per seconds. A silicon surface barrier detector was recently installed at the end of the laser beam–line for radioactive ion detection, complementing the existing MCPs and germanium detector station.

Measurements for ^{102,104,106}Mo were taken, and the isotope shifts evaluated and compared to IGISOL–3 [9]. The results are summarized in 5.2, where the results for ^{102,104}Mo are consistent within statistical errors however a 30 MHz shift is observed for ^{106}Mo, outside the statistical errors and in the opposite direction compared to the shift observed in the stable Mo isotopes (but again well within systematic error).

5.1.3 Results for ^{101,107}Mo

As described in Section 2, the analysis of optical hyperfine spectra can yield measures of I, μ, Q and isotope shift. New measurements for ^{101}Mo and ^{107}Mo are reported and analysed here. In the former, ^{101}Mo, the ground state nuclear spin has been

A	I^{π}	$\delta\nu^{92,A'}$ (MHz)	
		IGISOL–3	IGISOL–4
102	0^+	−3635(7)[42]	−3640(6)[41]
104	0^+	−4353(6)[46]	−4353(4)[49]
106	0^+	−4836(8)[56]	−4808(8)[56]

Table 5.2: Comparison of the isotope shifts for ^{102,104,106}Mo for the ($4d^4 5s\ ^6D_{1/2}$)⟶($4d^4 5p\ ^6F_{1/2}$) transition as measured at IGISOL–3 and IGISOL–4, the associated statistical errors are given in parentheses and total errors in square brackets.

previously assigned as $\frac{1}{2}^+$ [50]. Great confidence exists in the assignment, which is inferred from the beta decay feeding pattern of the isotope to the near–stability ^{101}Tc system (which consists of a high spin, $\frac{9}{2}^+$, ground state and isomeric, $\frac{1}{2}^-$, first excited state). In ^{107}Mo only a tentative spin assignment, $\frac{5}{2}^+$, has been suggested [51]. The assignment is tentative as different references have suggested differing spin and parity assignments in the system. Assignments were tentatively provided for many ^{107}Mo energy levels in reference [52], with the ground state assigned as $\frac{7}{2}^-$. Independent work [53], that included polarisation–directional correlations and angular correlation, however identified this configuration as an excited state and suggested a $\frac{5}{2}^+$ ground state. In this work, the ground state spin of ^{101}Mo has been confirmed and particular attention has been paid to uniquely determining the ground state spin of ^{107}Mo. No previous magnetic moments or isotope shifts have been reported for either system. The initial data for ^{107}Mo was obtained during the first on–line run [9], however the achieved statistics failed to resolve whether the isotope was spin–$\frac{1}{2}$ or greater (due to a possible weak, fourth resonance peak). The weak nature of the possible fourth peak observed inferred a low spin for the ground state. A further run in January 2014 enabled the collection of more data on ^{107}Mo, to confirm the spin assignment ($\frac{1}{2}$), and provided the first optical measurements of the ^{101}Mo isotope. All measurements were performed using the ^{104}Mo as a frequency reference, where the resonance from the same transition in ^{104}Mo was repeatedly measured in between scans of the odd–N isotopes. This provided a reference to account for any slow drift in the Cooknell or HV platform voltages.

The fitting of the hyperfine structure in the $4d^4 5s\ ^6D_{1/2}(11783.36\ cm^{-1}) \longrightarrow 4d^4 5p$

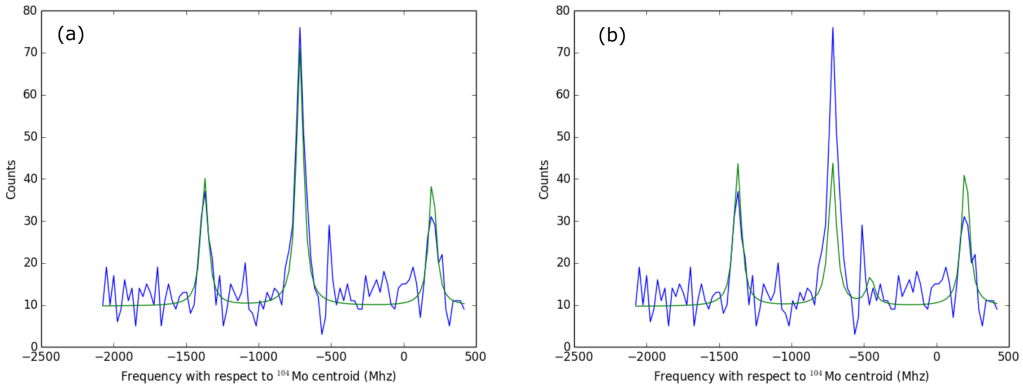

Figure 5.2: Two spectra of the observed $4d^45s\ ^6D_{1/2}(11783.36\ cm^{-1}) \longrightarrow 4d^45p\ ^6F_{1/2}$ $(45853.08\ cm^{-1})$ transition in ^{107}Mo. A least squares minimisation fit to the hyperfine structure for (a) spin–$\frac{1}{2}$ and (b) spin–$\frac{3}{2}$ as shown. The reduced chi–squared values are 1.5 and 2.0, respectively.

$^6F_{1/2}$ $(45853.08\ cm^{-1})$ transition produces two possible solutions for the A_{upper} and A_{lower} (due to the transition being spin $\frac{1}{2}$ to $\frac{1}{2}$). To determine the sign of the A coefficients a second transition, $4d^45s\ ^6D_{1/2} \longrightarrow 4d^45p\ ^6F_{3/2}$ was previously measured in stable ^{95}Mo, with the sign of the A_{lower} determined to be negative [44]. Figure 5.2 displays the obtained ^{107}Mo spectrum with two least squares minimisation fits for nuclear spins of panel (a) $\frac{1}{2}$ and panel (b) $\frac{3}{2}$. The fit minimises the background, full width at half maximum, A_{upper}, A_{lower} and the hyperfine centroid parameters for Lorentzian profiles (suitable due to the heavily reduced Gaussian contributions from Doppler broadening). The uncertainty in the spin assignment came from the observed 'spike' to the right of the central peak, although the reduced χ^2 values of 1.5 and 2.0 respectively strongly infer that the spin–$\frac{1}{2}$ assignment provides a better description of the data than spin–$\frac{3}{2}$. The peak intensities are more representative of a spin–$\frac{1}{2}$ nucleus, however the intensities of the peaks are an unreliable parameter due to potential optical pumping in the light collection region. A unique spin assignment thus required further statistics. If present a fourth peak would have to reside above, below or in–between the three observed peaks, as shown in figure 5.3 for spin–$\frac{5}{2}$. For a fourth peak to be present outside the range covered by the spectrum (shown as regions (a) and (b)) the ratio of the A_{upper}/A_{lower} parameter would diverge significantly from the well established ratio of 0.749(3) (obtained from the A values of previously measured molybdenum isotopes) with the two options shown differing by +360% and -177%.

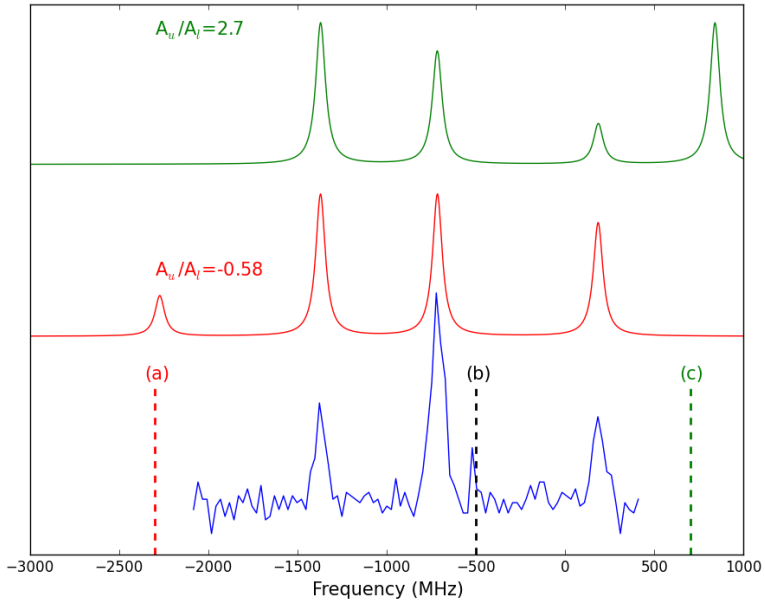

Figure 5.3: A spectrum of ^{107}Mo with the three locations, (a), (b) and (c) indicated where a final hyperfine resonance could be located. The two solid lines display minimised fits to the data for I= $\frac{5}{2}$ subject to the condition that a fourth peak is located at position (c) (top) or (b) (lower) with required A_{upper}/A_{lower} ratios highlighted.

This ratio is expected to hold across the isotope chain, with any variation in the region of 1%. Therefore this restricts a potential fourth resonance peak to a single location, near the –500 MHz mark for any spin greater than $\frac{1}{2}$.

A more detailed scan of the central region for ^{107}Mo (taken in January 2014) shown in figure 5.4 lacks the 'spike' from the previous data set. A χ^2 analysis of the central region was performed, with the centroids, FWHM and, in the case of spins $\frac{3}{2}$ and $\frac{5}{2}$, ratio of peak intensities constrained. A χ^2 value of 31.6 (with 23 degrees of freedom) for spin–$\frac{1}{2}$, a value of 58.3 for the spin–$\frac{3}{2}$ and a value of 125.4 for the spin–$\frac{5}{2}$ fit were measured. Scaling the spin–$\frac{1}{2}$ value to equal the degrees of freedom and scaling the values for the other spin assignments produces a χ^2 value of 42.4 for the spin–$\frac{3}{2}$ assignment, placing a false rejection at outside the 1% level. For the spin assignment $\frac{5}{2}$ the scaled χ^2 value of 91.3, places that assignment at less than the 0.005 % level. The ^{107}Mo nucleus is assigned as spin $\frac{1}{2}$ and the extracted A values for the upper and lower states, along with the isotope shift, $\delta\nu^{104,107}$, are given in table 5.3.

For ^{101}Mo all 3 hyperfine peaks plus the ^{104}Mo reference peak were unobtainable

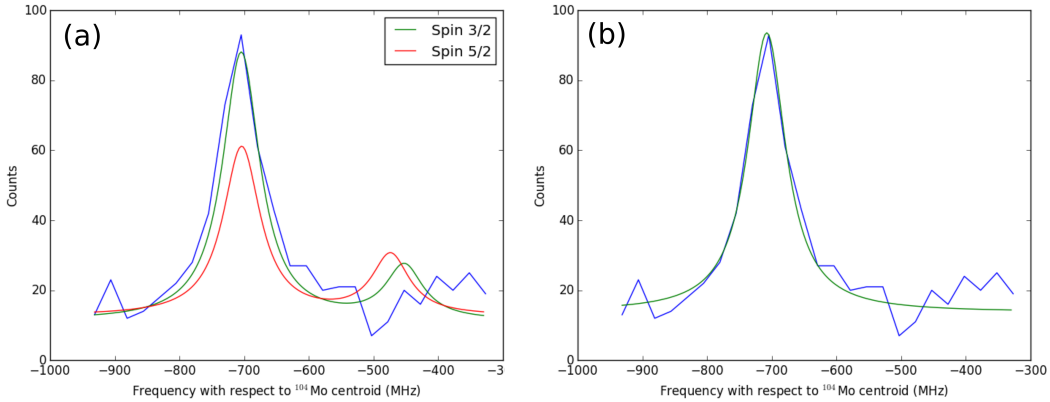

Figure 5.4: Two spectra of the central resonance peak of the ^{107}Mo hyperfine structure given in frequency with respect to the ^{104}Mo centroid, panel (a) shows the peak with spin–$\frac{3}{2}$ and spin–$\frac{5}{2}$ fits and panel (b) shows the spin–$\frac{1}{2}$ fit.

A	Spin	A($^6F_{\frac{1}{2}}$) (MHz)	A($^6D_{\frac{1}{2}}$) (MHz)	$\delta\nu^{104,A'}$ (MHz)	μ (μ_N)
101	$\frac{1}{2}$	−2749(7)	−3695(7)	+1797(4)	−0.732(5)
107	$\frac{1}{2}$	+658(8)	+909(8)	−658(3)	+0.178(2)

Table 5.3: The A coefficients for the upper ($4d^4$ $5p$ $^6F_{1/2}$) and lower ($4d^4$ $5s$ $^6D_{1/2}$) states of the transition as extracted from the data, with the isotope shift given relative to the ^{104}Mo centroid, the associated statistical errors are given in parentheses.

on a single iodine lock. The central and upper peaks were obtained on the initial 17021.2341 cm^{-1} lock along with the ^{104}Mo reference to obtain the isotope shift (the lower peak would have required a positive LCR potential). A second lock at 17020.4333 cm^{-1} was used to obtain the three peaks for 101, allowing for the A values to be extracted, with the reference resonance outside the voltage scan range. The spectrum obtained using the second lock is shown in figure 5.5. The A hyperfine coefficients for the upper ($^6F_{\frac{1}{2}}$) and lower ($^6D_{\frac{1}{2}}$) states were extracted from the data and are displayed in table 5.3 along with the isotope shifts relative to the ^{104}Mo centroid. The magnetic moments were calculated using ^{97}Mo as a reference, with a magnetic moment of $-0.9335(1)\mu_N$ [54].

The mean–square charge radii for ^{101,107}Mo were calculated using the extracted F and $\delta\nu_{MS}^{96,98}$ parameters for the combined analysis of the stable molybdenum and are plotted relative to ^{92}Mo (N=50) in figure 5.6, A 10% systematic uncertainty on the extracted $\delta\langle r^2\rangle$ is not shown. Figure 5.6 displays the change in mean–square charge

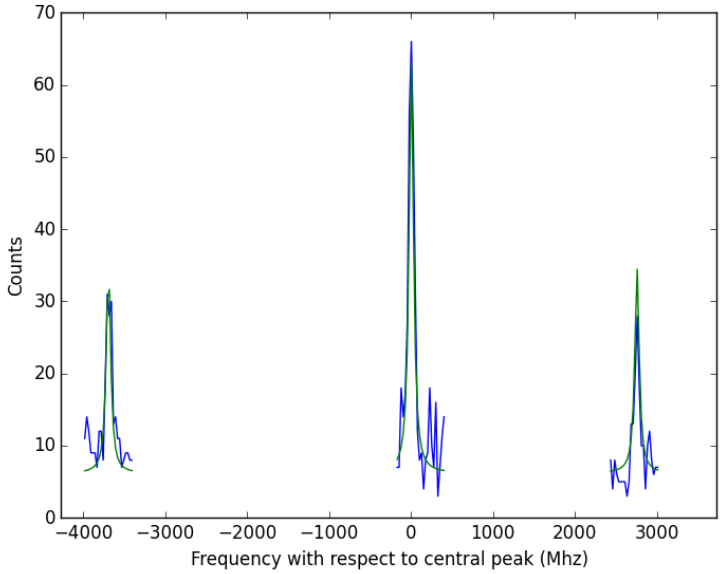

Figure 5.5: A spectrum composed of 3 scan ranges over the 3 hyperfine peaks for the spin $\frac{1}{2}$ ^{101}Mo isotope. A least squares minimisation routine was used to fit the peaks and extract $A_{upper} = -2749(7)$ MHz, and $A_{lower} = -3695(7)$ MHz.

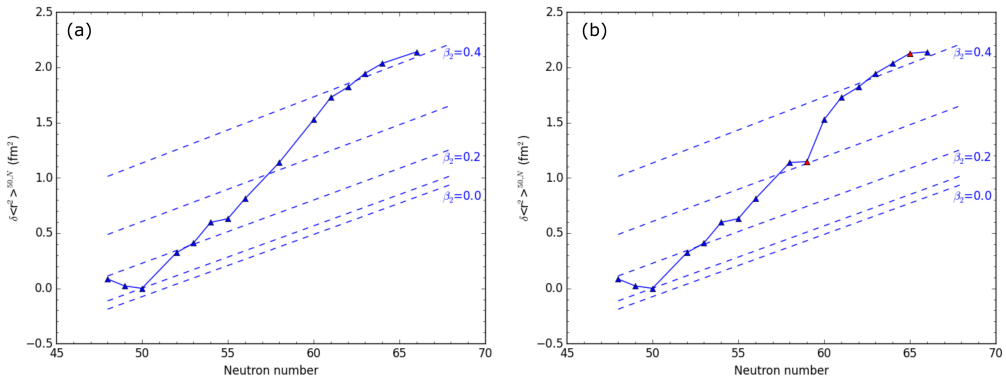

Figure 5.6: The change in the mean–square charge radii of the molybdenum isotopes relative to ^{92}Mo. Panel (a) shows the molybdenum chain without the ^{101,107}Mo mean–square charge radii and panel (b) with the new data showing the development of the charge radius near N=60 is far from the apparently smooth trend of the previous (incomplete) data. The dashed lines are for given ms β_2 deformation values as calculated from the droplet model [55, 19], they are normalised to β_2=0.1 for ^{92}Mo [56].

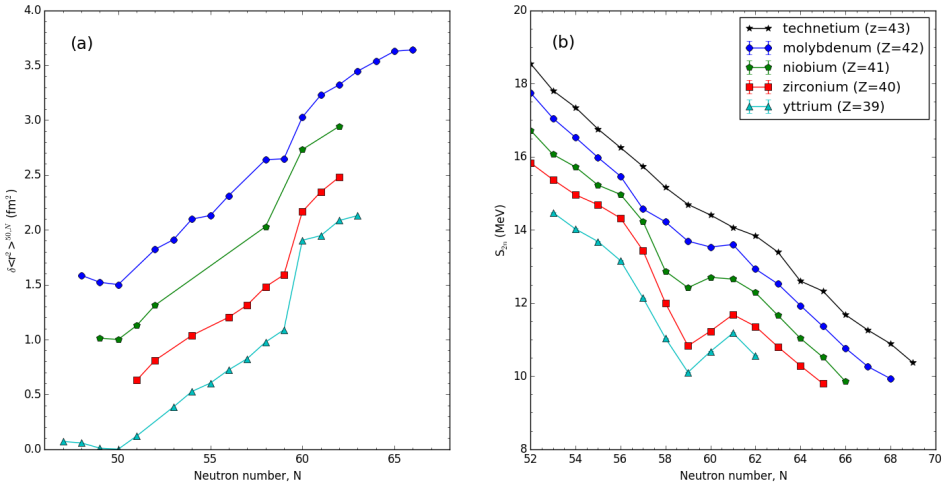

Figure 5.7: Panel (a) displays difference in mean–square charge radii (relative to N=50) across the N=60 region for molybdenum, niobium [41], zirconium [57] and yttrium [58], with a 0.5 fm spacing between the chains for clarity. Panel (b) shows the trend S_{2n} in the N=60 region [59, 60, 61, 62, 63, 64, 65]. A 10% systematic uncertainty on extracted $\delta\langle r^2\rangle$ is not shown, uncertainties in S_{2n} are smaller than the symbol sizes.

radii, with respect to N=50, for molybdenum, panel (a) displays the picture before the inclusion of the ^{101,107}Mo measurements and (b) displays the progression of charge radii with the new measurements, with the development in the mean–square charge radius near N=60 shown to depart from the apparently smooth trend seen with the previous (and incomplete) data.

5.1.4 Discussion of results

Panel (a) of figure 5.7 shows the change in mean–square charge radii near the N=60 region for molybdenum, niobium [41], zirconium [57, 66] and yttrium [58, 67]. The change in mean–square charge radii at N=60 is most prominent in yttrium and becomes smoother with increasing Z (up to technetium) and decreasing Z, through strontium (Z=38) [68, 69] and rubidium (Z=37) [70] to krypton (Z=36) [71] where a smooth transition through deformation is observed in both cases. This behaviour is mirrored in the S_{2n} energies, shown in panel (b) in the figure. A good agreement between the systematics of the mean–square charge radii and two–neutron separation energies is expected due to a $(1 + \frac{5}{4\pi}\delta\langle\beta^2\rangle)$ dependence in the leading terms of the droplet and

Weizsäcker formulas. The two–neutron separation energy is defined as

$$S_{2n} = [-M(A,Z) + M(A-2,Z) + 2n]c^2, \tag{5.1}$$

where $M(A,Z)$ is the nuclear mass. The energies displayed in figure 5.7 are from high precision mass measurements made by the IGISOL Penning trap group [60, 61, 62, 63, 65] with further contributions from references [59] and [64] for technetium. The systematics between the mean–square charge radii and the separation energies are compatible, with yttrium displaying the greatest changes in S_{2n}, decreasing in magnitude towards molybdenum and displaying the smoothest variation in S_{2n} for technetium (Z=43).

The addition of ^{101}Mo data shows a clear odd–even staggering in the mean–square charge radii approaching the N=60 region, which is also seen (to a lesser degree) from N=52–56. A far smoother progression is observed after N=60. Beyond this point almost no odd–even staggering is observed and a clear change in nuclear character is evident. The inclusion of the odd data removes a seemingly featureless development of $\delta\langle r^2\rangle$, that might be erroneously inferred from point to point presentation of even–even only data.

The nuclear magnetic dipole moment of $-0.732(5)$ μ_N for the $\frac{1}{2}^+$ ground state of ^{101}Mo is comparable to the –0.930(4) μ_N value for the $\frac{1}{2}^+$ ground state of ^{99}Zr [72] and the value of –0.498(2) μ_N for ^{97}Sr [68] both of which have an even number of protons and the same number of neutrons as ^{101}Mo. These values are typical of neutron $s_{1/2}$ moments observed in spherical nuclei (i.e. those with less than 60 neutrons) and corresponding to around 50–60% of a Schmidt estimates. The ^{101}Mo ground state is thus attributed to the $\frac{1}{2}^+[420]$ Nilsson orbital.

Nuclei around Z $\sim$40 display near spherical shapes at N=50, becoming more deformed with increasing N, increasing in oblate deformation (both static and dynamic increases) before undergoing sharp changes to (rigid) prolate deformation near N=60. This sharp transition from oblate to prolate is most predominant for yttrium (Z=39), becoming progressively smoother for neighbouring elements with lower and higher Z. For molybdenum this change around N$\simeq$58 is predicted to be gradual, unlike the transitions in the Y, Sr, Zr chains, with a transition from prolate to oblate after the N=60 region (although predictions [73] differ due to the close energy minima of the oblate and prolate deformations, with mean–square charge radii differing due to subtle differences

in calculations of the nuclear ground states). At N=60 ^{102}Mo is expected to be a soft transitional nucleus, with ^{104,106,108}Mo calculated to have triaxial ground state minima and the isotope chain transitioning through these range of shapes [74]. Relativistic mean field calculations [75] predict a gradual rise in mean–square charge radii, with a smooth development, now less comparable to experimental results with the addition of the latest measurements. At N=62 a sharp decrease in $\delta\langle r^2\rangle$ is predicted, with a shift to oblate β_2–deformation, this is not observed in the experimental data. The data instead shows a rising charge radius, peaking at ^{107}Mo (N=65), at a $\delta\langle r^2\rangle^{50,N}$ of 2.14 fm^2, making this system the most deformed molybdenum isotope, in agreement with the predictions of reference [76]. Calculations based on an extended Thomas–Fermi plus Strutinsky integral method underestimate charge radii below N=60, with a large increase at N=60, after which the calculations overestimate $\delta\langle r^2\rangle$ [77]. The new ^{101}Mo measurement makes the change through N=60 less smooth than previously thought, but compatible with the S_{2n} data that shows clear perturbation from a smooth, linear trend (such as that observed at higher Z). The ^{99}Mo isotope will be the subject of future spectroscopy at IGISOL–4 as the additional data from this isotope will provide a clear picture of the shape progression prior to the change now apparent at N=60.

A transition from prolate to (smaller) oblate deformation (which would produce a clear decrease in $\delta\langle r^2\rangle$) is clearly not apparent in the measured molybdenum isotopes and no evidence for such a change is supported here, despite no quadrupole moments being measured. In calculations of reference [76] a maximum in the molybdenum quadrupole deformation is predicted at N=65 and in reference [21] the transition to oblate deformation is predicted around N$\simeq$68. These (in the case of [21], long standing) predictions are supported in this work, and experimentally a further order of magnitude in sensitivity will be required to perform measurements in the region where the transition to oblate shape is expected.

In this work a definitive spin assignment of $\frac{1}{2}$ is made for the ground state of ^{107}Mo. The assignment disagrees with the tentative assignment of $\frac{5}{2}^+$ [53] and an earlier suggestion of $\frac{7}{2}^-$ [52]. The presence of a low–lying spin $\frac{1}{2}^+$ state is however expected theoretically in this isotope [78] and this character has previously been assigned to a 65.4 keV excited state [78] (to explain the observed lifetime and decay multipolarity). An exchange of spin assignments between the ground and excited state is possible,

preserving the existing explanation of the properties of the isomeric state, but impacts significantly on the assignments suggested by [52, 53].

The suggestion of a ground state of $\frac{7}{2}^-$ [52] was based on the assuming that a band built from this state was a $h_{11/2}$ decoupled band (comparable to one observed in ^{103}Mo). The later suggestion of $\frac{5}{2}^+$ arose from assigning the $h_{11/2}$ decoupled band to one arising from an excited state (that decays to the ground state by a strong E1 transition [53]). In both references [52, 53] band structures with the same energies were observed but the interpretation of the low–energy structure (and nature of the bands) differed. The low energy structure of ^{107}Mo is suggested to consist of two, extremely closely spaced, states at 65.4 and 66.0 keV as the first excitation(s). These unfortunately overlap (in energy) with a decay to the ground state in the neighbouring ^{107}Tc nucleus, 65.7 keV, and a variety of pre–1976 measurements of "^{107}Mo" are clearly contaminated by the presence of ^{107}Tc (on inclusion of which an apparent reduction in the lifetime of the 65.4 keV state in ^{107}Mo of a factor of two is observed). Work that would have provided multipolarities and g–factor measures, such as [79], are affected and unfortunately must be revised or rejected. The spin assignment of $\frac{1}{2}$ leaves some existing assignments unaffected (notably decays from bandhead with $\frac{3}{2}^\pm$ to $\frac{5}{2}^+$ are immediately compatible with $\frac{3}{2}^\pm$ to $\frac{1}{2}^+$) but a majority of the high–lying spin assignments must now change. The lowest lying structures, $\frac{1}{2}^+$, $\frac{3}{2}^+$ and $\frac{5}{2}^+$ predicted theoretically [53] are however still compatible with the work here. The spin assignment and magnetic moment reported here are now being investigated theoretically in large scale Monte Carlo shell model calculations. It is hoped that the successful modeling of the surprising result will guide our future investigations in this region.

The quadrupole deformation parameter for ^{107}Mo, suggested from the charge radii is, $\beta_2 \sim 0.4$ and the ground state of the nucleus can be attributed to the $\frac{1}{2}^+[411]$ Nilsson orbital of the $3s_{\frac{1}{2}}$ state. The possible triaxial nature of the molybdenum isotopes around the shape change at N=60 does however make assignment to an axial symmetry configuration problematical (gammas of typically 19–20 degrees are invoked during the modeling of these nuclei [80]).

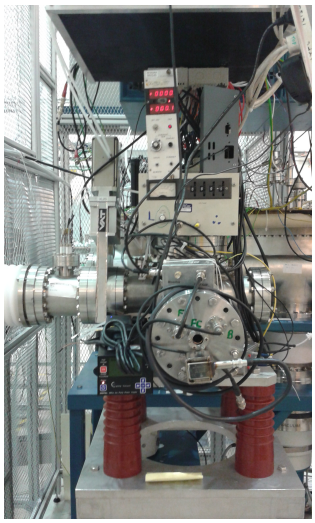

Figure 5.8: Photograph showing the layout of the ConeTrap controls, HV supplies and ion pump control box.

5.2 On–line testing of the ConeTrap

The first on–line tests of the collapsed ConeTrap were successfully completed in October 2014 and are reported in this work. The tests represent a critical development stage for the ConeTrap as absolute efficiency and charge capacity could be accurately determined at full "on–line" conditions (unlike tests with weak current, stable beam). The experiment used a primary beam of 30 MeV protons impinging on a thorium target, producing a range of fission fragments. The ConeTrap was complemented with a 'mesh' Faraday cup attached to the back cone electrode (allowing the HV feed–through to be employed as a Faraday cup readout during initial tuning). An ion pump, section 4.5, was also installed to provide differential pumping near the back cone electrode. It produced only a marginal effect on the ConeTrap performance, but permitted an accurate pressure monitoring at the rear of the trap. The final layout of the ConeTrap and ion pump supplies and controls is shown in the photograph, figure 5.8. During the run the first quantitative results for ion survival following injection and extraction from the ConeTrap were made, along with the observation an optical pumping effect on the survival of singly charged yttrium ions, with the effect enhanced upon further storage in the ConeTrap.

The use of radioactive species enabled ion flux detection and counting without the use of MCPs, which, due to their saturation, limited the total ion flux for injection

into the trap and subsequent observation. Decay detection was achieved through the installation of a germanium detector and a thin Havar foil window, situated at the end of the laser beam–line. The deflector plate potential could be altered to deflect the ion beam onto the Havar window or to the MCPs. During the testing gamma ray lines from the decay of ^{96}Sr (122 keV), ^{97}Y (161 keV) and ^{98}Sr (119 keV) were observed at high efficiency, close to 40%. The increase in detectable ion flux allowed for several performance parameters of the trap to be studied, including ion loading and survival within the ConeTrap. The radioactive decay measurements also provided an accurate determination of the ConeTrap efficiency, by comparing the detected radioactive decay counts with the ConeTrap in operation and with the trap bypassed (and the ions guided straight to the Havar window), as shown by the two spectra in figure 5.9. The measurements were made over a period of 300 seconds at mass A=98, the 4 peaks for ^{98}Sr (119 keV), ^{98}Nb (787 keV), ^{98}Y (1223 keV) and the ^{98m}Y (1591 keV) are labeled, with a comparison of the two yielding a total trapping and transport efficiency of 6.7±0.3 % from the ytrrium lines and the niobium lines (the ratio in strontium was not determined from the 119 keV line due to the presence of a contamination background contribution at this energy). However further investigations displayed problems with the switches and overall extraction from the ConeTrap such that only a fraction of the available ions were be transported down the line.

The spectra (shown in figure 5.9) were taken at yield optimised ConeTrap settings. These were determined following an exploration of the (previously studied) stability regions under on–line conditions. The behaviour of the ConeTrap with respect to the back electrode voltage was investigated, observing the 122 keV gamma ray from the decay of ^{96}Sr isotopes. During the commissioning of the ConeTrap it was apparent that the gamma count rates were more sensitive with respect to the ConeTrap settings than the tests previously performed using the MCPs for ion detection. The observed stability range for a front voltage of +1350 V is shown in figure 5.10, with the back electrode voltage corrected for the power supply off–set. The ConeTrap is observed to begin trapping near +803 V, below the +805/806 V start predicted from simulations and has reached instability by +814 V, giving a narrower stability range than observed with the ion detection off-line, and a lower stability limit than the +819 V from simulation. This shift may be due to a change in the voltage off–set of the Cooknell

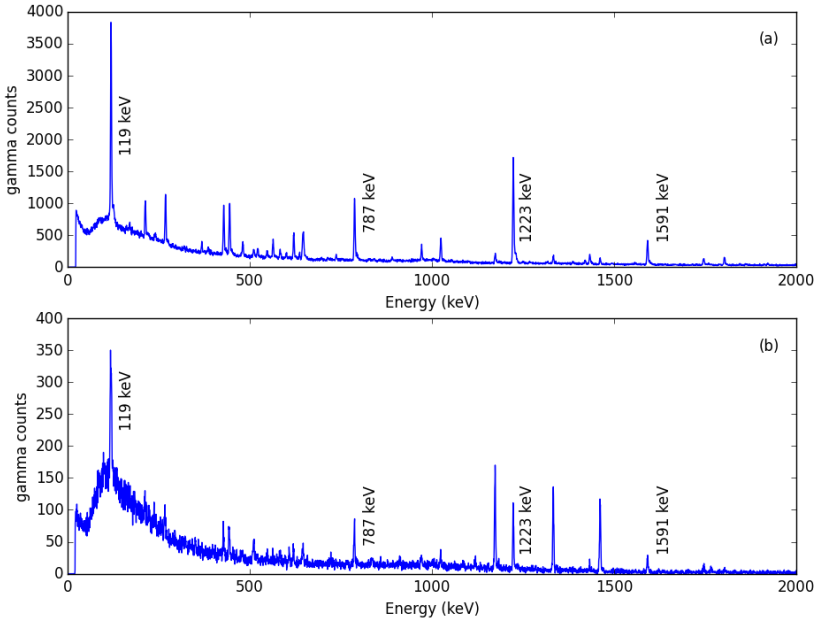

Figure 5.9: Decay gamma spectra at mass A=98, panel (a) is the spectrum with the ConeTrap bypassed and (b) shows the spectrum observed following 5 ms containment in the ConeTrap (both with a 300 s observation period).

power supply output, compared to previous off–line results (section 4.6) which supports the presence of a long term drift in the output voltage.

The ∼7% efficiency was attributed to a combination of losses from ion–gas collisions (section 5.2.1), possible molecular formation, losses during trapping and extraction and poor subsequent transport from the ConeTrap. A large, vertical spatial spread in the ion plume was observed (after storage in the ConeTrap) at the end of the laser beam–line which potentially reduced the observed ion rates. The progression to the collapsed geometry ConeTrap for commissioning increased the distance between the front cone electrode and the einzel plates of the quadrupole deflector, increasing the distance over which the ions need to be focused into the einzel plate. The ion focusing provided by the front cone electrode is inadequate for the full transport of the ejected ions into the quadrupole deflector across this increased distance. Although reasonable transport is obtainable in simulation, in reality it has proven difficult to assess due to a lack of ion beam diagnostics in the beam–line region. Any angular off–set in the cone electrode mounting would also act to steer the ejected ions. This was observed with a full SIMION simulation, which included the ion optic elements of the low energy section

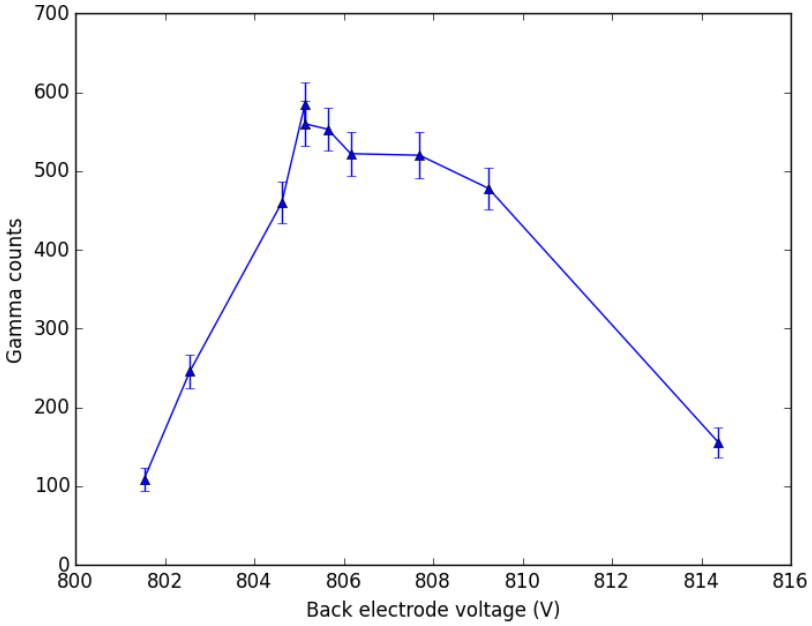

Figure 5.10: A plot of the measured 122 keV gamma ray counts from the decay of ^{96}Sr (observation period of 100 s) after 5 ms storage in the ConeTrap in relation to the back cone voltage (fixed front cone voltage of +1350 V).

and laser beam–line, using electrode potential settings from the optimised beam–line at JYFL. The transport efficiency (with a perfectly trapping ConeTrap) was observed to be as high as 60%, however at the optimised voltage settings from the experimental trap tests large losses were observed with the ions re–entering the quadrupole deflector, with transport efficiencies in the region of 30%. To rectify this transport problem several einzel lens options were explored, based around existing parts and with the aim of providing a solution with minimum changes to the beam–line section required. The addition of an einzel lens, as shown in figure 5.11, will provide control over the ion injection/extraction focusing without affecting the transport settings prior to the trap. Construction and testing of the einzel lens is currently in progress.

5.2.1 Ion survival within the ConeTrap

Initial on–line investigations focused on determining the ion survival with respect to the trapping time, with a minimum containment time of 5 ms. The pressure at the back of the ConeTrap, monitored by the ion pump, was 7.0×10^{-7} mbar, which started at low 10^{-6} before switching on. The storage time was periodically increased and gamma

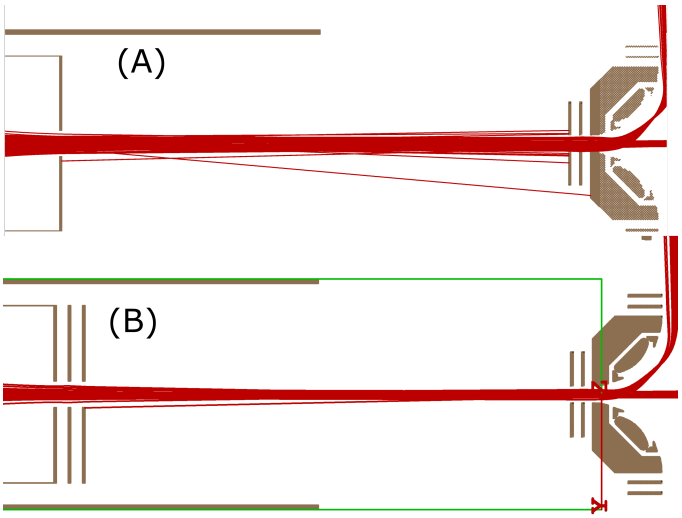

Figure 5.11: A SIMION model of the planned einzel lens plates to improve the ion transport after ConeTrap extraction. Panel (A) displays the simulated ion trajectories without the einzel lens, panel (B) shows the simulated trajectories with the einzel lens plates present (central plate at +300 V).

ray count rates for the decay of ^{96}Sr (122 keV line) were recorded for 300 seconds at each individual storage times. The half–life of 1.07(1) seconds for the decay of ^{96}Sr ensured decay losses were a negligible factor over the 5–10 ms range of storage times. All measurements were made using a constant Cooler–Buncher gas head pressure (3.1 mbar) and a bunching time of 20 ms. The results are shown below in figure 5.12. An expected, decreasing trend was observed with respect to the storage time. The decay was assumed to be exponential in form (due to ion–gas collisions section 4.5) and a mean lifetime of 11.9 $\pm$ 0.9 ms was extracted. This means on average 65.7$\pm$2.0 % of the ions will survive after 5 ms confinement (at a pressure of 7.0×10^{-7} mbar).

During the tests the ConeTrap was loaded with around 30 ions per bunch, to avoid significant contributions from ion–ion collisions. The ion survival probability is inversely proportional to the pressure within the trap, therefore a decrease in the base pressure will increase the ion survival. An order of magnitude improvement in base pressure will be possible in future with the installation of a turbo molecular pump below the quadrupole deflector section, immediately in front of the ConeTrap. The improvement in base pressure will make trapping times in the 100 ms range available without significant ion losses.

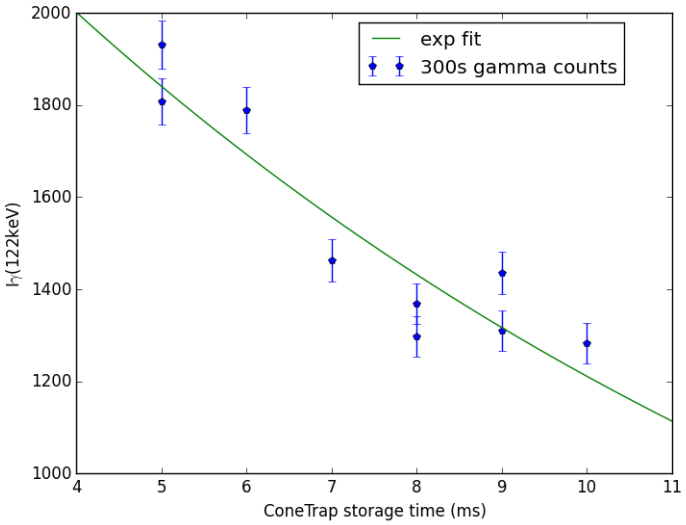

Figure 5.12: A plot of the gamma ray counts observed (over a counting period of 300 s) from the decay of ^{96}Sr (122 keV) as a function of ConeTrap containment time. The green line shows an exponential fit with a mean lifetime determined as 11.9 ± 0.9 ms.

5.2.2 Ion loading within the ConeTrap

A critical operational aspect of the ConeTrap is the maximum ion capacity before ion–ion collisional losses become dominant. This capacity is dependent on the ion density and the overall size and geometry of the trap. The ion survival (for a containment time of 5 ms) with respect to the number of ions injected was studied by observing the 122 keV gamma line from the decay of ^{96}Sr. The number of ions injected was increased by lengthening the bunching time within the Cooler–Buncher, building up ion ensembles prior to injection, with ensembles of 300 to 1500 ions in size. The number of ions per bunch is reduced by the radioactive decay of the ions within the Cooler–Buncher, assuming a constant ion injection rate, F, into the Cooler–Buncher the number of ions per bunch, N, follows the rate equation

$$\frac{dN}{dt} = F - \lambda N. \tag{5.2}$$

The solution for N is given by

$$N = \frac{F}{\lambda}[1 - e^{-\lambda T}], \tag{5.3}$$

where T is the bunching time and λ is the decay constant (determined from the decay halflife of 1.07(1) seconds). The number of ions per bunch in the absence of

radioactive decays is FT, dividing through equation 5.3 by this gives a fractional loss due to radioactive decay in the Cooler–Buncher as

$$\frac{N}{FT} = \frac{1}{\lambda T}[1 - e^{-\lambda T}]. \tag{5.4}$$

As the containment time within the ConeTrap is constant losses due to residual gas collisions will occur at a constant rate for any bunch size, only losses due to the density dependent ion–ion collisions will vary depending on the total ions per bunch (and thus the Cooler–Buncher storage time). The number of ions within the ConeTrap as a function of the containment time is given by equation 4.2, where τ_0 is the mean lifetime due to ion–gas collisions, which was determined as 11.9±0.9 ms for ^{96}Sr ions (section 5.2.1). Using the fact that the quantity $\frac{\Gamma^0_{ii}}{N_0} = \gamma$ is a constant and taking the trapping time as 5 ms equation 4.2 leads to a description of the relative ion survival after trapping as

$$\frac{N(t)}{N_0} = \frac{1}{B + (B-1)\gamma\tau_0 N_0}, \tag{5.5}$$

where $B = e^{5/11.9} = 1.522$. As γ tends towards 0, equation 5.5 just gives the loss fraction due to ion–gas collisions only. The γ constant is dependent on the trap geometry and the ion–ion collisional cross–section and the losses due to ion–ion collisions are comparable to ion–gas collisional losses when $\gamma \sim 1/\tau_0$.

Loading studies were performed at mass A=96, observing an intense 122 keV line from the decay of ^{96}Sr (1.07(1) s half–life). The continuous ion beam rates were measured (using the MCPs) as 1500 ion per second which was used in the analysis to calculate the ions injected into the ConeTrap. It was assumed that all the ions released from the Cooler–Buncher were injected into the ConeTrap and any additional losses occurred during containment or on extraction, the validity of this assumption is returned to at the end of this section. With equations 5.4 and 5.5 giving expressions for the relative losses the intensity of the fit was normalised to two of the data points (50 ms and 800 ms). The first data point at 20 ms was excluded from the analysis, due to it lying far from the expected trend and concerns over the HV switching on the quadrupole bends at 20 ms. All ion optic optimisation (maximising ion flux intensities at the end of the line) was undertaken with a 20 ms bunching time, if this provided insufficient time for the quadrupole deflector potentials to reach ground and stabilise then any optimisation would act to counteract this. Therefore a reduction in ion

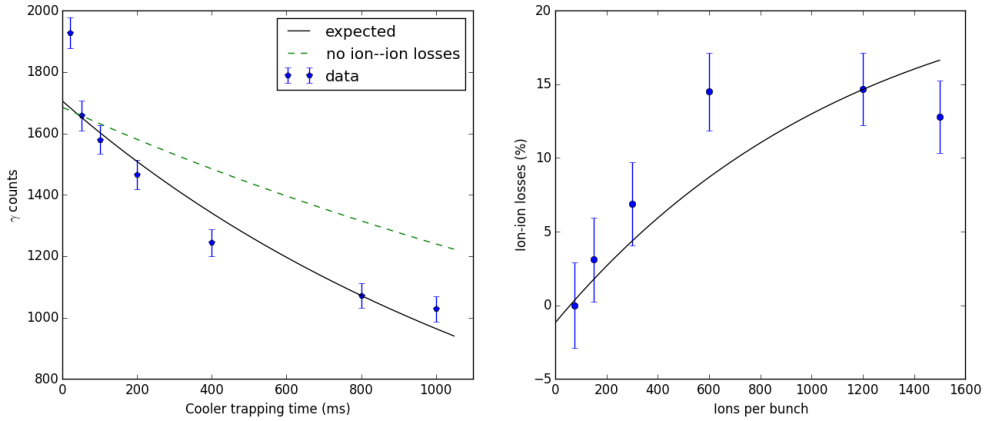

Figure 5.13: A figure showing (a) the gamma ray counts collected over 300 s for the 122 keV gamma line of ^{96}Sr and (b) the calculated ion–ion losses (relative to the 50 ms data point) as a function of ions per bunch. The green dashed line in panel (a) displays the expected losses due to radioactive decay in the Cooler–Buncher.

transport efficiency would be observed when sufficient time for the potentials to lower and stabilise is provided.

The results are shown in figure 5.13, with errors on the peak areas obtained from the automatic region of interest routine in the data acquisition program (GENIE). Panel (a) shows the recorded gamma ray counts as a function of Cooler–Buncher containment time, and panel (b) shows the losses associated to ion–ion collisions (relative to the 50 ms data point). The 50 ms data point was chosen as it represents 75 ions per bunch where any ion–ion collisional losses were minimal. The dashed line in panel (a) shows the expected losses due to the increased storage in the Cooler–Buncher and ion–gas collisions within the ConeTrap, and the solid line shows the fit to the data points using equation 5.4 and 5.5 with γ as a free parameter (the intensity was normalised to the data prior to the fit). The deviation from the dashed line in (a) displays additional losses within the ConeTrap (associated with ion–ion collisions), as displayed in panel (b) where the losses reach 15% for 1500 ions. From the solid line fit the extracted value for γ is 0.033 $\pm$ 0.006, when $\gamma N_0 \simeq \frac{1}{\tau_0}$ the ion–ion losses will be comparable to the ion–gas losses (determined as 34% at 5 ms storage), which occurs around N_0 =2550 ions (at the current ConeTrap pressure), producing a total loss of 68%. The ion–ion collisions initially dominate during containment within the ConeTrap, as shown here with the 5 ms storage time in the ConeTrap.

For the original trap described in [10] the ion–ion collisions were observed to be comparable to the ion–gas collisions at initial bunch sizes of 10,000 ions for 1.5 keV He^+ ions at a trap pressure of 10^{-10} mbar (and at cryogenic temperatures) with an ion–gas collisional mean lifetime of 1.53 s. In comparison we have observed a higher rate of ion–ion loss contributions, with ion–ion loss rates comparable to a mean lifetime 2 orders of magnitude shorter than that at 10^{-10} mbar pressures for ion ensembles one quarter of the size. These rate will be dependent on the ion–ion collisional cross–section and the geometry of the trap. The cones of the original trap are of similar size to the ConeTrap, with the trap operating in a symmetric, low voltage region (electrodes near the 1.5 keV ion energy) creating slow, arcing turning points in the electrodes. In the experiment presented previously the ion mass (A=97) is higher and the injection energies are lower, leading to lower ion velocities within the trap. This apparent onset of (relatively) large ion–ion losses at low ion densities, compared to the original trap may suggest extra loss not due to ion–ion collisions are occurring. Later investigation revealed that a loss contribution was occurring due to molecular formation within the Cooler–Buncher. As such the losses here represent a worst case scenario for the ion–ion losses in the ConeTrap with the true losses potentially an order of magnitude lower.

Under the assumption of the worst case scenario the impact of ion–ion collisional losses can be considered with respect to future use of the ConeTrap. At the typical radioactive ion rates at IGISOL–4 of $\sim$50,000 s^{-1} maintaining a 15% loss would limit bunching times to 30 ms. The present ConeTrap is still readily useable at IGISOL–4. Possible approaches in future experiments to reduce ion–ion collisional losses include a reduction of the high potential applied to the front cone electrode, to reduce the ion density and velocity, as well as increasing the size of the back cone electrode. Increasing the rear cone size would increase the spatial spread of the ions within the trap as well as provide an increased acceptance time (reducing losses during ion injection and extraction) and has been prioritized as a future development.

5.3 Optical pumping of yttrium ions

The possibilities of spectroscopy, based on optical pumping, with the ConeTrap were explored by pre–pumping ionic populations (in the Cooler–Buncher) prior to injection. An optical pumping effect in singly charged (radioactive) yttrium ions, pre–pumped within the Cooler–Buncher and subsequently held for 5 ms in the ConeTrap was successfully observed. The pumping effect was later shown to also occur within the Cooler–Buncher, as the effect was still observed, to a lesser degree, without subsequent containment in the ConeTrap. Bunching times up to 1000 ms were used to maximise the ion–laser interaction times. The laser light from a frequency quadrupled Ti:Sa lasers was tuned to 224.3034 nm for the $5s^2\ S_0$ (0.000 cm^{-1}) $\longrightarrow$ 5s5p P_1 (44568.637 cm^{-1}) state transition in yttrium. To test for a pumping effect the 161 keV gamma ray line from the decay of ^{97}Y isomer was observed (over a counting period of 300 seconds). Subsequent runs with and without the pump laser light injected into the Cooler–Buncher (1000 ms ion storage) were repeated multiple times to observe any changes in the ion survival within the Cooler–Buncher and/or the ConeTrap. The observed gamma ray counts are shown in figure 5.14, the total counts observed with the pump laser light injected equal 4707 $\pm$ 97 and without the laser light the total is 3839 $\pm$ 92. The errors are calculated (in quadrature) from the errors of the 161 keV gamma peak counts for each individual run. The difference is beyond six standard deviations, but fluctuations in the overall count rates perturb the measurement. The data displays higher counts measured with the injected pump laser, than without, apart from the 5th iteration. An overall decrease in the measured count rates is observed over the course of the runs, with and without the presence of the pump laser, associated to a decrease of the ion beam flux. The results however show a clear optical pumping effect on the yttrium ions, with a 22 $\pm$ 3.5 % increase in survival.

To determine if the observed effect was resonant the investigation was repeated at mass A=96, observing the rates of the 122 keV line from the ^{96}Sr decay. The results for the (non–resonant) strontium case are shown in figure 5.15. There was no observed effect for the strontium system, with no discernible effect in ion survival resulting from the presence of the pump laser light. The total observed counts without the pump laser equals 7399 $\pm$ 109, and the total counts with the pump laser present are 7498 $\pm$

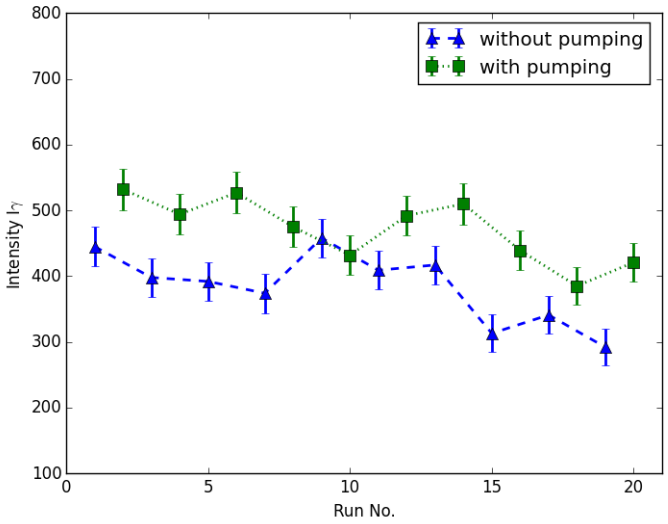

Figure 5.14: This figure shows the 161 keV gamma counts from ^{97}Y decay (counting period of 300 s) for 10 successive cycles with and without the pumping laser injected into the Cooler–Buncher (and subsequent ion storage in the ConeTrap).

109, consistent within one standard deviation.

To resolve if the effect was due to effects (such as charge exchange) within the Cooler–Buncher or due to effects within the 5 ms ConeTrap storage the experiment was repeated without the ConeTrap in operation. The ion bunches were held in the Cooler–Buncher for 1000 ms then transported directly to the end of the laser beam–line and deflected onto the Havar gamma ray window. The results are shown in figure 5.16. Apart from the 5th iteration (run number 9) the count rates are higher with the laser light injected than without. The total counts are 53389 ± 239 with the laser light injected and 52511 ± 235 without, which are consistent within 3 standard deviations. Despite possible consistency the general trend for the counts to be higher with the laser light injected suggests a pumping effect, with a survival increase of 1.7 ± 0.6 %. Again this was repeated with ^{96}Sr, shown in figure and 5.17, with results of 56872 ± 263 without the pump laser, and 56479 ± 261 with the laser light present (the values are within 2 standard deviations). The observed pumping effect is greatly 'enhanced' through the subsequent storage of ions within the ConeTrap (after pumping) although it is unclear if this apparent enhancement is due to further effects (charge exchange) during trapping or is due to a time gating the ConeTrap applies to the ion ensemble.

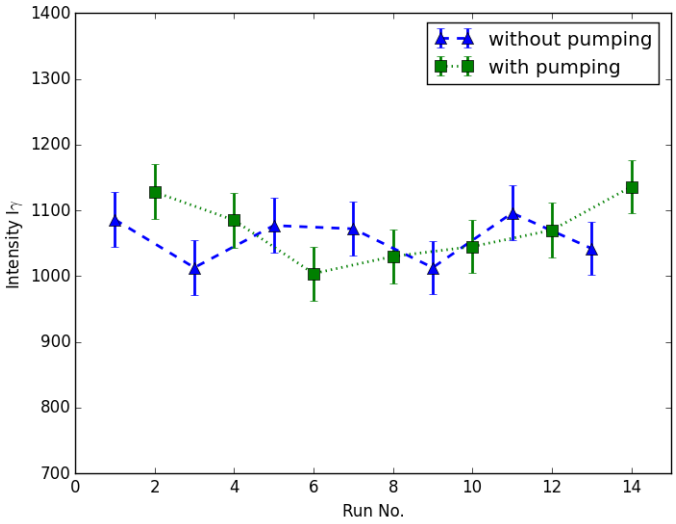

Figure 5.15: This figure shows the gamma ray counts over 300 seconds for the 122 keV line from the decay of ^{96}Sr for 7 iterations with and without the pumping laser light injected. The total counts without the pumping laser are 7399 ±109, and with the laser are 7498±109.

This possible perturbation, a change in the rate of molecular formation in the Cooler–Buncher, was investigated further.

Prior to exploring time related effects, optical pumping effects were explored at mass A=98 using gamma ray lines from Sr (119 keV), Nb (787 keV) and Y (1223 keV) isotopes. The ions were bunched for 200 ms in the Cooler–Buncher, and subsequently transported to the end of the laser beam–line (bypassing the ConeTrap). The same procedure was used, over successive iterations, with and without the pre–pumping in the Cooler–Buncher. The total counts of the successive iterations and errors are given in table 5.4. The total gamma counts display a noticeably larger deviation for yttrium than for either strontium or niobium. Both the Sr and Nb counts (with and without the pump laser light) are within 2 standard deviations respectively, however a larger deviation (within 3 standard deviations) due to the pump laser light is observed for the yttrium ions. This deviation, combined with the measurements on ^{97}Y gives further evidence of a measurable pumping effect.

A final investigation to determine the form of the optical pumping effect was performed, using a time gate on the ion ensemble (through fast switching of the electrostatic deflectors). The ^{88}Y isomer was stored for 20 ms and pre–pumped in the

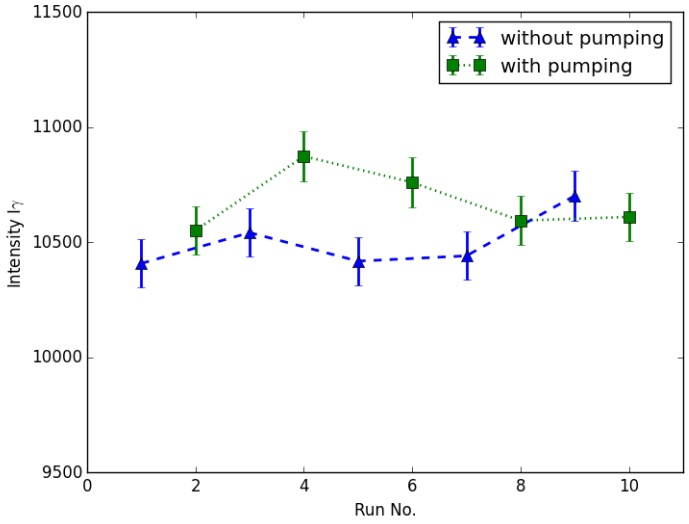

Figure 5.16: A plot showing the 161 keV gamma ray counts (collection period 300 s) for 5 successive iterations with the pumping laser injected (into the Cooler–Buncher) or blocked. The total counts are 52511 ± 235 with the laser blocked and 53389 ± 239 with the laser injected, which are consistent within 3 sigma.

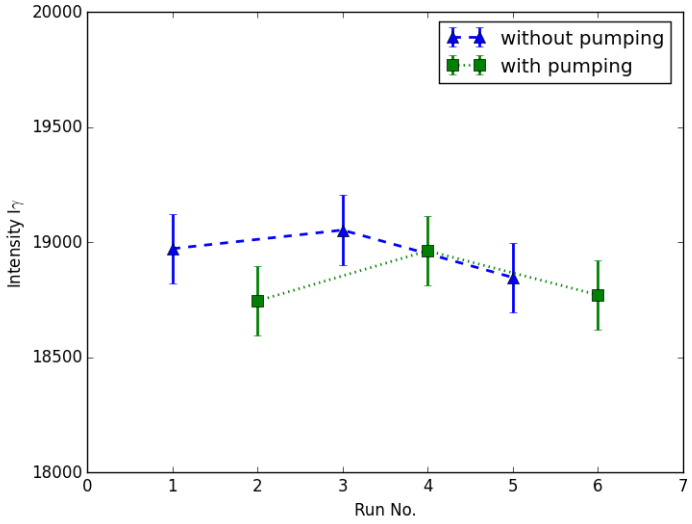

Figure 5.17: A plot showing the gamma ray counts of the 122 keV line from the decay of ^{96}Sr (counting period of 300 s) for successive iterations with and without the pumping laser injected into the Cooler–Buncher.

Laser	Sr (119 keV)	Nb (787keV)	Y (1223 keV)
OFF	46677 ± 282	6804 ± 110	6050 ± 100
ON	46549 ± 286	6988 ± 112	6437 ± 100

Table 5.4: The total counts observed (with statistical errors) over 8 successive iterations injecting and blocking the pumping laser light for the 3 gamma ray lines from the decays of ^{98}Sr (119 keV), ^{98}Nb (787 keV) and ^{98}Y (1223 keV).

Cooler–Buncher at a wavelength of 363.3 nm, exciting the (J=0) ground state to the 27516.691 cm^{-1} (J=1) state transition. The ConeTrap was bypassed for these control studies. A fast HV switch provided a pulsed potential to the deflector plates, switching to half the applied potential for 20 μs, removing 90–92% of the ion plume for this period. The native ion ensemble (those that did not form molecules) were observed to arrive within a 84–97 μs time of flight window at the germanium station. Gamma rays of energy 232 keV and 442.6 keV were observed from the decay of the second isomer, ^{88m2}Y, with a measurement time of 100 seconds. A 20 μs windows were applied to the defector plates, whereby either the ion bunch was excluded ($\sim$84–104 μs). With the 84–104 μs gate a pumping effect was observed, with a measured rate increase of 17.8 ± 1.2% and 14.1 ± 1.3%, counting the 232 keV and 442.6 keV lines respectively. The results for the 232 keV gamma rays are shown in figure 5.18. The total observed gamma counts for the 232 keV line are 19482 ± 140 with optical pumping and 16536 ± 129 without. The recorded counts for the 442.6 keV line are 14601 ± 121 with optical pumping and 12795 ± 113 without. This effect with the time gate is due to radioactive species arriving outside the time gate window, later than 104 μs, with a reduced contribution from the main native ensemble. This implies the ^{88m2}Y are forming molecules within the Cooler–Buncher, hence the increased time of flight to the end of the laser beam–line.

The optical pumping tests were also repeated at mass 87, at the same pump laser frequency, recording the 201 keV gamma ray from the decay of ^{87}Zr. The observed counts without the pump laser were 13056 ± 114 and 13365 ± 116 without the pump laser, which are consistent within 2 sigma, displaying the effect is specific to ^{88m2}Y and resonant.

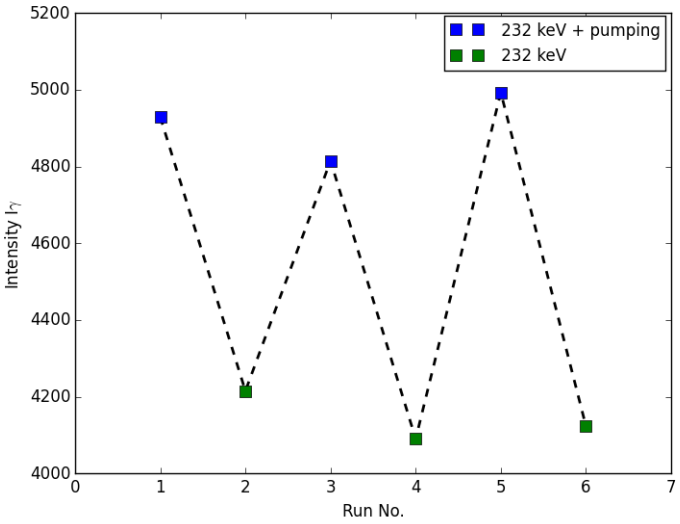

Figure 5.18: The observed 232 keV gamma ray counts from the decay of ^{88m2}Y ion for successive iterations with and without 363.3 nm light injected into the Cooler–Buncher. A 20 μs time gate was applied across the ion ensemble.

5.3.1 Discussion and future work

The occurrence of molecular formation in the Cooler–Buncher is well established [57]. In reference [57] time–of–flight spectra clearly displayed an increase in molecular formation with increasing Cooler–Buncher containment time. The species formed were identified as charged molecular complexes (ligands), where a central metallic ion, Me, bonds with ligand groups, for example MeO^+ and $Me(H_2O)_n^+$. Molecular formation is normally suppressed in the Cooler–Buncher due to the high purity helium gas and low base vacuum pressure (with molecular formation rates under 10% at 100 ms containment).

The observation of an optical pumping effect on the ^{88m2}Y ions using 363.3 nm light, combined with molecular fraction time–of–flight gating, likewise displays an increase in the formation of radioactive, charged molecules in the Cooler–Buncher. A near 20% increase in molecular formation is achieved with storage and pumping times of only 20 ms.

The readily measurable optical pumping effect provides an exciting possibility for future spectroscopy work (exploiting radioactive ion/molecule detection). In the Cooler–Buncher the resonance is broadened (due to ion macro–motion in the Cooler–Buncher) and, previously measured [44], to be of order 10 GHz. As such, only a limited

resolution spectroscopy is attainable using the effect, resonances are however detected at extremely high sensitivities. The total scanning time for the data in figure 5.18 is one (almost two) orders of magnitude less than that used for collinear detection of ^{88m2}Y resonances. As such spectroscopic applications involving weakly produced heavy systems, where large hyperfine structures and uncertainties on isotope shifts exist, match well to the spectroscopic opportunity. Once resonances are coarsely located using (any form of) broadband spectroscopy, higher resolution spectroscopy can be then employed to precisely determine the hyperfine structure and isotope shift. Future work has already been proposed to fully develop and exploit this new technique in locating the hyperfine structure peaks from two isomers of ^{100}Y and ^{102}Y. These isomers were not observed during collinear laser spectroscopy measurements taken on the 363.3 nm line at IGISOL–3 [58], and represent an ideal roof–of–principle application for the spectroscopy.

5.4 Detection of a collinear laser resonance

In December 2014 a further (off–line) run took place at IGISOL–4 aimed at observing a collinear laser resonance from ions extracted from the ConeTrap. This provided a critical measure of any ion energy perturbation, in both shift and spread, due to injection, storage, or extraction from the ConeTrap. Stable hafnium was chosen as the candidate due to a readily accessible transition from the ground state, which was within the Rhodamine 6G dye fluorescence range, and which was known to possess a narrow linewidth. The transition was the 301.29 nm line from the ground state to the 33180.920 cm^{-1} state (J= $\frac{3}{2}$ to J= $\frac{5}{2}$). Hafnium has 5 stable isotopes (mass 176–180), as well as the naturally occurring ^{174}Hf isotope with a lifetime of 2.0×10^{15} years. The most abundant isotope is ^{180}Hf with an abundance of 35.08%, and the ^{174}Hf isotope is the least abundant at 0.16%. Resonantly scattered photons were observed for ^{180,174}Hf with the ConeTrap bypassed, in continuous and bunched ion beam modes. With the ConeTrap in operation the ^{174}Hf isotope was initially chosen, to ensure low ion rates and an unsaturated ConeTrap, however the observed spectrum, shown in figure 5.19 was inconclusive. A possible peak expected near channel 9 cannot be resolved due to the poor signal to background ratio. With the input ion beam switched to ^{180}Hf

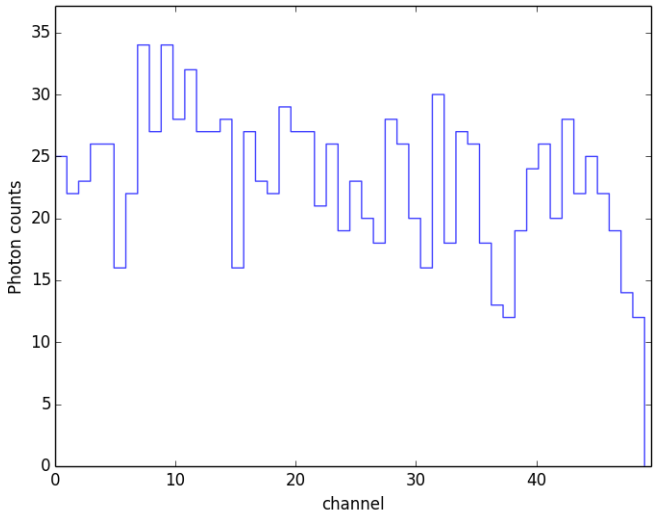

Figure 5.19: An attempted observation of the ground state to 33180.920 cm^{-1} transition in ^{174}Hf with the ion bunches stored within the ConeTrap for 5 ms.

resonantly scattered photons from ConeTrap stored ions were readily observed, and are shown in figure 5.20.

The two spectra shown in figure 5.20 bunched collinear laser spectroscopy of ^{180}Hf, one with the ConeTrap bypassed (top panel) and one with the ions trapped within the ConeTrap for 5 ms (lower panel). The spectra were obtained with a 15 ms bunching time within the Cooler–Buncher over 197 scans (a total of 1.955 seconds per channel) for the first case and 2007 scans for the latter (30.1 seconds per channel). The efficiency with the ConeTrap bypassed was 1 resonant photon per 5000 ions. The spectra show that the total acceleration energy on resonance in both cases are identical, with no observable shift in the resonance position. The ion bunches do not therefore incur an energy perturbation on injection, storage or extraction from the ConeTrap. A marginal difference between the fitted centroids from the two peaks of 5.3 ± 4.1 MHz is observed, with both centroid locations within 2 standard deviations. A marginal narrowing of the full width half maximum of the resonance (as opposed to broadening) may however be observed in the stored ion plume spectrum (lower panel) from 35 ± 3 MHz to 29 ± 6 MHz, which are consistent within one standard deviation. A reduction is compatible with only a temporal subset of ions being interrogated following storage in the ConeTrap as expected from the ion arrival spectra (section 4.6.2).

As discussed earlier in this section it is feasible that only a fraction of extracted

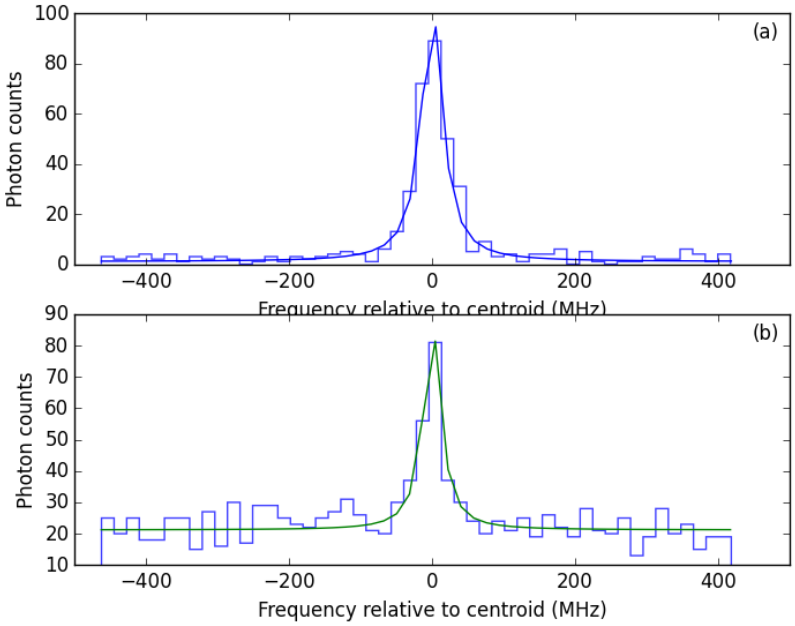

Figure 5.20: A comparison of two laser–ion fluorescence spectra obtained from ^{180}Hf with bunched ion beams (a) bypassing the ConeTrap and (b) stored within the ConeTrap for 5 ms. Both peaks have been fitted with a Lorentzian profile.

ions are transported to the end of the laser beam–line and contribute to the resonance in figure 5.20. Losses due to ion trajectory do not change the conclusions drawn above concerning a shift in energy. Losses due to energy spread, with perturbed ions analysed by the quadrupole bend and ejected from the beam could be reflected in the measurements and contribute to the reduction in the width of the resonance.

Chapter 6

Summary and Outlook

Over the course of this work the IGISOL–4 facility has progressed from the first off–line beams to a fully functioning isotope separator facility. Key milestones for the collinear laser group have been achieved, including the first detected collinear resonance, first collinear measurements of new isotopes and isomers and the first operation of a ConeTrap. The work builds on previous work from IGISOL–3 and displays the improved capabilities of the new facility.

In this thesis the IGISOL–4 facility has been outlined and the key improvements from IGISOL–3 described. An overview of a new microcontroller based data acquisition system has been presented. The system will replace all of the hardware based time gating units (with pure software controls), a bulky VME crate and SUN microsystems computer. Instead a small, compact unit connected via USB to a computer or suitable portable device will provide greatly upgraded acquisition capabilities. The main features include photon time stamping (for the first time) enabling corrections of an 'artificial' energy broadening. A new data collection method applicable for the detection of weak hyperfine peaks, has further been implemented.

The principles and development of the electrostatic ConeTrap have been presented, along with possible designs for a future central laser interaction region within the trap. The interaction region will provide a suitable location for in–trap optical manipulation and spectroscopy. Comparisons of the stability regions for the respective designs along with central field structure are given. The device will, in future, provide "resolution adjustable" spectroscopy at JYFL and make possible a range of studies of the heavy elements. The commissioning of the (collapsed geometry) trap was successful, with

the first ions injected, stored and extracted during an off–line run at an estimated efficiency of 1 in 200. This rose to an actual performance efficiency of 1 in 10 ions with full optimisation using radioactive ion detection. The behaviour of the trap on–line was compared to a full SIMION simulation of the apparatus with excellent reproduction of experimental results. The combined experimental and theoretical effort show the trap is performing as intended and ready for exploitation.

Spectroscopy using the ConeTrap has also been possible, the first off–line and on–line tests have taken place, and the first collinear laser resonance detected from ions ejected out of the device. The application of the optical pumping technique within the Cooler–Buncher (which began at IGISOL–3) has been re–established for IGISOL–4, along with a first, exciting, observation of pumping effects on ion survival within the Cooler–Buncher and ConeTrap producing a spectroscopically usable effect.

The first, entirely new measurements with IGISOL–4 are presented here for two critical odd isotopes, ^{101,107}Mo. The two isotopes are at the lower limit of fission production, too weakly produced for study at IGISOL–3, and thus displaying the improved capabilities of IGISOL–4. The obtained results provide a valuable insight into changes of the nuclear deformation, as displayed by the changes imposed by the new results on the $\delta\langle r^2\rangle$ trend across the isotope chain.

In the near future construction (completed as of writing) and testing of suitable laser interaction regions for the ConeTrap will take place. The interaction regions will take advantage of the long interaction times available during storage, for optical pumping studies within the low vacuum conditions and future in–trap spectroscopy. The installation and testing of an einzel lens, immediately before the ConeTrap, will commence, with the aim of improving overall transport and ion extraction. Optical pumping within the Cooler–Buncher will be immediately exploited for future high sensitivity, medium resolution studies, with a proposal for exploiting the technique for studies of yttrium isomers already submitted.

Appendix A

High voltage switching

Several bespoke switches, manufactured in this work, are employed for switching the high voltages (HV) applied to the quadrupole bend shim and rod electrodes and the front electrode of the ConeTrap. The switches on the rod and shim electrodes are required to switch from ground to around +1600 V and –1600 V respectively. The switches are composed from a chain of 5 opto–couplers in series, with a 22 MΩ pull–down resistor, and they switch on within a couple of milliseconds. This imposes a lower limit on the trapping time of the ConeTrap (>5 ms) to allow sufficient delay for the potentials to fall to ground before the next bunch release from the Cooler–Buncher. Due to the speed the bunching time needs to be equal to or greater than 15 ms otherwise ions still experience the fields from the electrodes while the voltages are changing (as noted by the fluctuating ion current below 20 ms when testing the ConeTrap).

The front ConeTrap electrode is switched between +1100–1400 V and +600–700 V, with the voltage lowered for 20 μs for ion bunch injection and extraction. The rise/fall times need to be sub–microsecond to ensure the ions do not experience a gradually changing field within the cone electrode. The recovery to baseline must likewise be flat to ensure no drift tube like effects alter the ion energy on transit. The details of the initially used front electrode switch can be found in [9], a new design has been constructed in this work employing two power MOSFETS in a push–pull orientation. The purpose is to improve the switching times and remove a gradual slope on the low voltage baseline. The circuit layout is shown below in figure A.1. Capacitor banks on the high and low side are necessary to provide the instantaneous current required

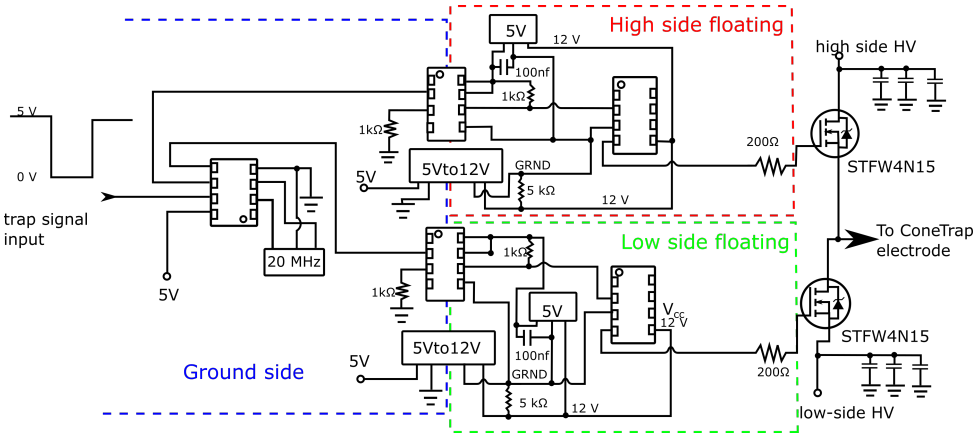

Figure A.1: Circuit diagram of the push–pull HV switch design, with two electrically isolated floating sections for the high–side switch and low–side switch.

during switching, removing a "shoulder" on the switch rise waveform and reducing the rise and fall times. The timing between the two gate driver signals was found to be critical, and a programmable microcontroller (ATtiny85) was used to tune the switching time to reduce the "shoulder" on the rise time to less than 1 V in 350 V. The timing must ensure that the threshold voltage is crossed on the first MOSFET before the second MOSFET threshold voltage is crossed ('break' before 'make'). The 200Ω resistors on the gate driver outputs are to protect the MOSFETS when they are switched on. The low side voltage is provided though a potential divider from the high side voltage power supply, with a potentiometer to allow for tuning of the injection and extraction electrode.

A.1 Bunching switch

A new HV switch for the +50 V trapping potential of the Cooler–Buncher was also built, following a similar push–pull MOSFET design. The circuit layout is shown in figure A.2, with the input signal routed into the ATtiny85 and to a +5 V TTL output to fire the ConeTrap control box. This circuit relies on 2 MOSFETS (STFW4N150) driven by a single gate driver. The low (ground) side of the switch is connected to the low side of the gate driver, the high side (+50 V) floats at +50 V or 0 V, with a second +5 V to +12 V isolated DC to DC converter supplying the +12 V bootstrap supply on top of the bridge. Both switches are now in use at the IGISOL–4 facility.

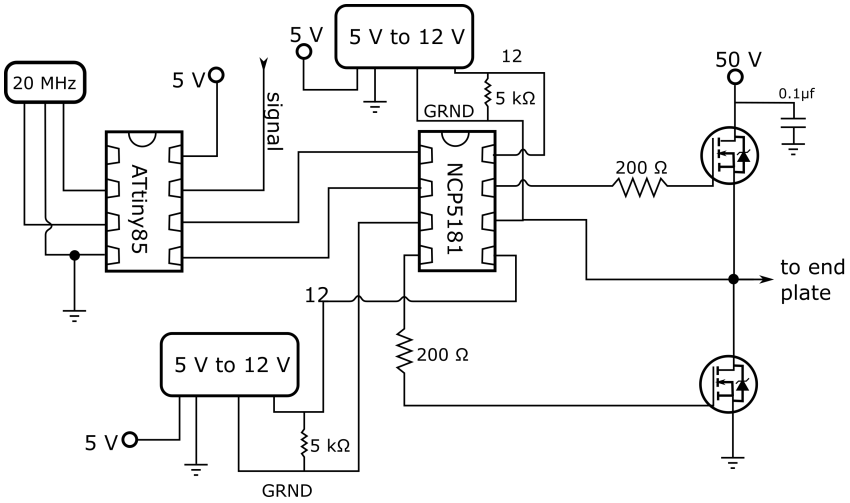

Figure A.2: Circuit diagram for the +50 V HV switch for the Cooler–Buncher end–plate potential. The voltage is switched down to ground for 100 μs to allow the ions to exit the Cooler–Buncher.

Bibliography

[1] E. Rutherford. "The scattering of alpha and beta particles by matter and the structure of the atom". *Philosophical Magazine*, 21:669–688, (1911).

[2] K. Bleuler. Wolfgang pauli: His scientific work and his ideas on the foundations of physics. In *Geometry and Theoretical Physics*, pages 304–310. Springer Berlin Heidelberg, (1991).

[3] E. Back and S. Goudsmit. "Kernmoment und Zeemaneffekt von Wismut". *Z. Phys.*, 47:174–183, (1928).

[4] H. C. Urey et al. "A hydrogen isotope of mass 2". *Physical Review*, 39:164–165, (1932).

[5] J. Chadwick. "Possible existence of a neutron". *Nature*, 129:312, (1932).

[6] T. Schmidt and H. Schüler. *Z. Phys.*, 94:457–468, (1935).

[7] J. Äystö et al. *Three decades of research using IGISOL technique at the University of Jyväskylä*. Springer Netherlands, (2014).

[8] J. Billowes et al. "First collinear laser spectroscopy measurements of radioisotopes from an IGISOL ion source". *Nuclear Instruments and Methods in Physics Research Section B: Beam Interactions with Materials and Atoms*, 126:416–418, (1997). International Conference on Electromagnetic Isotope Separators and Techniques Related to Their Applications.

[9] D. J. S. Johnson. *An electrostatic ion trap for laser and nuclear spectroscopy at the IGISOL*. PhD thesis, University of Manchester, (2013). (Unpublished).

[10] H. T. Schmidt et al. "Conetrap: A compact electrostatic ion trap". *Nuclear Instruments and Methods in Physics Research Section B: Beam Interactions with Materials and Atoms*, 173:523–527, (2001).

[11] A. Fardi. *"ConeTrap: An electrostatic ion trap for atomic and molecular physics"*. PhD thesis, Stockholm University, (2001). (Unpublished).

[12] N. A. Jelley. *Fundamentals of nuclear physics*. Cambridge university press, (1990).

[13] Kenneth S. Krane. *Introductory nuclear physics*. John Wiley & Sons, (1988).

[14] R. C. Barrett. "Model–independent parameters of the nuclear charge distribution from muonic X–rays". *Physics Letters B*, 33:388–390, (1970).

[15] T. Seo. "Nillson potential parameters for all mass regions". *Z. Phys. A - Atomic Nuclei*, 324:34–52, (1986).

[16] W. D. Myers and W. J. Swiatecki. "Average nuclear properties". *Annals of Physics*, 55:395–505, (1969).

[17] W. D. Myers and W. J. Swiatecki. "The nuclear droplet model for arbitrary shapes". *Annals of Physics*, 84:186–210, (1974).

[18] P. Möller and J. R. Nix. "Nuclear mass formula with a Yukawa–plus–exponential macroscopic model and a folded–Yukawa single–particle potential". *Nuclear Physics A*, 361:117–146, (1981).

[19] W. D. Myers and K. Schmidt. "An update on droplet–model charge distributions". *Nuclear Physics A*, 410:61–73, (1983).

[20] P. Möller et al. "Nuclear mass formula with a finite–range droplet model and a folded–Yukawa single particle potential". *Atomic Data and Nuclear Data Tables*, 39:225–233, (1988).

[21] J. Skalski et al. "Equilibrium shapes and high–spin properties of the neutron–rich A$\simeq$ 100 nuclei". *Nuclear Physics A*, 617:282–385, (1997).

[22] M. Bender et al. "Collectivity–induced quenching of signatures for shell closures". *Physical Review C*, 78:054312, (2008).

[23] J. P. Delaroche et al. "Structure of even–even nuclei using a mapped collective Hamiltonian and the D1S Gogny interaction". *Physical Review C*, 81:014303, (2010).

[24] A. Corney. *Atomic and Laser Spectroscopy*. Oxford Classic texts, (2006).

[25] J. R. Persson. "Table of hyperfine anomaly in atomic systems". *Atomic Data and Nuclear Data Tables*, 99:62–68, (2013).

[26] W. H. King. *Isotope shifts in atomic spectra*. Physics of atoms and molecules. Springer, (1984).

[27] A. R. Bodmer. "Isotope shift and changes of nuclear radius". *Nuclear Physics*, 9:371–290, (1958).

[28] S. A. Blundell. "A re–evaluation of isotope shift constants". *Z. Phys. A - Atoms and Nuclei*, 321:31–33, (1985).

[29] S. A. Blundell. "A reformulation of the theory of field isotope shift in atoms". *Journal of Physics B: Atomic and Molecular Physics*, 20:3663, (1987).

[30] G. Fricke and K. Heilig. *Nuclear charge radii*, volume 20. Landolt-Brnstein - Group I, Elementary Particles, Nuclei and Atoms, Springer Berlin Heidelberg, (2004).

[31] E. Liukkonen. "New K130 cyclotron at Jyväskylä". *Proceedings of the 13th International Conference on Cyclotrons and their Applications, Vancouver, BC, Canada*, (1993).

[32] J. Huikari et al. "Production of neutron deficient rare isotope beams at IGISOL; on–line and off–line studies". *Nuclear Instruments and Methods in Physics Research B*, 222:632–652, (2004).

[33] P. Karvonen et al. "A sextupole ion beam guide to improve the efficiency and beam quality at IGISOL". *Nuclear Instruments and Methods in Physics Research B*, 226:4794–4807, (2008).

[34] P. Karvonen. *"Fission yield studies with SPIG–equipped IGISOL: A novel method for nuclear data measurements"*. PhD thesis, University of Jyväskylä, (2010). (Unpublished).

[35] B. Cheal and D. H. Forest. "Collinear laser spectroscopy techniques at JYFL". *Hyperfine Interactions*, 223:63–71, (2014).

[36] A. Nieminen et al. "Beam cooler for low–energy radioactive ions". *Nuclear Instruments and Methods in Physics Research Section A: Accelerators, Spectrometers, Detectors and Associated Equipment*, 469:244–253, (2001).

[37] M. Reponen et al. "Laser developments and resonance ionization spectroscopy at IGISOL". *European Physical Journal A*, 48, (2012).

[38] T. Kessler et al. "An injection–seeded high–repetition rate Ti:Sapphire laser for high–resolution spectroscopy and trace analysis of rare isotopes". *Laser Physics*, 18:842–849, (2008).

[39] V. Sonnenschein et al. "Determination of the ground–state hyperfine structure in neutral ^{229}Th". *Journal of Physics B: Atomic, Molecular and Optical Physics*, 45:165005, (2012).

[40] J. Brossel and F. Bitter. "A new "double resonance" method for investigating atomic energy levels". *Physical Review*, 86:308–316, (1952).

[41] B. Cheal et. al. "Laser spectroscopy of niobium fission fragments: first use of optical pumping in an ion beam cooler buncher". *Physical Review Letters*, 102:222501, (2009).

[42] B. Cheal and K. T. Flanagan. "Progress in laser spectroscopy at radioactive ion beam facilities". *Journal of Physics G: Nuclear and Particle Physics*, 37:113101, (2010).

[43] S. L. Kaufman. "High–resolution laser spectroscopy in fast beams". *Optics Communications*, 17(3):309–312, (1976).

[44] F. C. Charlwood. *Ground state properties of Mn and Mo using laser spectroscopic methods*. PhD thesis, University of Manchester, 2010. (unpublished).

[45] P. Reinhed et al. "Cryogenic keV ion–beam storage in ConeTrap – A tool for ion–temperature control". *Nuclear Instruments and Methods in Physics Research A*, 621:83–90, (2010).

[46] Charged particle optics simulation software, SIMION. http://simion.com.

[47] F. C. Charlwood et al. "Nuclear charge radii of molybdenum fission fragments". *Physics Letters B*, 674:23–27, (2009).

[48] A. R. Dicker et al. "Laser spectroscopy at IGISOL IV". *Hyperfine Interactions*, 277:139–145, (2014).

[49] G. Fricke and C. Bernhardt. "Nuclear ground state charge radii from electromagnetic interactions". *Atomic data and nuclear data tables*, 60:177–285, (1995).

[50] Jean Blachot. "Nuclear data sheets for A=101.". *Nuclear data sheets*, 83, (1998).

[51] Jean Blachot. "Nuclear data sheets for A=107". *Nuclear data sheets*, 109:1383–1526, (2008).

[52] J. K. Hwang et al. "Identification of ^{109}Mo and possible octupole correlations in ^{107,109}Mo". *Physical Review C*, 56, (1997).

[53] W. Urban et al. "Near–yrast, medium–spin structure of the ^{107}Mo nucleus". *Physical Review C*, 72, (2005).

[54] I. Mills et al. *Quantities, Units and Symbols in Physical Chemistry.* Blackwell Scientific Publications, (1988).

[55] D. Berdichevsky and F. Tondeur. "Nuclear core densities, isotope shifts, and the parametrization of the droplet model". *Zeitschrift fr Physik A Atoms and Nuclei*, 322(1):141–147, 1985.

[56] S. Raman et al. "Transition probability, B(E2), from the ground state to the first–excited 2^+ state of even–even nuclides". *Atomic Data and Nuclear Data Tables*, 36:1–96, (1987).

[57] P. Campbell et. al. "Laser spectroscopy of cooled zirconium fission fragments". *Physical Review Letters*, 89:082501, (2002).

[58] B. Cheal et. al. "The shape transition in the neutron–rich yttrium isotopes and isomers". *Physics Letters B*, 645:133–137, (2006).

[59] G. Audi et al. "The AME2003 atomic mass evaluation". *Nuclear Physics A*, 729:337–676, (2003).

[60] U. Hager et al. "First precision mass measurements of refractory fission fragments". *Physical Review Letters*, 96:042504, (2006).

[61] U. Hager et al. "Precision mass measurements of neutron–rich yttrium and niobium isotopes". *Nuclear Physics A*, 793:20–39, (2007).

[62] A. Kankainen et al. "Mass measurements of neutron–deficient nuclides close to A=80 with a Penning trap". *The European Physical Journal A*, 29:271–280, (2006).

[63] S. Rinta-Antila et al. "Decay study of neutron–rich zirconium isotopes employing a Penning trap as a spectroscopy tool". *European Physical Journal A*, 31:1–7, (2007).

[64] J. Fallis et al. "Mass measurements of isotopes of Nb, Mo, Tc, Ru and Rh along the $\nu p-$ and $rp-$process paths using the Canadian Penning trap mass spectrometer". *Phsical Review C*, 84:045807, (2011).

[65] U. Hager et al. "Precision mass measurements of neutron–rich Tc, Ru, Rh and Pd isotopes". *Physical Review C*, 75:064302, (2007).

[66] P. Campbell et al. "Laser spectroscopy of radioactive Ti, Zr and Hf isotopes and isomers at the JYFL laser–IGISOL facility". *Spectrochimica Acta part B*, 58:1069–1076, (2003).

[67] K. Baczynska et al. "Nuclear spin determination of ^{100m}Y by collinear laser spectroscopy of optically pumped ions". *Journal of phyiscs G: Nuclear and Particle Physics*, 37:105103, (2010).

[68] F. Buchinger et al. "Systematics of nuclear ground state properties in $^{78-100}$Sr by laser spectroscopy". *Physical Review C*, 41:2883–2897, (1990).

[69] P. Lievens. "Nuclear ground state properties of ^{99}Sr by collinear laser spectroscopy with non–optical detection". *Physics Letters B*, 256:141–145, (1991).

[70] C. Thibault. "Hyperfine structure and isotope shift of the D_2 line of $^{76-98}$Rb and some of their isomers". *Physical Review C*, 23:2720–2729, (1981).

[71] M. Keim. "Laser–spectroscopy measurements of $^{72-96}$Kr spins, moments and charge radii". *Nuclear Physics A*, 586:219–239, (1995).

[72] H. L. Thayer et al. "Collinear laser spectroscopy of radioisotopes of Zirconium". *Journal of Physics G: Nuclear and Particle Physics*, 29, (2003).

[73] P. Möller et al. "Nuclear ground–state masses and deformations". *Atomic Data and Nuclear Data Tables*, 59:185–381, (1995).

[74] R. Rodríguez-Guzmán et al. "Charge radii and structural evolution in Sr, Zr and Mo isotopes". *Physics Letters B*, 691:202–207, (2010).

[75] G. A. Lalazissis and S. Raman. "Ground–state properties of even–even nuclei in the relativistic mean–field theory". *Atomic Data and Nuclear Data Tables*, 71:1–40, (1999).

[76] P. Möller. "Axial and reflection asymmetry of the nuclear ground state". *Atomic Data and Nuclear Data Tables*, 94:758–780, (2008).

[77] Y. Aboussir and J. M. Pearson. "Nuclear mass formula via an approximation to the Hartree–Fock method". *Atomic Data and Nuclear Data Tables*, 61:127–176, (1995).

[78] J. A. Pinston et al. "Triaxiality in ^{105}Mo and ^{107}Mo from the low to intermediate spin region". *Physical Review C*, 74, (2006).

[79] E. Cheifetz and A. Wolf. "Measurements of g–factors of isomeric states in fission fragments". *3^{rd} international conference on nuclei far from stability*, (1976). (proceedings).

[80] H. Hua et al. "Triaxiality and the aligned $h_{11/2}$ neutron orbitals in neutron–rich Zr and Mo isotopes". *Physical Review C*, 69, (2004).